AN ABSTRACT OF THE DISSERTATION OF

Sukosin Thongrattanasiri for the degree of Doctor of Philosophy in Physics presented on July 22, 2010.

Title: Computational Nanooptics in Hyperbolic Metamaterials and Plasmonic Structures

Abstract approved: _____

Viktor A. Podolskiy

This dissertation concerns several problems in the fields of light interaction with nanostructured media, metamaterials, and plasmonics. We present a technique capable of extending operational bandwidth of hyperbolic metamaterials based on interleaved highly-doped InGaAs and undoped AlInAs multilayer stacks. The experimental results confirm theoretical predictions, exhibiting broadband negative refraction response in mid-infrared frequency.

We propose a new class of nanofocusing structures, named hypergrating, combining hyperbolic metamaterials with Fresnel optics, able to achieve extremely subwavelength focal spots (up to 50 times smaller than free-space wavelength) in the far field of the input interface. Several experimental realizations of hypergratings for visible and infrared frequencies are presented.

We further develop a new technique capable of imaging subwavelength objects with far-field measurements. The approach utilizes a diffraction grating, placed at the object plane, to convert subwavelength information of objects into propagating waves and project this information into far-field. The set of far-field measurements is used to deconvolute the images. The resolution of the proposed method can surpass 1/20-th of the free-space limit, strongly overperforming other subwavelength imaging technology.

We develop a new mode matching approach for analysis of scattering and propagation of surface and volume modes in multiple multilayered-stack structures. Our theory relies on the complete spectrum of free-space and guided electromagnetic modes to solve Maxwell's equations in the extended systems that have relatively few interfaces. We demonstrate the convergence of this technique on a number of plasmonic and metamaterial structures.

Finally, we consider the problem of plasmonic beam-steering structures consisting of a single slit flanked by a periodic set of metallic corrugations. We show that the light emitted by the structures forms a prolonged focal range that may extend for hundreds of wavelength from the plasmonic interface and eventually splits into two plasmonic beams. We develop a quantitative theory to physically describe the beam formations and evolution of field pattern.

The numerical and analytical results presented here can be applied to several nanooptics applications including deep-subwavelength imaging, nanolithography, on-chip communications, high-density energy focusing, and beaming devices, and can be used for metamaterial and plasmonic composites operating across ultraviolet, visible, infrared, or terahertz spectra.

Computational Nanooptics in Hyperbolic Metamaterials and Plasmonic Structures

by

Sukosin Thongrattanasiri

A DISSERTATION

submitted to

Oregon State University

in partial fulfillment of

the requirements for the

degree of

Doctor of Philosophy

Presented July 22, 2010

Commencement June 2011

Doctor of Philosophy dissertation of Sukosin Thongrattanasiri presented on July 22, 2010.

APPROVED:

Major Professor, representing Physics

Chair of the Department of Physics

Dean of the Graduate School

I understand that my dissertation will become part of the permanent collection of Oregon State University libraries. My signature below authorizes release of my dissertation to any reader upon request.

Sukosin Thongrattanasiri, Author

ACKNOWLEDGEMENTS

I would like to thank my advisor, Prof. Viktor A. Podolskiy, for his effort and guidance to discipline me to be a good PhD student, a good physicist, and a good researcher. I am truly admired by his serious dedication to the study of physics and his research, and by his overwhelming supports to all of his students. He is also the motivation and model for me to work harder and harder to chase his pace.

I would like to thank one of our research group members, Nicholas A. Kuhta, for valuable discussions in various topics, and for friendship that has been kept for three years (and it will last forever). All times that we had spent together, both in office and in conferences, are very enjoyable, and will be a part of my memory.

I would like to thank my OSU teachers, William Warren, Rubin Landau, Oksana Ostroverkhova, David McIntyre, Janet Tate, William Hetherington, Tomasz Giebultowicz, Albert Stetz, David Roundy, Henri Jansen, Ethan Minot, Bokil Vrushali, Nathan Gibson, and Thomas Plant, for their dedication in classes to teach me to learn advanced physics, and how to solve problems systematically. I also thank for many valuable discussions related to my research.

I would like to thank our collaborators from Department of Electrical Engineering, Princeton University, Prof. Claire F. Gmachl and her students, Anthony J. Hoffman and Matthew D. Escarra, for the guidance and contribution to the projects of hyperbolic metamaterials, hypergrating structures, and image-retrieving technique. Also, I would like to thank Prof. Daniel M. Wasserman and his graduate student, David D. Adams, from

Department of Physics and Applied Physics, University of Massachusetts Lowell, for their criticism and contribution to plasmonic beam-steering project.

I would like to thank all American friends, Korean friends, Japanese friends, Thai friends, Wat Buddha Oregon, Tarntip Restaurant, The Siam Classical Music Ensemble, and The Siam Sentinel, for their concerns. Life of international students is sometimes tougher than local people. Almost of them have to encounter unpredictable emotional fluctuation and self-adjusting in different cultures. However, because of helps and cares of friends here, they can pass all obstacles and obtain the highest achievement of education.

I would like to thank all funding from Development and Promotion of Science and Technology Talents Project (Thailand), Office of Naval Research, National Science Foundation, Air Force Office of Scientific Research, Air Force Research Laboratory, and Department of Physics, Oregon State University.

Especially, I would like to thank my entire family members, Nattaphan, Suchart, Surinta, and Sukhothai Thongrattanasiri, and Ubonrat Theantanakhom, for their supports and advices of my study and ultimate goals. I am grateful for their encouragement in my abroad study, and for their love and patience to help me succeed this highest educational achievement.

TABLE OF CONTENTS

TABLE OF CONTENTS (Continued)

TABLE OF CONTENTS (Continued)

LIST OF FIGURES

LIST OF FIGURES (Continued)

LIST OF FIGURES (Continued)

LIST OF TABLES

LIST OF APPENDIX FIGURES

DEDICATION

แด่ มามี๊ และ ปาป๊า

ณัฐฏาพันธุ์ และ สุชาติ ทองรัตนาศิริ

Chapter 1 - Introduction of Nanooptics

Nanoscience deals with the engineering of functional systems at the molecular and atomic scales. Its original motivation is to build nanomachines – for example, motors, robot arms, and even whole computers – on the scale of molecules [1, 2]. Nanoscience research became overwhelmingly active after the discovery of fullerenes and carbon nanotubes in 1980s [3-5]. At the present time, nanoscience has covered broad areas, evolved to include both bottom-up and top-down approaches, and has provided various scientific applications, including nanomaterials [5-10], nanomedicine [11, 12], and nanoelectronics [13-17].

An important class of nanoscience called nanooptics, which we will discuss at length in this dissertation, describes light manipulation on the nanoscale, which recently has enormous influences on imaging, communication, security, and sensing applications. One of the big successes in the nanooptics field was the invention of *metamaterials*, the engineered nanostructures that can control the propagation of electromagnetic waves inside themselves [18]. The very first optical metamaterial composite consists of a periodic array of metallic wires and conducting nonmagnetic split ring resonators where their alignments and portions tune effective optical properties of the composite, leading to simultaneously negative permittivity and permeability for microwave frequencies [19-25]. When electromagnetic fields propagate inside such a structure, they encounter negative refraction, where directions of energy and wavefront (locus of points having the same phase) propagations are antiparallel. This kind of refraction has also been verified experimentally and theoretically with fishnet, chiral, and nanorod array metamaterials, and honeycomb-lattice photonic crystals in the visible and infrared spectrum [8, 9, 26-37]. Another kind of negative refraction requires strong

anisotropy of permittivity, allowing forward direction of wavefront propagation and negative refraction of energy propagation [6, 38-45].

One of the major applications in original negative refraction material is *superlens*, which is able to perfectly image objects that are placed close enough to the lens by amplifying the evanescent fields of the source [19, 46-56]. However, the resolution of image is highly sensitive to losses inside the material and the image is restricted to near field [57-60]. Another imaging device, named *hyperlens* is fabricated using interleaved metallic-dielectric multilayered metamaterial with cylindrical structure, and yields imaging magnification in far field [14, 61-68].

The flexibility of designing effective optical properties inside metamaterials leads to the controlling of light propagation which may not be found in nature [18, 69-72]. A mathematical approach, called *transformation optics*, transforms initial configuration of electromagnetic fields on the Cartesian mesh to a specific coordinate system where light can propagate as designed. One achievement of this mapping technique is represented by the *cloaking device*, where its engineered coordinate is designed to bend electromagnetic waves around a concealed volume, and return the waves to their original trajectory [73-83]. It can be assumed that no radiation leaves and enters the concealed volume of space; so that, an object of arbitrary shape is invisible inside the volume. Transformation optics has also been extended to model celestial mechanics, general relativity, and even optical black holes inside metamaterials [84-91].

Nanophotonics of surface plasmon polaritons is another important class of nanooptics technology, where the physics of confined surface waves at a metal-dielectric interface is studied [92-99]. It has been known that in present electronic devices, the speed of information

transfer is restricted by the speed and mass of electrons, leading to high losses of energy due to heat inside circuits. Therefore, surface plasmon polaritons have been proposed as a means of data transfer for on-chip devices, due to their extremely high frequencies. Recently, researches in surface plasmons have been pointed interests to extraordinary transmission by a single slit [100-106]. When the slit is surrounded by a set of metallic grooves on the input side, the transmitted field is enhanced by surface plasmon polaritons induced by the periodic corrugation. Such a phenomenon is not found in the single slit without a corrugation surface. On the other hand, if periodic corrugation is installed on the output side of the slit, the transmitted field is confined in some directions, allowing directional control of light beams [107-114]. This beam-steering device can be applied to on-chip communications which transfer photonic signals.

In this dissertation, we will develop physical insight for important problems in the nanooptics field, including broadband negative refraction, subwavelength imaging, surface plasmon scattering, and directional optical beaming. In Chapter 2, we will theoretically present mathematical conditions for negative refraction inside strongly anisotropic metamaterials and designs of broadband and flat response negative-refraction spectrum will be represented. The theory was supported by the experiments, performed by our Princeton University (PU) collaborators. This proposal leads to understanding of designing broadband response in applications of cloaking and imaging metamaterial devices. In Chapter 3, we will propose the structure, named *hypergrating*, which employs a subwavelength Fresnel diffraction plate for generating high-wavevector information, and a strongly anisotropic metamaterial to propagate high-resolution signal to the far field. Consequently, hypergratings introduce new type of subwavelength imaging devices, nanolithography, or even optical communications with high spatial resolution.

A mathematical algorithm used to image subwavelength objects with the far-field measurement will be presented in Chapter 4. The general mechanism is to use a subwavelength diffraction grating behaving as an optical device, to shift high-transverse-wavevector signal of an object into the propagating regime which is detectable in the far field. Later, the mathematical formulation is used to deconvolute original propagating signals and originally evanescent signals. Moreover, we will illustrate that the technique can classify the shape and size of objects that are much smaller than the wavelength of incident light. This approach offers a new low-cost technique to image subwavelength objects using planar-structure fabrication. In Chapter 5, a new wave-matching method will be developed to numerically compute electromagnetic fields inside planar structures. The method is extremely memory efficient when compared with the finite-element and finite-difference time-domain algorithms. The method will be applied to the problem of control of surface plasmon scattering and modal cross-talk in planar waveguide structures. We will also show the robustness of our approach in several photonic and plasmonic applications. Chapter 6 will be devoted to a theoretical model which is used to predict directions of beams in plasmonic beam-steering structures. We will confirm the robustness of our model with analytical, finite-element simulations, and experimental results obtained from our University of Massachusetts (UMass) collaborators.

Chapter 2 - Hyperbolic Optical Metamaterial

2.1 Introduction

An optical metamaterial is an artificial medium engineered to provide effective optical properties which may not be found in nature. A composite consists of nanostructured components aligned in a periodic pattern. On the microscopic scale, electromagnetic fields interact with each individual constituent, and consequently the microscopic electric and magnetic fields are inhomogeneous. However, the macroscopic electric field and polarization can be obtained by averaging the microscopic electromagnetic fields and local dipole moments over the groups of constituents, leading to the macroscopic optical properties of the composite, for example, electrical conductivity, permittivity, and permeability.

The origin of the overwhelming interest in the metamaterial research started from theoretical possibility of perfect imaging by a slab of *negative index material*, whose both permittivity ε and permeability μ are simultaneously negative [19, 115]. Since then, several negative index metamaterial designs have been proposed [20-25]. However, the metamaterials require the overlapping resonances in permittivity and permeability, leading to the complication of metamaterial design and fabrication [20-25]. Furthermore, the metamaterials are highly lossy due to the dissipation at the resonances [116-118], significantly reducing the resolution of imaging [57-60].

Another class of negative refraction employs a uniaxial anisotropic medium having the hyperbolic form of the dispersion relation [6, 38-45, 119-124]. Such a material requires only a single resonance and hence the optical loss is significantly reduced, and more importantly negative refraction spectrum is not limited by double resonances. Here we design

semiconductor multilayered composites, which exhibit negative light refraction in mid-infrared frequency regime. The planar structure provides many fabrication advantages and can be easily adapted to current industrial techniques.

This Chapter is organized as follows. In Section 2, we will derive the refraction properties of the electromagnetic field inside a hyperbolic material, and will show how the hyperbolic material can transfer high-wavevector signals to the far field. Later, an effective medium theory used in averaging field properties to calculate the effective optical quantities, will be described. In Section 3, we will study theoretically negative light refraction in the semiconductor nanolayered structure, comprising interleaved highly doped InGaAs and undoped AlInAs nanolayers. The simulations are in good agreement with experimental results, obtained from our PU collaborators. To reduce the dispersion of effective dielectric constant tensor, the design of the broad bandwidth and flat response of negative refraction in such heterostructures will be presented in Section 4. The agreement between simulation and experimental results will be confirmed.

2.2 Wave Propagation in Hyperbolic Metamaterial

In this Section, we will present an overview of the mathematical description of light propagation in anisotropic materials that will be used throughout this dissertation. We will setup Maxwell's equations for general uniaxial anisotropic materials, named birefringent media [116], in the Cartesian coordinate system, and the conditions for the hyperbolic dispersion relation will be presented. The solutions of Maxwell's equations show uncommon relation of energy and phase propagation in such the hyperbolic material, yielding positive and negative wave refractions. Even though hyperbolic materials are found in nature [42, 43], the losses inside those materials are very high for realistic applications and the changes in their

crystal structures are sensitive to the environmental stimulations. However, it is possible to artificially make the low-loss and structurally-strong hyperbolic metamaterials. Effective medium theory (EMT) will be employed to design the optical properties of the metamaterials.

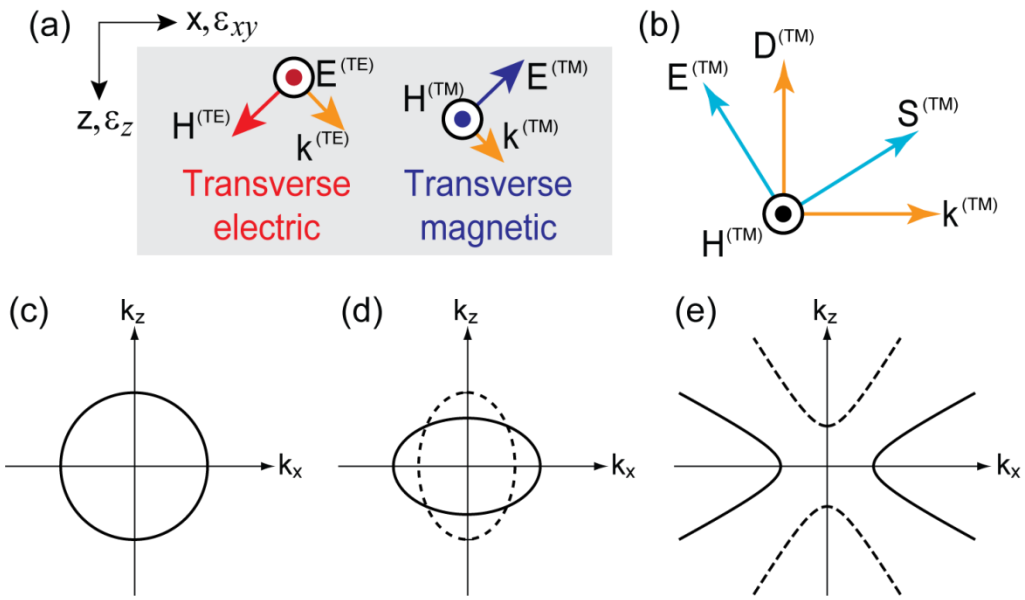

FIGURE 2.1: (a) Cartesian coordinate of the structure; the optical axis is parallel to z axis; arrows show directions of electric and magnetic fields and wavevectors for TE- and TM-polarized light; (b) relation of all electromagnetic vectors for TM-polarized wave; $\vec{k} \perp \vec{D} \perp \vec{H}$ and $\vec{S} \perp \vec{E} \perp \vec{H}$; (c) illustration of isotropic dispersion relation [Eq. (2.7)] when TE-polarized filed propagates inside a uniaxial material (assuming no loss); radius of circle is $\sqrt{\varepsilon'_{xy}}\omega/c$; (d) dispersion relation Eq. (2.8) encounters elliptic form when $\varepsilon'_{xy} \neq \varepsilon'_z$; solid and dashed curves correspond to $\varepsilon'_z > \varepsilon'_{xy} > 0$ and $\varepsilon'_{xy} > \varepsilon'_z > 0$ cases (assuming no loss); (e) hyperbolic dispersion relation occurs when either ε'_{xy} or ε'_z is negative (assuming no loss); solid and dashed curves correspond to $\varepsilon'_{xy} < 0 < \varepsilon'_z$ (positive refraction) and $\varepsilon'_z < 0 < \varepsilon'_{xy}$ (negative refraction) cases; in the positive refraction case, propagation condition yields $k'_x > \sqrt{\varepsilon'_z}\omega/c$; in contrast, the negative refraction case can cover all k'_x spectra.

2.2.1 Maxwell's Equations and Dispersion Relations

Maxwell's equations for a nonmagnetic uniaxial medium for a monochromatic wave are given by [116-118]

$$\vec{k} \cdot \hat{\varepsilon}\vec{E} = 0\,, \tag{2.1}$$

$$\vec{k} \cdot \vec{H} = 0\,, \tag{2.2}$$

$$\vec{k} \times \vec{E} = \frac{\omega}{c}\vec{H}\,, \tag{2.3}$$

$$\vec{k} \times \vec{H} = -\frac{\omega}{c}\hat{\varepsilon}\vec{E}\,, \tag{2.4}$$

where

$$\hat{\varepsilon} \doteq \begin{bmatrix} \varepsilon_{xy} & 0 & 0 \\ 0 & \varepsilon_{xy} & 0 \\ 0 & 0 & \varepsilon_z \end{bmatrix} \tag{2.5}$$

is a dielectric constant tensor of the uniaxial material, ω is the angular frequency of light, c is the speed of light in air, and $\vec{k} = \{k_x, k_y, k_z\}$ is wavevector of light [Fig. 2.1]. Here the optical axis (O.A.), representing the direction of the material symmetry, is perpendicular to the xy-plane, and the electromagnetic fields depend on $\exp[i(\vec{k} \cdot \vec{r} - \omega t)]$. These conditions will be used throughout this dissertation. Maxwell's equations are reduced to the wave equation given by

$$\vec{k}(\vec{k} \cdot \vec{E}) - k^2\vec{E} = -\frac{\omega^2}{c^2}\hat{\varepsilon}\vec{E}\,. \tag{2.6}$$

Note that for the isotropic medium, the first term on the left-hand side vanishes, and Eq. (2.6) yields the spherical form of the dispersion relation [116]. The so-called anisotropic wave

equation [Eq. (2.6)] can be written as a system of linear equations for the electric field components, and the nontrivial solutions exist when

$$k_x^2 + k_y^2 + k_z^2 = \varepsilon_{xy}\frac{\omega^2}{c^2} \tag{2.7}$$

or

$$\frac{k_x^2 + k_y^2}{\varepsilon_z} + \frac{k_z^2}{\varepsilon_{xy}} = \frac{\omega^2}{c^2}. \tag{2.8}$$

In the case of light propagating on the xz plane ($k_y = 0$) [Fig. 2.1(a)], Maxwell's equations and Eq. (2.7) allow possible field components: $\vec{E} = \{0, E_y, 0\}$ and $\vec{H} = \{H_x, 0, H_z\}$. Such a wave is called "transverse electric (TE)" or "ordinary" polarized electromagnetic field, and its "circular" dispersion relation [Eq. (2.7)] relating all possible k_x and k_z to ε_{xy} and ω, is illustrated in Fig. 2.1(c). The waves with this polarization behave as electromagnetic fields propagating inside an isotropic medium; both wavevector (direction perpendicular to wavefronts) and Poynting vector (direction of energy propagation) $(\vec{S}_{TE})$, are related by

$$\vec{S}_{TE} = \frac{c^2}{4\pi\omega}\left|E_y\right|^2\{k_x, 0, k_z\}, \tag{2.9}$$

and have the same direction. Consequently, the directions of wavefront and energy propagations are co-parallel.

On the other hand, another polarization, called "transverse magnetic (TM)" or "extraordinary" electromagnetic wave, consists of the field components: $\vec{E} = \{E_x, 0, E_z\}$ and $\vec{H} = \{0, H_y, 0\}$, and its dispersion relation Eq. (2.8) relates k_x and k_z to ε_{xy}, ε_z, and ω. The Poynting vector $(\vec{S}_{TM})$ is related to wavevector by

$$\vec{S}_{TM} = \frac{c^2}{4\pi\omega}\left|H_y\right|^2\left\{\frac{k_x}{\varepsilon_z}, 0, \frac{k_z}{\varepsilon_{xy}}\right\}. \tag{2.10}$$

Note that for TM-polarized field, both wavevector and Poynting vector, and both $\vec{D}$ and $\vec{E}$ are nonparallel. Their relations are illustrated in Fig. 2.1(b). Apparently, in a uniaxial material for a TM-polarized field, wavefronts and energy propagate in different directions.

2.2.2 Refraction Laws: Positive and Negative Refractions

Now we may classify combination of ε_{xy} and ε_z into two groups: (i) both ε'_{xy} and ε'_z are positive quantities, and (ii) either ε'_{xy} or ε'_z is negative but not both. Note that notations $'$ and $''$ denote real and imaginary parts of a complex number quantity, respectively, and they will be used throughout this dissertation.

The dispersion relation of the material in the group (i) has the elliptical form, shown in Fig. 2.1(d). The solid and dashed curves correspond to $\varepsilon'_z > \varepsilon'_{xy} > 0$ and $\varepsilon'_{xy} > \varepsilon'_z > 0$ cases, respectively. The medium can be found plentifully in nature, for instance, calcite, quartz, and ruby crystals [125, 126]. Applications include beam splitter, liquid crystal displays, light modulators, color filters, wave plates, and optical axis gratings [127-130].

The group (ii) is the primary focus of this dissertation. When one of permittivities in Eq. (2.8) is negative, mathematically the dispersion relation has the hyperbolic form, and each hyperbola belongs to each negative permittivity. Specifically, negative ε'_{xy} gives the east-west opening hyperbola, and negative ε'_z gives the north-south opening hyperbola [38-41] [Fig. 2.1(e)]. The peculiar behaviors of propagation of TM-polarized waves inside hyperbolic media are clearly seen when considering propagation from an isotropic material into a strongly anisotropic material.

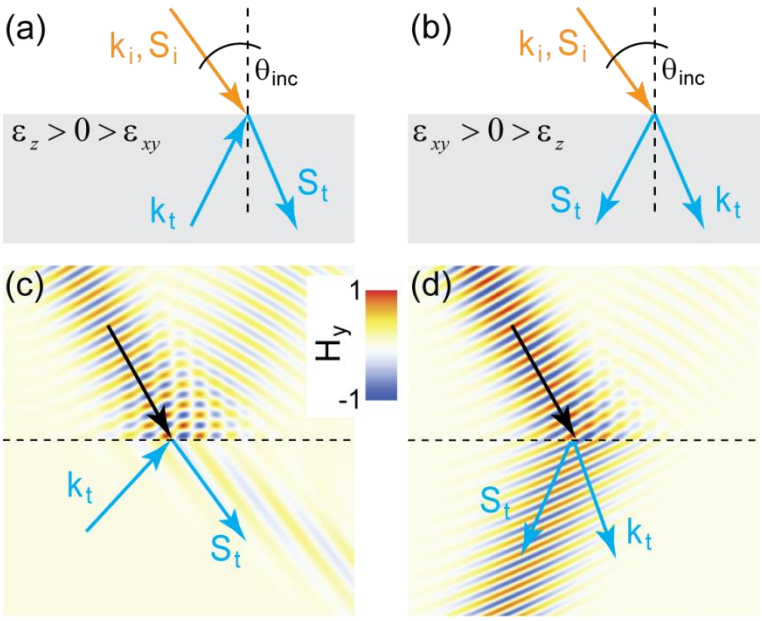

FIGURE 2.2: Schematics representing the transmitting wavevector $(\vec{k}_t)$ and Poynting vector $(\vec{S}_t)$ for (a, c) positive and (b, d) negative refractions; (a, b) arrows of reflecting $\vec{k}$ and $\vec{S}$ are not shown; (c, d) full numerical calculations demonstrating positive and negative refractions of a monochromatic TM-polarized Gaussian beam across an air-metamaterial interface.

Let us setup the system as follows: a TM-polarized wave of wavelength λ_0 propagates from air to a hyperbolic material, either $\varepsilon'_{xy} < 0 < \varepsilon'_z$ or $\varepsilon'_z < 0 < \varepsilon'_{xy}$ case, with arbitrary incident angle θ_{inc} [Fig. 2.2]. The propagation of the refracted fields inside the hyperbolic materials can be analyzed by employing the Poynting vector-wavevector relation [Eq. (2.10)], with the requirements of conservation of transverse component of the wavevector and energy flowing in the forward direction ($S'_z > 0$). Hence, in the case of $\varepsilon'_{xy} < 0 < \varepsilon'_z$ material [38-41] we need to choose $k'_z < 0$ and $k'_x > \sqrt{\varepsilon'_z}\omega/c$. As a result, the wave transmits into the hyperbolic dielectric with *backward* wavefront propagation ($k'_z < 0$) with respect to the interface and exhibits *positive* refraction ($S'_x > 0$) [Fig. 2.2(a)]. In contrast, materials of the $\varepsilon'_z < 0 < \varepsilon'_{xy}$ permittivities [38-41] allow wave propagation when $S'_x < 0$ and $k'_z > 0$; so that

transmitted wave encounters *negative* refraction and *forward* wavefront propagation [Fig. 2.2(b)]. Both circumstances are very essential for imaging, high resolution transfer device and nanolithography, which will be mentioned later in Section 2.2.3. Full numerical calculations demonstrating positive and negative refractions of a monochromatic TM-polarized Gaussian beam across an air-metamaterial interface are shown in Fig. 2.2 (c, d).

In an anisotropic material, the Poynting vector and wavevector have different directions; their directions depend on the effective group (n_g) and phase (n_p) indices of refraction, respectively. The group index is obtained from Snell's law, giving the continuity of the transverse Poynting vectors at the interface:

$$n_0 \sin\theta_{inc} = n_g \sin\theta_g \,, \tag{2.11}$$

where $n_0 = \sqrt{\varepsilon_0}$ is index of refraction of air, ε_0 is permittivity of air, and θ_g corresponds to the direction of transmitted Poynting vector, respective to the optical axis. Similarly, the phase index is obtained from Snell's law, giving the continuity of the transverse wavevectors at the interface:

$$n_0 \sin\theta_{inc} = n_p \sin\theta_p \,, \tag{2.12}$$

where θ_p is angle of the transmitted wavevector, respective to the optical axis. Consequently, the group and phase indices of refraction are represented as

$$n_g = \frac{\varepsilon_z}{\varepsilon_{xy}} \sqrt{\varepsilon_{xy} - \frac{\varepsilon_{xy}}{\varepsilon_z}\left(1 - \frac{\varepsilon_{xy}}{\varepsilon_z}\right)\varepsilon_0 \sin^2\theta_{inc}} \,, \tag{2.13}$$

$$n_p = \sqrt{\varepsilon_{xy} + \left(1 - \frac{\varepsilon_{xy}}{\varepsilon_z}\right)\varepsilon_0 \sin^2\theta_{inc}} \,, \tag{2.14}$$

Surprisingly, contrary to the conventional isotropic refractive index, both group and phase indices of refraction depend on the angle of incidence. The $\varepsilon'_{xy} < 0 < \varepsilon'_z$ hyperbolic material gives positive n_g and negative n_p, yielding positive energy refraction and backward wavefront propagation as mentioned earlier. The opposite case ($\varepsilon'_z < 0 < \varepsilon'_{xy}$) gives negative n_g and positive n_p allowing negative energy refraction and forward wavefront propagation for all angles of incidence [131]. Negative refraction by hyperbolic metamaterials has been shown in experiments in the UV, optical, and mid-IR spectra [6, 44, 45, 119, 120]; applications include broadband Purcell effect [132-134], imaging hyperlens [14, 61-66], waveguiding [12, 42, 43, 135], out-of-plane scattering elimination [136, 137], and on-chip light-communication [16, 17].

The other crucial quantities for bulk hyperbolic metamaterials are Fresnel coefficients [116], describing the fractions of the incident light that will be reflected from or transmitted through the air-metamaterial interface. For TM-polarized illumination, the reflecting (r_{TM}) and transmitting (t_{TM}) coefficients computed by the ratio of H_y components, are expressed as

$$r_{TM} = \frac{\varepsilon_z \tan\theta_g - \varepsilon_0 \tan\theta_{inc}}{\varepsilon_z \tan\theta_g + \varepsilon_0 \tan\theta_{inc}}, \tag{2.15}$$

$$t_{TM} = \frac{2\varepsilon_z \tan\theta_g}{\varepsilon_z \tan\theta_g + \varepsilon_0 \tan\theta_{inc}}, \tag{2.16}$$

where the refracted angle, $\tan\theta_g = S_x/S_z$, is defined as the ratio of different components of Poynting vector. The fractions of the incident power that is reflected from and refracted through the interface are given by the reflectance (R_{TM}) and transmittance (T_{TM}), and are related to Fresnel coefficients by $R_{TM} = |r_{TM}|^2$ and $T_{TM} = \mathbb{R}\mathrm{e}\left(k_{z,g}/\varepsilon_{xy}\right)/\mathbb{R}\mathrm{e}\left(k_{z,inc}/\varepsilon_0\right)|t_{TM}|^2$, respectively. The incident plane wave can encounter phenomena observed in a

conventional isotropic medium, for instance, total internal reflection and minimum of TM-polarized reflection at Brewster's angle.

Table 2.1 summarizes all necessary information for TM- and TE-polarized light propagating inside hyperbolic metamaterials. The information will be invoked again in the rest of the dissertation.

TABLE 2.1: Summary of important information when TE- and TM-polarized fields, illuminated from air, propagate inside hyperbolic metamaterials.

Polarization	Dispersion Relation	Hyperbolic Metamaterials	
		$\varepsilon'_{xy} < 0 < \varepsilon'_z$	$\varepsilon'_z < 0 < \varepsilon'_{xy}$
TE	$\frac{k_x^2+k_z^2}{\varepsilon_{xy}} = \frac{\omega^2}{c^2}$	No Wave Propagation	*Forward* Wavefront *Positive* Refraction
TM	$\frac{k_x^2}{\varepsilon_z} + \frac{k_z^2}{\varepsilon_{xy}} = \frac{\omega^2}{c^2}$	*Backward* Wavefront *Positive* Refraction	*Forward* Wavefront *Negative* Refraction

2.2.3 Resolution of an Image

Another unusual characteristic of hyperbolic materials that goes beyond conventional isotropic media is the propagation of high-wavevector-spectrum field components, which contain subwavelength information which is necessary for high image resolution [14, 16]. In this Subsection, we will prepare the physical understanding of image resolution limitations when an object is placed in an isotropic medium. We will later show that a hyperbolic material can achieve deep subwavelength resolution.

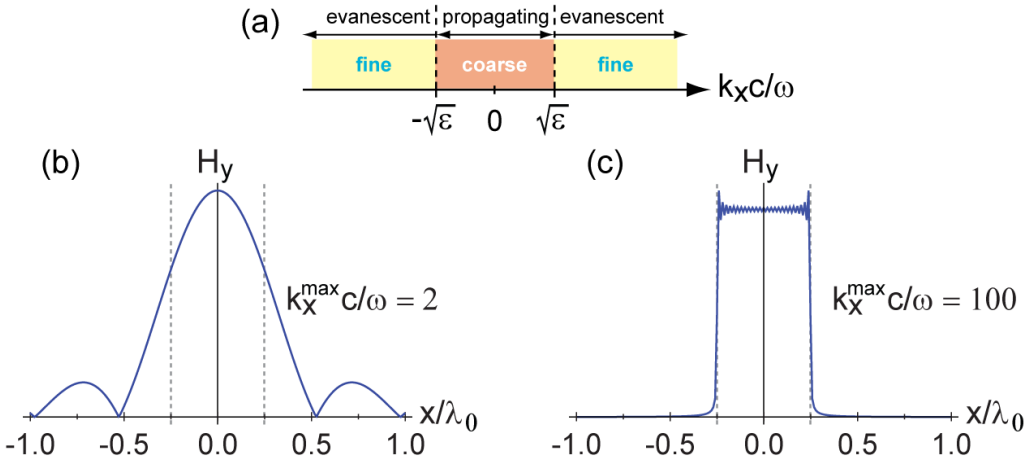

FIGURE 2.3: (a) Schematic of wavevector spectrum illustrating the separation of propagating and evanescent regimes of an isotropic medium with permittivity ε; the coarse and fine image details are kept in propagating and evanescent spectrum, respectively; (b, c) the retrieval of a subwavelength single slit with width $\lambda_0/4$ when (b) $k_x^{max} = 2\omega/c$ and (c) $k_x^{max} = 100\omega/c$; the dashed lines show the original size of the slit; the measurements are performed at the same distance z from the slit.

Let us consider a subwavelength object placed in an isotropic medium with permittivity ε. The object can be written as a Fourier function, $H_y(x,z)$, constructed from broad range of transverse-wavevector components, k_x [138]:

$$H_y = \int_{-\infty}^{+\infty} dk_x \, \tilde{H}_y(k_x) e^{ik_x x} e^{ik_z(k_x) z} \tag{2.17}$$

where $\tilde{H}_y(k_x)$ contributes to the field amplitude for each k_x, and $k_z(k_x) = \sqrt{\varepsilon\omega^2/c^2 - k_x^2}$ representing the spherical dispersion relation [Eq. (2.7)], classifies the type of field transfers. Assuming the isotropic material is lossless, the wavevector spectrum may be separated into two regimes: propagating $\left(|k_x| \leq \sqrt{\varepsilon}\omega/c\right)$ and evanescent $\left(|k_x| > \sqrt{\varepsilon}\omega/c\right)$ [Fig. 2.3(a)]. The wavevector governing the propagating regime can be detected in the far field; in contrast, the wavevector governing the evanescent regime is only measurable in the near field. The

resolution of an image that each wavevector keeps can be described as $\sim 2\pi/k_x$. Therefore, the propagating regime occupies low-wavevector-spectrum values, and stores coarse-resolution details, while the evanescent regime occupies high-wavevector-spectrum values, and stores fine-resolution details [Fig. 2.3(a)]. As a result, a conventional optical microscope cannot image a subwavelength object with the resolution beyond about $\lambda_0/2$, because it only retrieves the coarse information [139].

We illustrate the resolution limitation of the conventional microscope with a single slit of width $\lambda_0/4$ in air. Fig. 2.3(b) illustrates the retrieval of the subwavelength single slit when $k_x^{max} = 2\omega/c$ is measured in the far-field. It is clearly seen that this maximum wavevector only contains propagating values, that the subwavelength resolution cannot be achieved. However, it is possible to use a hyperbolic material, whose dispersion relation has open hyperbolas with a broader k_x range [Eq. (2.8)], to transfer high-wavevector-components (subwavelength information) into the far field. Fig. 2.3(c) illustrates the complete retrieval of the single slit placed in a lossless hyperbolic material when $k_x^{max} = 100\omega/c$ is included in calculation.

Therefore, hyperbolic materials, which can support high-wavevector-spectrum propagation, are capable of providing subwavelength imaging and nanolithographic techniques. Moreover, the hyperbolic materials posses a broad bandwidth singularity in the photonic density of states; hence they are also a good candidate for enhancing the spontaneous emission of a light source [132-134]. In the next Subsection, we will employ the effective medium theory (EMT) [140-143] to design effective optical properties of the hyperbolic metamaterials; such a media can be fabricated using present technology.

2.2.4 Effective Medium Theory

Effective medium theory is an approach for computing macroscopic properties of a composite from the microscopic properties and relative fractions of its constituents. The first traditional EMT models for application in the optical regime was proposed by J.C. Maxwell Garnett, where optical properties of a medium containing minute metallic spheres were examined [140]. More recently theory developed by Von D.A.G. Bruggeman treats two composites in a symmetrical fashion [141]. Moreover, modern applications allow the approximation of the optical properties of nanocrystals embedded in a crystalline matrix [144-146], and nanolayered and nanowire structures [41, 147, 148].

Nanolayered and nanowire structures are among most important compositions used to design the dielectric constant tensor in hyperbolic metamaterials. The approximation is restricted in the sense that the size of the inclusions, either nanolayer thickness or nanowire radius, should be much smaller than the wavelength; in consequence, the radiation cannot distinguish the collection of elements from the homogeneous material. Therefore, macroscopic electric and displacement fields are obtained from averaging local electric and local displacement fields inside the composites. The effective dielectric constant tensor $\varepsilon_{\alpha\beta}$ results from the ratio of components of the average displacement $\langle D\rangle_\alpha$ and the average electric field $\langle E\rangle_\beta$:

$$\langle D\rangle_\alpha = \varepsilon_{\alpha\beta}\langle E\rangle_\beta \tag{2.18}$$

where the bracket $\langle \quad \rangle$ represents spatial averaging of the material quantities for microscopic scales over macroscopic compositions, and the indices α and β represent summation in Cartesian coordinates.

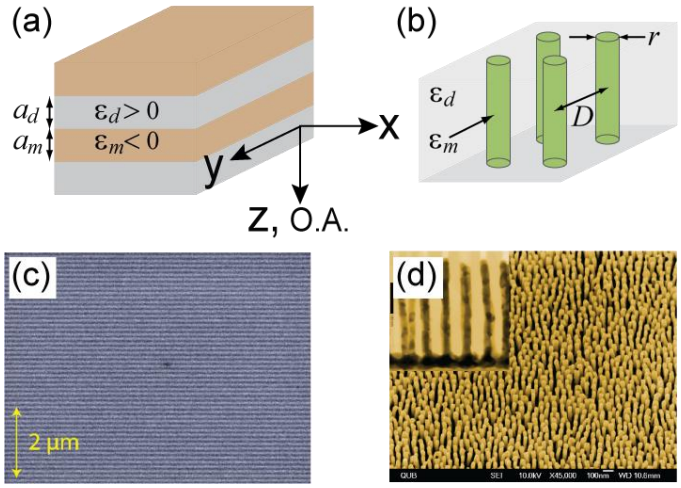

FIGURE 2.4: (a, c) Nanolayered structures consist of interleaved layers of metal and dielectric of thicknesses and permittivities a_m, ε_m and a_d, ε_d; the formation of layers is aligned along to the optical axis (O.A.); (b, d) nanowire structures consist of metallic wires of radius r with center-to-center distance D embedded in the dielectric host; (c, d) scanning electron microscope (SEM) images of (c) InGaAs/AlInAs nanolayered structure [6] and (d) Au/Al_2O_3 nanowire structure [123]; reprinted with permission from Ref. [6] (c) and Ref. [123] (d).

For the two-dimensional nanolayered metamaterial, a structure is comprised of multiple interleaved layers of metal and dielectric perpendicular to the optical axis; layer thickness and permittivity are a_m, ε_m for metal and a_d, ε_d for dielectric [Figs. 2.4(a, c)]. The EMT yields the effective permittivities as [41, 117, 140]

$$\varepsilon_{xy} = \frac{a_m\varepsilon_m + a_d\varepsilon_d}{a_m + a_d}, \tag{2.19}$$

$$\varepsilon_z = \frac{\varepsilon_m\varepsilon_d(a_m + a_d)}{a_m\varepsilon_d + a_d\varepsilon_m}. \tag{2.20}$$

The effective optical properties can be tuned to obtain the hyperbolic dispersion. However, the efficiency of the EMT is controlled by a_m, $a_d \ll \lambda_0$ where λ_0 is the free-space wavelength. Eqs. (2.19) and (2.20) are viewed as a formula relating the bulk dielectric constant tensor $\hat{\varepsilon}$ in terms of its constituents ε_m which form inclusions of volume fraction $N = a_m/(a_m + a_d)$ in

the host ε_d. The multilayered sandwich structure of doped $In_{0.53}Ga_{0.47}As$ and undoped $Al_{0.48}In_{0.52}As$ semiconductor layers, and a curved periodic stack of Ag and Al_2O_3 have been shown in the experiments demonstrating negative refraction of TM-polarized light in UV, visible, and mid-IR spectra [6, 64, 119, 120].

Another composition is the nanowire structure, consisting of metallic nanorods embedded in the dielectric template matrix [Figs. 2.4(b, d)]. The composite can be fabricated with electrochemistry [7]. The controllable parameters of the effective optical properties are metallic nanorod radius r, metallic permittivity ε_d, average separation distance between each wire D, and membrane dielectric permittivity ε_d. Letting the optical axis be parallel to the alignment of nanorods, the effective permittivities are given by [41, 140, 147]

$$\varepsilon_{xy} = \frac{\frac{2\varepsilon_m\varepsilon_d}{\varepsilon_m+\varepsilon_d}N + \varepsilon_d(1-N)}{\frac{2\varepsilon_d}{\varepsilon_m+\varepsilon_d}N + (1-N)}, \tag{2.21}$$

$$\varepsilon_z = \varepsilon_m N + \varepsilon_d(1-N), \tag{2.22}$$

where $N = \pi r^2/D^2$ is the inclusion factor. Note that the efficiency of EMT requires $N \ll 1$ and D, $r \ll \lambda_0$. The hyperbolic dispersion has been shown experimentally in Refs. [44, 45, 121, 122] with the compositions of Ag/Al_2O_3, Au/Ta_2O_5, and Au/Al_2O_3, operated at UV, visible, and near-IR frequencies.

Note that for the nanowire structures, the effective optical properties described above originates from the averaged microscopic properties of the constituents. Hence, the desired response does not require any periodicity of the constituent arrangement and only the average concentration has to be controlled during the fabrication step.

2.3 Semiconductor Metamaterial

Here we demonstrate numerically negative refraction behavior for the mid-IR TM-polarized illumination in the multilayered structure of all-semiconductor composites. Later, the correctness of the simulations is confirmed by the experimental results, performed by our PU collaborators. The advantages of the structure are that it has remarkably low-loss and optically-thick planar structure, and also employs the single epitaxial growth process available in the present nanofabrication technology.

Similar to Refs. [6, 120], the multilayered stack of total thickness $L = 12\,\mu m$, comprised of interleaved layers of $In_{0.53}Ga_{0.47}As$ and $Al_{0.48}In_{0.52}As$, each $80\,nm$-thick, is placed on the $620\,\mu m$-thick lattice-matched InP substrates ($\varepsilon_{InP} = 9.61$), and the light is illuminated on the interleaved-layers side. The undoped AlInAs layers are treated as dielectric media with permittivity $\varepsilon_{\infty-AlInAs} = 10.23$ [149]. The InGaAs layers are uniformly highly doped by Si to provide plasma free carriers, and then behave as metallic inclusions. The permittivity of the doped InGaAs layers is expressed by Drude model [117, 118]:

$$\varepsilon_{InGaAs} = \varepsilon_{\infty-InGaAs}\left[1 - \frac{\omega_p^2}{\omega(\omega + i\,\tau)}\right], \tag{2.23}$$

$$\omega_p^2 = \frac{4\pi e^2 N_d}{m^*_{InGaAs}\,\varepsilon_{\infty-InGaAs}}, \tag{2.24}$$

where $\varepsilon_{\infty-InGaAs} = 12.15$ is the high frequency permittivity of InGaAs, $\tau = 10^{13}\,s^{-1}$ represents the electromagnetic losses due to damping by inelastic scattering inside the material, $e = 4.8 \times 10^{-10} esu$ is electron charge, $m^*_{InGaAs} = 3.89 \times 10^{-29} g$ is effective mass of electrons in InGaAs layers, and ω_p is the plasma frequency depending on the doping concentration N_d of cm^{-3} unit. Consequently, the effective dielectric constant tensor can be

computed by Eqs. (2.19) and (2.20), and the range of wavelengths corresponding to negative refraction is tuned by adjusting the doping density in the InGaAs layers.

The dependence of the calculated permittivities ε_{xy} and ε_z on wavelengths for free-electron density $N_d = 8.3 \times 10^{18}\, cm^{-3}$ is illustrated in Fig. 2.5(a, b); corresponding plasma frequency is $2.26 \times 10^{14}\, s^{-1}$ which is in the infrared spectrum. The high imaginary part of ε_z around $11.3\, \mu m$ is due to the plasma resonance in the highly doped InGaAs layers. The spectral region, where the metamaterial exhibits negative refraction, is shaded by the yellow band. The onset of negative refraction occurs at the critical wavelength $\lambda_c = 8.37\, \mu m$, when $\varepsilon_z' = 0$. For the smaller wavelength $\lambda_0 < \lambda_c$, the metamaterial behaves as the conventional uniaxial anisotropic material. However, beyond the negative refraction spectrum the metamaterial exhibits positive refraction. Note that for this typical doping concentration, both ε_{xy} and ε_z encounter negative values at approximately $\lambda_0 = 11.31 - 11.35\, \mu m$. The absorption coefficient, $\alpha_{TM} \approx -\ln\big(T_{TM}/(1 - R_{TM})\big)/L$, and the figure of merit, FOM= k_z'/k_z'', are shown in Fig. 2.5(c) for various wavelengths and incident angles. T_{TM} and R_{TM} are the TM transmittance and reflectance, respectively. The strong peaks around the critical wavelength arise from high imaginary parts of k_z, relating to losses inside the material and the real part of ε_z vanished. We also compute the shift (Δx) of the laser beam with 5° angle of incidence transmitting through the metamaterial using the ray-tracing method for various wavelengths [Fig. 2.5(d)]. It is clearly seen the negative shift in the negative refraction spectral region.

To obtain experimental verification of negative refraction, our PU collaborators performed reflectance (R) and transmittance (T) measurements with incident TM- and TE-polarized illumination as a function of incident angles and wavelengths. For transmittance

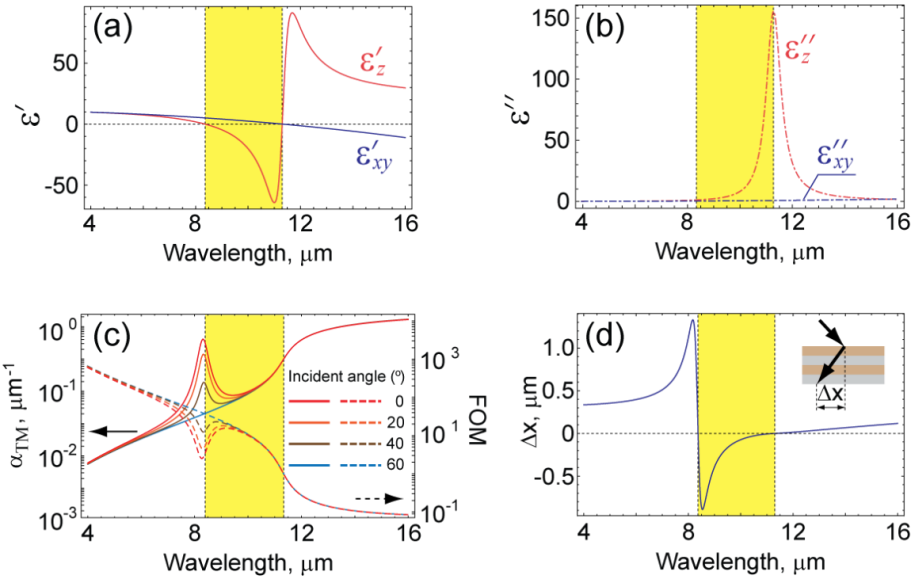

FIGURE 2.5: (a) Real and (b) imaginary parts of ε_{xy} and ε_z for $N_d = 8.3 \times 10^{18}\ cm^{-3}$ as a function of wavelength; the yellow band covers negative refraction spectra; (c) absorption coefficient (solid curves corresponding to the left vertical axis) and FOM (dashed curves corresponding to the right vertical axis) as a function of wavelength and incident angle, are plotted on the log scale; plots show 0, 20, 40, and 60 degrees of incident angles; (d) shift (Δx) of transmitted fields behind the metamaterial for 5 degree angle of incidence; negative shift is in the yellow band; the inset shows definition of the shift.

measurements, the ratio of the TM and TE transmittance is taken to reduce environmental fluctuations [Fig. 2.6(a)]. The strong absorption dip around $8\,\mu m$ is observed; the dip corresponds to high imaginary parts of k_z. For the separated TM and TE transmittance plots [Figs. 2.6(c, e)], the overall decrease in transmission with increasing wavelengths for each angle of incidence is due to k_z'' inside the metamaterials [Fig. 2.5(c)]. In addition, it also appears the strong dip around $8\,\mu m$ in the TM transmittance plot [Fig. 2.6(c)]; the dip is not observed in the TE transmittance plot [Fig. 2.6(e)]. Note that the critical wavelengths from experiment and calculation are slightly different; this deviation occurs from variation of the experimental doping concentration.

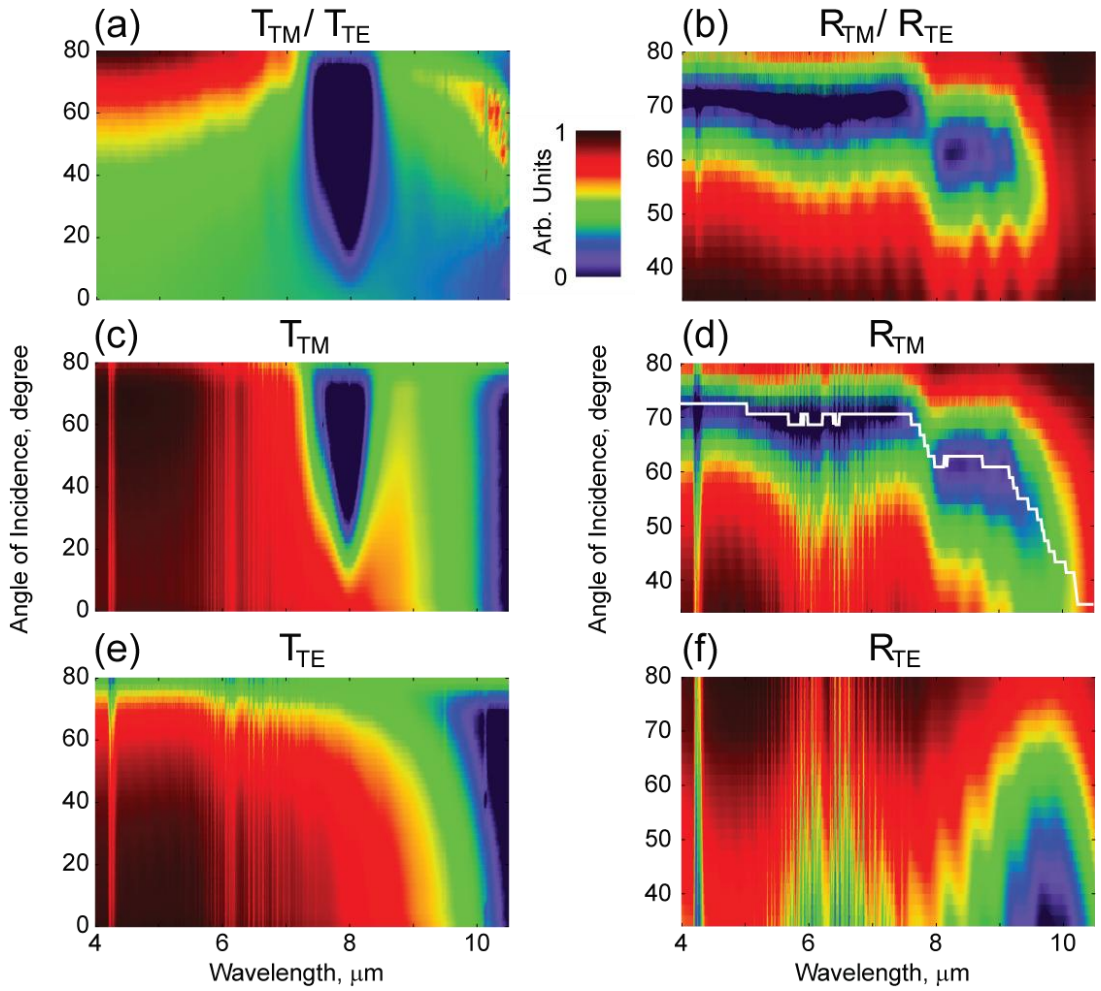

FIGURE 2.6: Experimental transmission and reflection measurements for various wavelengths and incident angles; critical wavelength for the doping density $N_d = 8.3 \times 10^{18}\, cm^{-3}$ is expected at 8.37 μm; each plot illustrate (a) T_{TM}/T_{TE}, (b) R_{TM}/R_{TE}, (c) T_{TM}, (d) R_{TM}, (e) T_{TE}, and (f) R_{TE}; the strong dips in (a) and (c) represent experimental critical wavelength at around 8 μm; no dip occurs in TE-polarized transmission plot (e); (e) small transmission of TE-polarized fields occurs after 10 μm due to negative real part of ε_{xy}; (b, d) discontinuity of Brewster's angle trace (solid white curve in R_{TM} plot) occurring at critical wavelength, is the feature of the transition of normal positive refraction into negative refraction; (f) clearly, TE polarization is not affected by the anisotropy of the material and does not exhibit any strong features at critical wavelength; the dip in reflection around 10 μm occurs because the real part of ε_{xy} is approaching 0 and the imaginary part is becoming increasingly large; printed with permission from our PU collaborators.

The interval of negative refraction may be observed by tracing Brewster's angle for each wavelength. Brewster's angles, corresponding to minimum reflectance of TM-polarized light, are marked as solid white curves in Fig. 2.6(d). The different spectra locations of the minima are due to the wavelength-dependent permittivity of the metamaterial. The apparent discontinuous step of the Brewster's angle tracing specifies the critical wavelength switching the optical properties of the metamaterial. Therefore, in experiments the discontinuity of Brewster's angles is utilized as the spectral indicator of the onset of negative refraction bandwidth. Figs. 2.6(d, f) show the color plots of the experimental TM and TE reflectance, respectively. The wavy fringes in spectra are due to multiple reflection effect across the epitaxial layer. Not surprisingly, TE reflectance does not exhibit Brewster's angles.

As mentioned above, the discontinuity of Brewster's angle is utilized to mark of beginning of the experimental negative refraction spectral region; moreover, we can also determine the end of the bandwidth λ_f by the large increase in the reflectance [Fig. 2.6(d)]. This instant increase at λ_f is due to both real parts of ε_{xy} and ε_z approaching 0, and their growing imaginary parts. The bandwidth (Δ) of the negative refraction is computed as the percentage deviation from the middle of the interval [6],

$$\Delta = \frac{\lambda_f - \lambda_c}{(\lambda_f + \lambda_c)/2} \tag{2.25}$$

For example, in this typical metamaterial, the negative refraction bandwidth is about 26.2% covering $\lambda_0 = 8.0 - 10.4\ \mu m$.

Furthermore, we compare the experimental measurements to our theoretical simulations [Fig. 2.7]. The simulations use the anisotropic transfer-matrix approach [116] [see details in Appendix A] to compute the electromagnetic fields in the planar semiconductor

heterostructure of air-metamaterial-InP-air. The discontinuity of minima occurs around the critical wavelength. An interesting observation is that the minimum dip of the experimental transmittance data at the critical angle stops at high incident angle; in contrast, the simulation shows continuity of the minimum at high angle. Possibly the stop of the minimum dip is the remark of nonlocality in the multilayered structures [59, 150, 151]. This behavior was seriously studied in the nanowire structures [152].

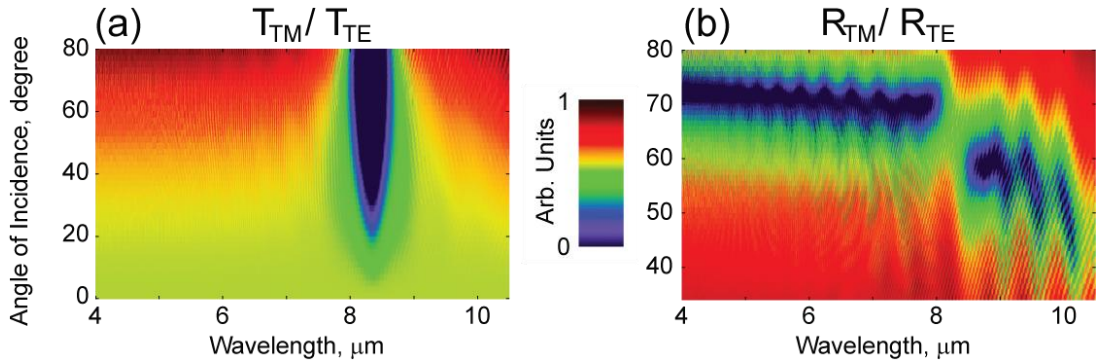

FIGURE 2.7: Calculations of the ratio of (a) TM and TE transmittance and (b) TM and TE reflectance; the results are in good agreement with experiments; however, position of critical wavelength is quite off due to the variation of the doping concentration in the experiments.

2.4 Broadband Negative Refraction and Flat Response

The effective dielectric constant tensor is a dispersive quantity. However, in imaging or optical cloaking applications [14, 16, 70, 76, 83, 153] the optical properties of metamaterials are required to remain unchanged for a range of wavelengths, and the bandwidth of negative refraction spectra should become significantly broadened.

In this Section, we design the graded-negative refraction metamaterials which have flatter dispersion and broader spectral response. Let us consider refraction of an electromagnetic wave with a wavelength and an incident angle from air to a metamaterial. The shift of the transmitted wave is directly related to the refracted angle, and depends on the dispersive dielectric constant tensor. Therefore, theoretically if we can design a structure which is capable of supporting constant shift in a range of spectrum, then as a result, we achieve a flat dispersive response and a broadband spectrum.

The general concept of the design is very similar to the chromatic aberration correction used in the conventional lens systems [116]. We need to add a set of multilayered metamaterial stacks with longer critical wavelength and thinner thicknesses to the main metamaterial stack, which is thickest and has highest doping constant. The negative refraction bandwidth of each metamaterial stack is overlapped with each other to support the broader bandwidth, and the thickness of each stack is tuned to flatten the negative electromagnetic wave shift.

Three samples are designed for the study: one, two, and four metamaterial substacks are labeled as sample A, B, and C, respectively. The designed structural parameters, including different critical wavelengths are given orderly in Table 2.2. Fig. 2.8(a) shows the real parts of individual dielectric functions of different substacks. It is clearly seen that the critical wavelength of each metamaterial stack increases along with the decrease of doping concentration. The ray-tracing simulations of all samples are shown in Fig. 2.8(b). Obviously, the shift responses of two-layer and four-layer structures are almost independent of wavelength in the range of $8.5 - 9.2$ and $8.5 - 10.3\ \mu m$, respectively. In addition, the bandwidths in the structures are also expanded.

TABLE 2.2: Summary of the sample parameters of the study; the alignment of substacks is shown in inset of Fig. 2.8(b); the doping concentration and substack thickness are tuned for samples B and C to broaden negative refraction bandwidth and flatten the optical properties; calculations are compared to the baseline sample, sample A.

Sample	Substack Thickness (μm)	$N_d(1\times10^{18}\ cm^{-3})$	$\lambda_c\ (\mu m)$
A	$L_1 = 12$	8.3	8.37
B	$L_1 = 9.6$	8.3	8.37
	$L_2 = 1.9$	7.5	8.80
C	$L_1 = 8.0$	8.3	8.37
	$L_2 = 2.1$	7.5	8.80
	$L_3 = 1.1$	6.8	9.25
	$L_4 = 1.0$	6.4	9.53

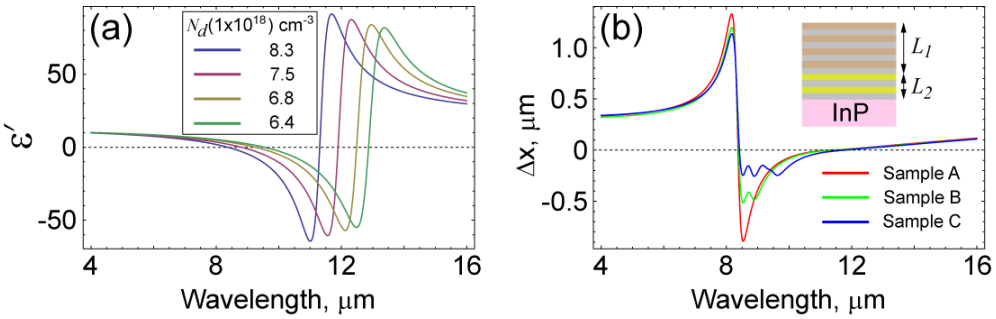

FIGURE 2.8: (a) Real part of ε_z for various doping concentration; the critical wavelength is increasing when the concentration is decreased, due to smaller free-carrier electrons; (b) the shifts (Δx) of the beam transmitting through each sample for 5° incident angle; sample C with four substack metamaterials has flatter and broader bandwidth; sample A, which is the baseline sample, has the most narrow bandwidth; the inset illustrates how the substacks are aligned.

We also perform the transmittance and reflectance calculations for sample B and C [Fig. 2.9]. In the transmittance plots, we see the overlapping of the absorption dips from different metamaterial stacks; the degrees of absorption reduce along to thickness of the corresponding doped substacks. In the reflectance plots, sample C is less dispersive than sample B.

Our PU collaborators verified experimentally the transmittance and reflectance of sample A-C [Fig. 2.10]. In the transmittance plots, we can see the overlapping of the minimum dips, mentioned above. In the reflectance plots, we see the broader spectral region of the negative refraction in sample C and B with bandwidth (Δ) of 33.2% and 32.0% respectively, while the bandwidth of the baseline sample is 26.2%. Therefore, the broadening of the bandwidth is improved by designing in advance the supplementary metamaterial substacks.

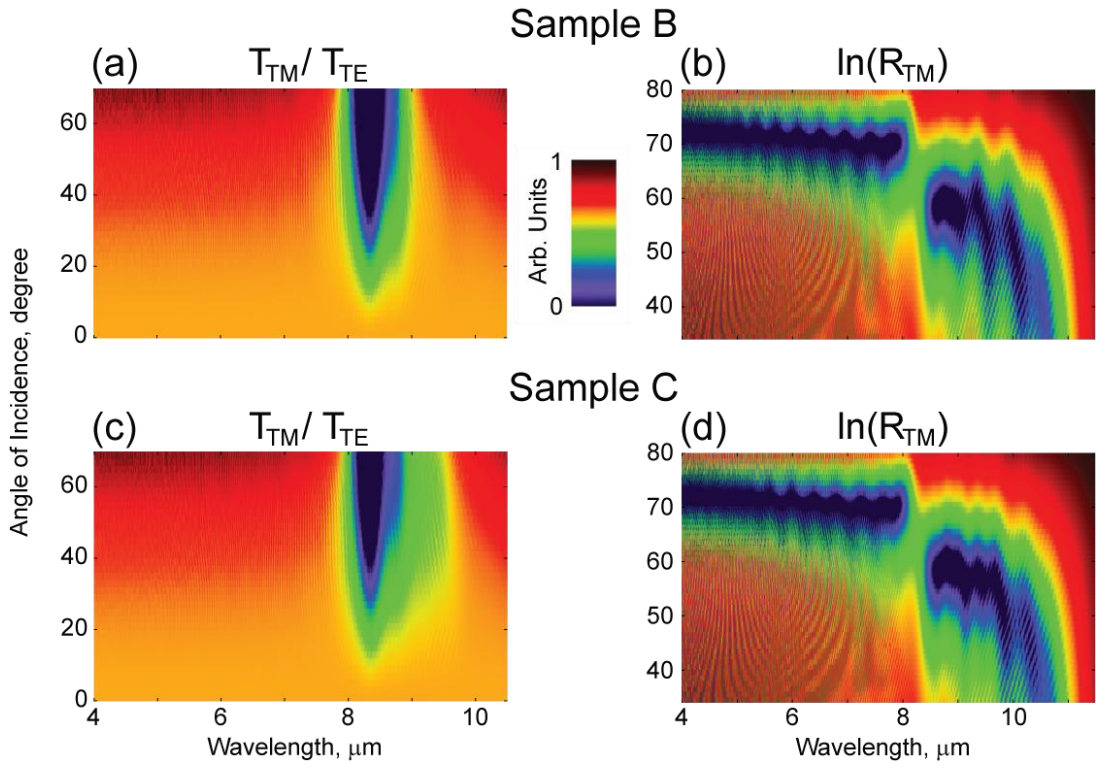

FIGURE 2.9: Theoretical transmittance and reflectance calculations with parameters given in Table 2.2; for sample B, (a) T_{TM}/T_{TE}, (b) $\ln R_{TM}$; for sample C, (c) T_{TM}/T_{TE}, (d) $\ln R_{TM}$; it is clearly seen broader negative refraction spectra in (d).

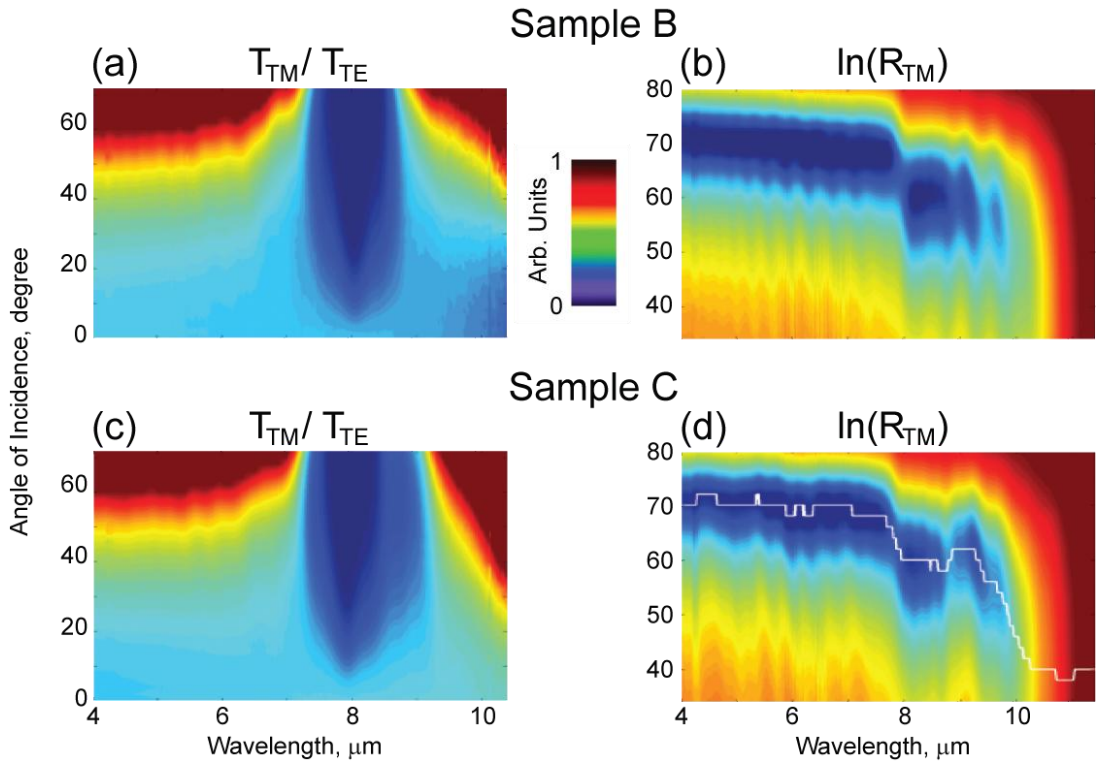

FIGURE 2.10: Experimental transmittance and reflectance measurements of samples B and C; (a, c) the overlapping of the absorption dips across differently highly doped substacks occurs in the flat dispersion portion of the negative refraction regime; (b, d) the broader negative refraction spectra are observed in the designed multiple-metamaterial substack composition with bandwidth of 32% and 33.2% for samples B and C; printed with permission from our PU collaborators.

The broader bandwidth can be further improved by adding more designed metamaterial substacks. However, as shown in Fig. 2.5(c), the loss is highest at the critical wavelength. Therefore, the overall loss inside the material in the flat dispersion portion of the negative refraction regime is increased.

2.5 Conclusion

To summarize, we first discussed the mathematical constitution of field propagation with backward-wavefront positive-refraction and forward-wavefront negative-refraction in

hyperbolic metamaterials. The physical understanding of image resolution inside isotropic and hyperbolic media was clarified. Later, the effective optical properties of nanolayered and nanowire structures were computed using the effective medium approximation; the dielectric constant tensor yielded hyperbolic dispersion relation, relating to the unusual field propagation behavior.

We showed theoretically and experimentally the negative refraction of waves transmitting through the InGaAs/AlInAs multilayered semiconductor metamaterials with different doping concentrations in mid-IR frequencies. The onset of negative refraction spectra occurring at the critical wavelength can be controlled by determining the doping density and layer thickness. Finally, we extended the spectral bandwidth of negative refraction and flatten the optical response by adding the substacks of predesigned metamaterials. The potential applications of such metamaterials include waveguiding, imaging, security and sensing, beam-steering, and nanolithography.

Chapter 3 - Hypergratings: Light Communication in Planar Hyperbolic Metamaterials

3.1 Introduction

Progress in sensing, imaging, and communication technology requires ever improving control over the propagation of electromagnetic waves [14, 19, 47-51, 61, 64-66, 70, 154-160]. A generic photonic unit (e.g. optical sensor, lithographic or imaging apparatus, communication unit) can be considered as a device providing the optical communication between several spatially separated spots ("object" and "image"). The separation between the spots ("focal distance") and the size of the spot ("resolution") are among the main figures of merit for optical systems.

In this Chapter, we propose a technique for *far-field communications* between several *subwavelength* spots based on manipulation of subwavelength signals in *planar slabs* of hyperbolic metamaterials [16]. Our method combines the benefits of planar optics offered by Fresnel zone plates [116] and negative-refraction lenses [19, 115], wide-spectrum-generation offered by near-field plates [156-159], and diffraction-less propagation offered by strongly anisotropic (hyperbolic) metamaterials. The method is illustrated on the example of far-field subwavelength foci generated by the diffraction plates in hyperbolic metamaterials. Analytical estimates of the performance of such "hyper"-gratings are provided and verified with numerical solutions of Maxwell's equations. Generalizations of the proposed technique for on-chip communications are suggested.

The optical behavior of imaging or focusing devices is most clearly seen by considering the wavevector space of a system. In this approach, an optical pulse at the

entrance of a device is represented as a set of plane waves with well-defined components of the wavevector $\vec{k}$ and frequency ω. The spatial evolution of each of these waves is then analyzed, and finally the spectrum is converted back into the real-space domain at the exit point of the device.

As mentioned in Section 2.2.3, most transparent natural materials support propagating waves with some limited range of transverse wavevectors. The maximum value of the transverse wavevector component $k_x^{max} = \sqrt{\varepsilon}\omega/c$ determines the minimum size of the focal spot that can be achieved in a device in the far-field limit $\backsim 2\pi/k_x^{max} = \lambda_0/\sqrt{\varepsilon}$ [116, 139]. The role of conventional optical elements is therefore reduced to adjusting the phase-shifts between different wavevector components to achieve the best-possible (although still diffraction-limited) resolution. This adjustment is typically provided by material inhomogeneities (lenses), or by diffraction gratings (Fresnel lenses or zone plates).

Several techniques have been suggested to achieve subwavelength imaging. Some of these techniques – near-field scanning optical microscope (NSOM) [161-163], superlens [19, 50], and near-field plates [156-159] – rely on exponentially decaying (evanescent) fields with $|k_x| > k_x^{max}$ to surpass the diffraction limit. Unfortunately, the realistic applications of these techniques are limited to near-field proximity of the imaging system [60]. Another class of structures, either uses transformation optics techniques (light compressors) [66, 70], or makes use of ultra-high-index modes in plasmonic [155] or strongly anisotropic [15, 42, 164] media. While these systems are able to achieve subwavelength light manipulation in the far-field, their fabrication requires three-dimensional patterning. Moreover, the devices themselves are often non-planar which further restricts the range of their possible applications [14, 61-64].

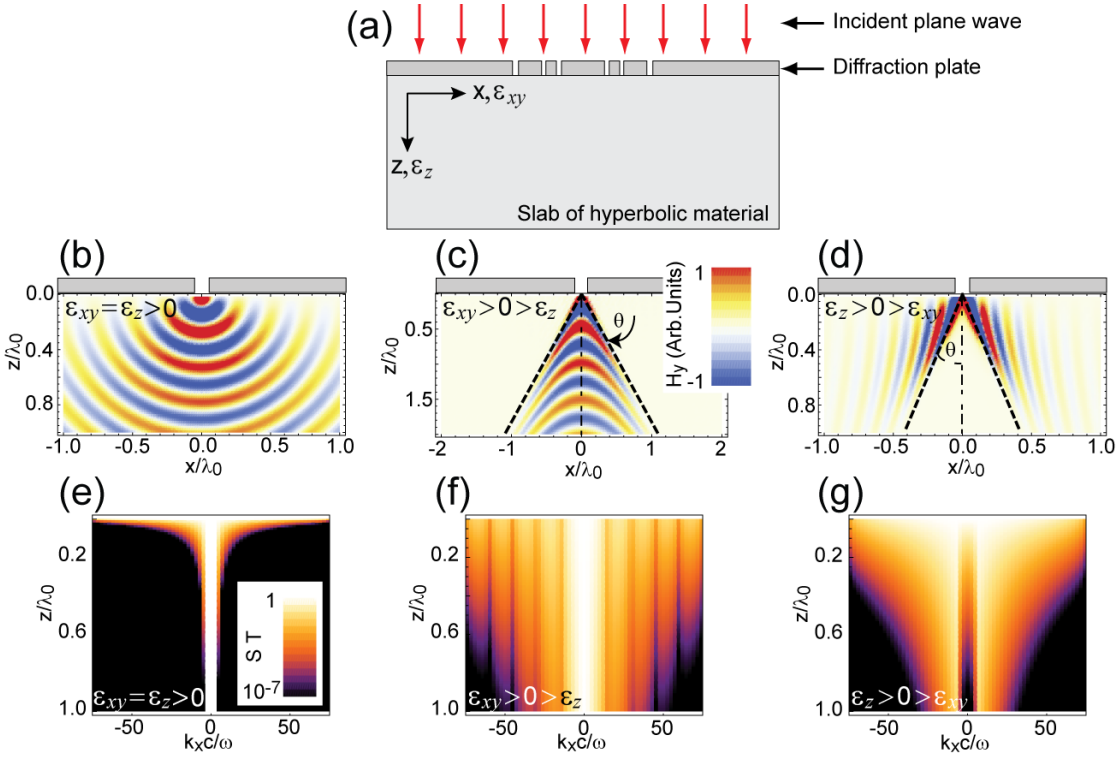

FIGURE 3.1: (a) Schematic of the hypergrating structure; 1D diffraction plate is shown; (b) diffraction-limited propagation in Si, $\lambda_0 = 15\ \mu m$, $d_1 = 200\ nm$, $x_1 = 0$, $\varepsilon_{xy} = \varepsilon_z = 16$; (c), (d) subdiffraction propagation in (c) negative refraction and (d) positive refraction metamaterials, (c) $d_1 = 100\ nm$ and (d) $d_1 = 200\ nm$; dashed lines show the direction of $|k_x c/\omega| \gg 1$ modes [Eq. (3.4)]; panels (e)-(g) show spectra of the systems in (b)-(d), respectively; reprinted with permission from Ref. [16].

Here we propose a system capable of far-field subwavelength light manipulation which is free of the above restrictions [16, 17]. The schematic of the proposed planar structure and several realizations are shown in Fig. 3.1. The system comprises a planar slab of the hyperbolic metamaterial covered with a subwavelength metallic diffraction plate. As will be explained below, the diffraction plate is responsible for generating the high-wavevector components of transmitted electromagnetic fields, and the slab is used for the routing of the resulting subwavelength signals.

This Chapter is organized as follows. In Section 2, propagation of diffracted fields from a single slit in hyperbolic metamaterials will be studied. Formalism of the subwavelength focusing structure will be developed in Section 3. Limitation of the technique is also discussed. In Section 4, we suggest that Fresnel zone plate hypergratings may behave as a converging lens and can be utilized for magnification and far-field imaging with subwavelength resolution.

3.2 Light Diffraction from a Single Slit

We begin by discussing the propagation of TM-polarized light generated by a thin slit of width $d_1 \ll \lambda_0$ with center positioned at $x = x_1$. We assume that the pulse propagates along the optical axis [axis z in Fig. 3.1(a)] of a uniaxial anisotropic metamaterial with the dielectric permittivity tensor $\hat{\varepsilon}$ [Eq. (2.5)]. The field due to the slit inside the metamaterial at the distance z from the interface is given by [138]

$$H_y(x,z) = \int_{-\infty}^{\infty} S(k_x)T(k_x,z)e^{ik_x x}dk_x \tag{3.1}$$

with the slit source $[S(k_x)]$ and the transfer $[T(k_x,z)]$ functions given by

$$S(k_x;x_1,d_1) = d_1\mathrm{sinc}(k_x d_1/2)e^{-ik_x x_1}\,, \tag{3.2}$$

$$T(k_x,z) = e^{ik_z z}\,, \tag{3.3}$$

where $k_z = \pm\sqrt{\varepsilon_{xy}\left(\frac{\omega^2}{c^2} - \frac{k_x^2}{\varepsilon_z}\right)}$ is given by the anisotropic dispersion relation [Eq. (2.8)], and the sign of the square root is chosen to enforce the field decay inside the absorptive medium.

The amplitude of the transfer function defines the evolution of the wavevector spectrum, and thus effectively defines the resolution of the system. As seen from Eq. (3.3), in

isotropic systems, the high-k_x components of the spectrum are exponentially suppressed [Fig. 2.1(c) and Fig. 3.1(b, e)], and the subwavelength solution is limited to the proximity of the slit.

The situation is dramatically different in strongly anisotropic metamaterials that have $\varepsilon_{xy}\varepsilon_z < 0$ where hyperbolic dispersion virtually eliminates high-k_x cut-off [42, 121, 132, 133]. Nanolayer [6, 120] and nanowire [44, 147, 165] realizations of these unique structures have been theoretically predicted and experimentally demonstrated for near-UV, visible, near- and mid-IR frequencies. It has been shown – both theoretically and experimentally – that optical properties of relatively thick metamaterials are well-described by effective medium theories [6, 41, 45, 120, 140, 143, 147]. Here we illustrate the subdiffractional manipulation of light for an Au-alumina nanowire system [41, 147] and InGaAs-AlInAs nanolayer [6, 120] structures operating at $1.5\,\mu m$ and $15\,\mu m$ respectively, where applicability of effective medium theories has been verified. The particular material parameters that we use in our simulations are: $\varepsilon_{xy} = 3.6 + 0.05i$; $\varepsilon_z = -12.2 + 1.36i$ for nanowire system and $\varepsilon_{xy} = -6.4 + 1.4i$; $\varepsilon_z = 36 + 3.4i$ for multilayered structure [149].

We emphasize again that the two structures have opposite anisotropy. The nanowire composite exhibits negative refraction (positive phase index) properties for incident light with $1.5\,\mu m$ wavelength as described in Chapter 2, and supports the propagation of both small ($|k_x c/\omega| \lesssim \sqrt{\varepsilon_0}$) and high-wavenumber waves. In contrast to this behavior, the nanolayer composite operates in the positive-refraction (negative phase index) regime for incident light with $15\,\mu m$ wavelength; the structure only supports high-wavenumber components. As seen in Fig. 3.1, both structures dramatically outperform their isotropic counterparts. However, suppression of diffraction-limited background in nanolayered structure makes these systems more suitable for far-field operations.

As described above, the subdiffraction manipulation of light relies on the propagation of high-k_x modes. In strongly anisotropic systems these waves propagate almost parallel to each other, where the angle between the propagation direction and the optical axis is given by the ratio of Poynting vector components [166, 167]:

$$\tan\theta = \frac{S_x}{S_z} \backsimeq \sqrt{-\frac{\varepsilon'_{xy}}{\varepsilon'_z}}. \tag{3.4}$$

The concentration of subwavelength components into the two subwavelength beams emerging from the point slits are clearly seen in Fig. 3.1(c, d); the directions of these beams are in perfect agreement with Eq. (3.4). Resonance cones exist only in the frequency regions where either ε_{xy} or ε_z becomes negative, but not both. For negative refraction, the diffracted fields propagate inside the cone yielding the hyperbolic wavefront pattern on the optical axis; in contrast, positive refraction metamaterials yield waves propagating outside the cone, and the hyperbolic wavefront pattern is perpendicular to the optical axis. Note that while the field distribution in nanowire metamaterials is dramatically different from that in nanolayer structures, the spectra of both systems contain substantial contributions of subdiffractional components [Fig. 2.1(d, e) and Fig. 3.1(f, g)].

3.3 Fresnel Zone Plate Hypergratings

The light propagation behind an arbitrary 1D diffraction plate with slits of thickness d_1, d_2,… positioned at x_1, x_2,… is given by Eqs. (3.1)-(3.3) with the multiple-slit source function $S(k_x) = \sum_i S(k_x; x_i, d_i)$. Thus, each slit of the diffraction grating generates a set of two subwavelength beams diverging at an angle θ. The interference of these beams can then be

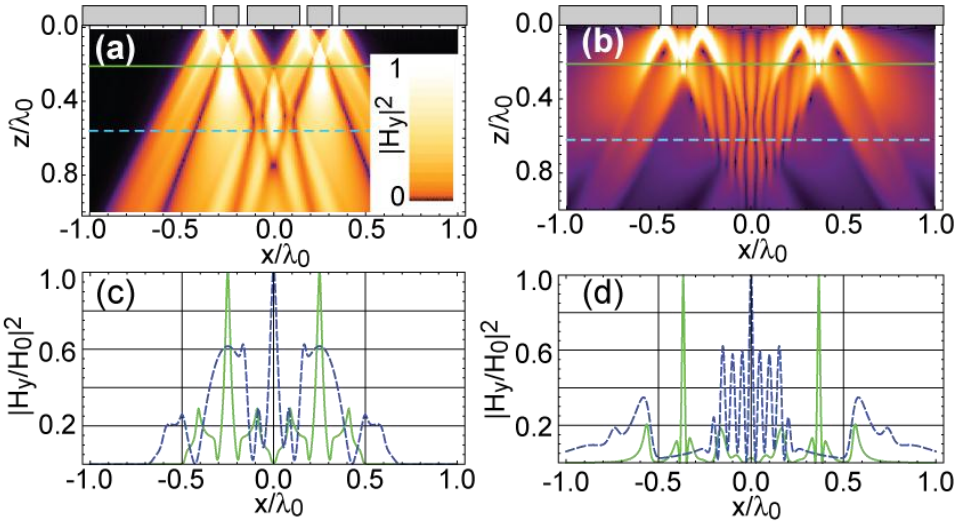

FIGURE 3.2: 1D hypergratings for subdiffractional photonics in the bulk of (a) nanowire and (b) nanolayer metamaterials; profile of several subwavelength foci from (a) and (b) is shown in (c) and (d), respectively; the fields in (c, d) are normalized to the maximum field at the given distance from the plate; dashed and solid lines in (a, b) correspond to the positions of field profiles shown in (c, d); geometry parameters: (a, c): slit thickness $d_1 = d_2 = d_3 = d_4 = 100\,nm$, slit positions $x_1 = -500\,nm$, $x_2 = -300\,nm$, $x_3 = 300\,nm$, $x_4 = 500\,nm$; (b, d): slit thickness $d_1 = d_2 = d_3 = d_4 = 200\,nm$, slit positions $x_1 = -7\,nm$, $x_2 = -4\,nm$, $x_3 = 4\,nm$, $x_4 = 7\,nm$; reprinted with permission from Ref. [16].

used to generate a subwavelength pattern inside the bulk of metamaterial or on its opposite edge.

The class of nanophotonic devices based on combinations of planar hyperbolic metamaterials and diffraction plates can be called *hypergratings* [16, 17], reflecting some analogy between these systems, Fresnel optics, and hyperlenses.

The developed framework is easily extendable for 2D diffraction plates, with each point of the plate generating a cone of radiation with apex angle 2θ [see Eq. (3.4)]. The superposition of these cones explains, in particular, the appearance of periodic subwavelength patterns in recent numerical simulations which image 2D arrays of holes by multilayered

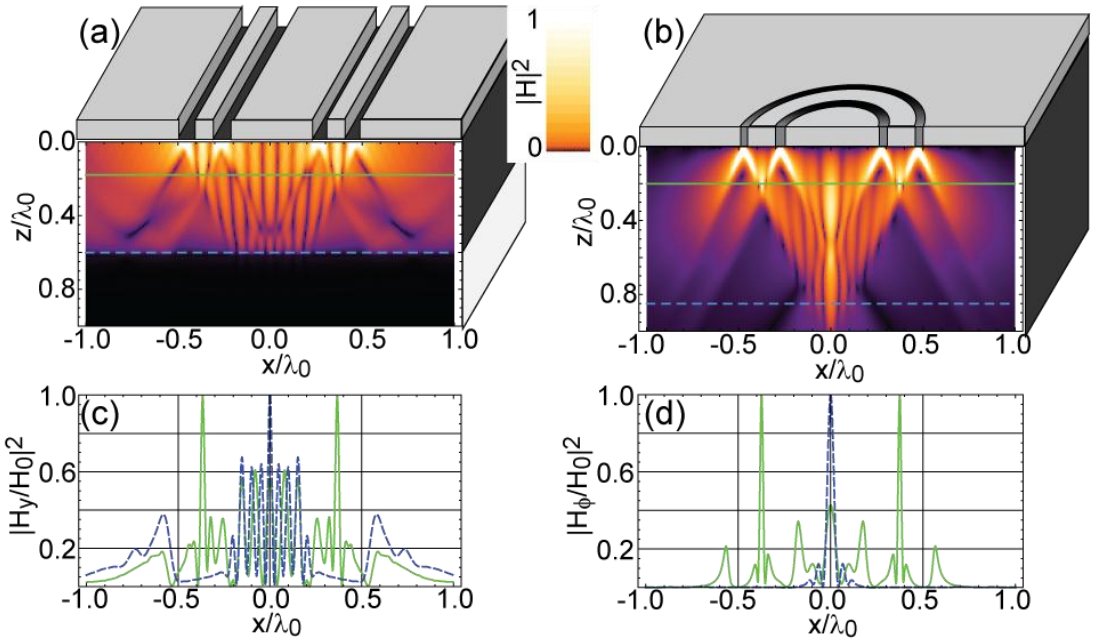

FIGURE 3.3: (a) Subdiffractional light focusing at the interface between a nanolayer composite and air and in the bulk of the structure; (b) light focusing inside 2D hypergrating; profiles of several subwavelength foci from (a) and (b) are shown in (c) and (d), respectively; the fields in (c, d) are normalized to the maximum field at the given distance from the grating; dashed and solid lines in (a, b) correspond the positions of field profiles shown in (c, d); geometry parameters: (a, c): slit thickness $d_1 = d_2 = d_3 = d_4 = 200\,nm$, slit positions $x_1 = -7\,nm$, $x_2 = -4\,nm$, $x_3 = 4\,nm$, $x_4 = 7\,nm$; (b, d): $d_1 = d_2 = 200\,nm$, $r_1 = 4\,\mu m$, $r_2 = 7\,\mu m$; reprinted with permission from Ref. [16].

composites [160]. The limit $|\varepsilon_z| \gg |\varepsilon_{xy}|$ yields $\theta \to 0$ and corresponds to canalization regime observed in low-frequency nanowire structures [168, 169].

Hypergratings have potential to enable numerous exciting applications, including the communication between diffraction-limited optics and subwavelength length scales, communication between several subwavelength objects inside a system, high-resolution lithography, high-density data storage, and high-density sensing. In particular, hypergratings can be designed to realize the planar Fresnel-like lenses with subwavelength foci, potentially enabling unprecedented density of pixels at the focal plane.

Several examples of generation of subwavelength field patterns inside and at the back edge of the metamaterial are shown in Figs. 3.2 and 3.3. Note that the size of the hypergrating foci ranges from $\lambda_0/50$ to $\lambda_0/20$ and is almost unaffected by the presence of material interfaces.

Such Fresnel hypergratings can be designed for any value of focal distance f by blocking (or reversing phases) of even (or odd) Fresnel zones. The wavelength-dependent coordinates x_m of boundaries of Fresnel zones [see Appendix B] in hyperbolic media are expressed by

$$\sqrt{\varepsilon'_{xy} f^2 + \varepsilon'_z x_m^2} - \sqrt{\varepsilon'_{xy} f^2 + \varepsilon'_z x_0^2} = \pm \frac{m\pi c}{\omega} \tag{3.5}$$

where x_0 is the horizontal displacement of the first opened Fresnel zone from the optical axis; for materials with $\varepsilon'_{xy} > 0$, $x_0 \geq 0$ and for materials with $\varepsilon'_{xy} < 0$, $x_0 \geq f \tan\theta$. The sign in Eq. (3.5) corresponds to the sign of ε'_z. Note that Fresnel lens with $\varepsilon'_z < 0 < \varepsilon'_{xy}$ is "left-handed": for oblique incidence, its focal point stays on the same side of the normal as the incident beam [see Section 3.4]. Moreover, the Fresnel lens hypergratings supports a number of secondary foci along the optical axis in addition to its main focal spot [Fig. 3.4(a)], as well as those usually found in the conventional Fresnel zone plate.

We now turn to the analysis of limitations of the proposed technique. The main limitation of the resolution of anisotropy-based nanophotonics comes from material absorption. In the limit of low loss, the high-k_x behavior of the transfer function can be characterized by

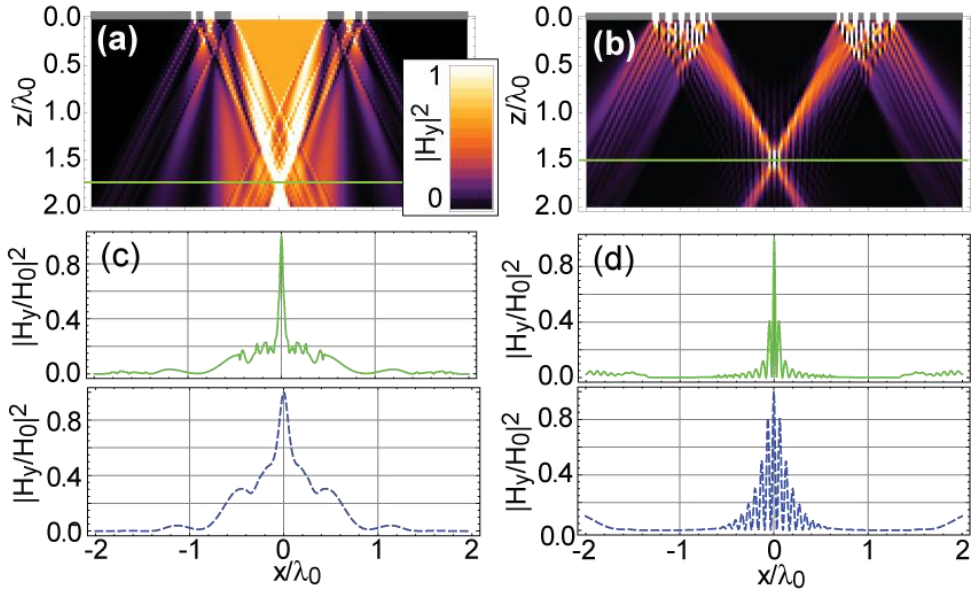

FIGURE 3.4: Effect of losses on far-field resolution of Fresnel zone plate hypergratings; sizes and positions of the slits are given by Eq. (3.5); panels (a, b) show field distribution in low-loss (a) nanowire and (b) nanolayer structures (ε'' is reduced 10 times with respect to bulk values shown in Section 3.2); panels (c, d) show field profiles in the focal planes; solid lines correspond to field distribution in low-loss systems, dashed lines represent performance of structures with full loss; reprinted with permission from Ref. [16].

$$|T(k_x, z)| \simeq \exp\left[-\frac{z}{2}\sqrt{-\frac{\varepsilon'_{xy}}{\varepsilon'_z}}\left(\frac{\varepsilon''_{xy}}{|\varepsilon'_{xy}|}+\frac{\varepsilon''_z}{|\varepsilon'_z|}\right)k_x\right]. \tag{3.6}$$

The evolution of the spectrum of the wavepackets inside anisotropic metamaterials calculated using numerical solutions of Maxwell's equations are shown in Fig. 3.1(f, g). Note that the performance of realistic metamaterials greatly exceeds the performance of their isotropic counterparts [Fig. 3.1(e)].

Assuming that the wavevector spectrum at the focal spot is dominated by the high-wavevector components given by Eq. (3.6), and neglecting the specific dynamics of $|k_x| \lesssim$

ω/c waves, we arrive at the following estimate of the resolution in the anisotropy-based hypergratings:

$$\Delta \backsim z\sqrt{-\frac{\varepsilon'_{xy}}{\varepsilon'_z}}\left(\frac{\varepsilon''_{xy}}{|\varepsilon'_{xy}|}+\frac{\varepsilon''_z}{|\varepsilon'_z|}\right). \tag{3.7}$$

Thus, material absorption serves as a major limitation to far-field subdiffractional focusing. However, since hypergratings are nonresonant and thus do not require restoration of evanescent waves, it is possible to achieve resolution $\sim \lambda_0/10$ at a distance $\sim 1.5\,\lambda_0$. Note that the resolution of hypergratings is directly proportional to the losses, $\Delta \propto \varepsilon''$ (in contrast to $\propto -1/\ln(\varepsilon'')$ dependence of superlenses [60]). Reducing the losses (for example by incorporating the gain into the system [170-175] or engineering larger interatomic distances in metallic conclusions [176]) restores the resolution [Fig. 3.4]. Our analysis indicates that under realistic conditions, Eq. (3.7) tends to overestimate the FWHM of the image.

The second limitation of the proposed technique emanates from the appearance of nonlocal corrections in the $k_x \gg \omega/c$ response of composite systems. Extensive previous research [147, 150, 177] indicates that these corrections become important when the scale of field variation in the system becomes comparable with the size of its structural unit. Thus, the nonlocal corrections will limit the resolution of hypergratings systems to the scale of the metamaterial component ($\leq 10-50\ nm$ in realistic nanowire and nanolayer structures).

3.4 Hypergrating as a Magnifying Lens

It has been known that a conventional Fresnel zone plate can behave as a thin lens [116]. In this Section, we show that, similar to the typical converging thin lens, the Fresnel zone plate hypergratings with negative-refraction metamaterials are capable of performing spatial

Fourier-optics, transforming an incident plane wave into the point on the focal plane with the position of the focal point depending on the angle of incidence of the original plane wave [17]. In the paraxial limit, magnifying objects by hypergratings is possible.

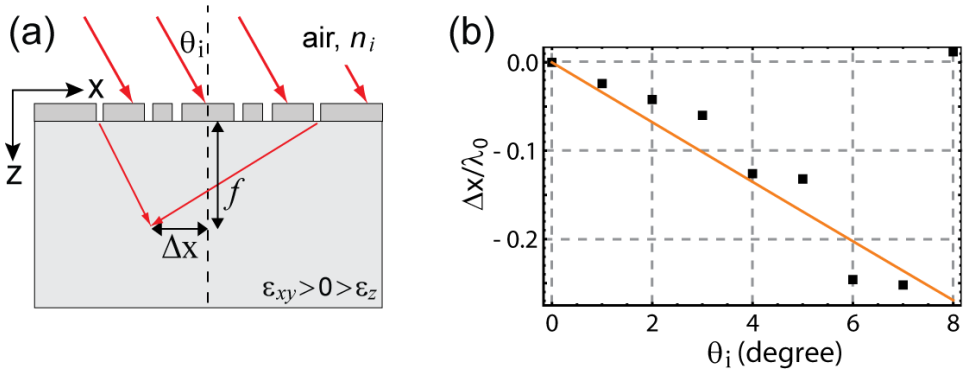

FIGURE 3.5: (a) Schematic of focal spot shifted by incident fields with small angles of incidence; for negative refraction materials, focal spots stay on the same side as the incident waves; (b) positions of focal points on the focal plane when θ_i is varied; around 8 degree, focal spot is destroyed; squared dots show maximum field intensity of simulations and orange line corresponds to Eq. (2.11).

As mentioned above, a Fresnel lens with $\varepsilon_z' < 0 < \varepsilon_{xy}'$ is "left-handed": when a plane wave is incident on a hypergrating with a small angle of incidence, the focal point shifts from the normal spot toward the same side as the incident beam [Fig. 3.5(a)]. The shift (Δx) of the focal plane agrees well with Snell's law [Eq. (2.11)] where $\tan\theta_g = \Delta x/f$. In Fig. 3.5(b), we numerically measure the position of maximum field intensity on the focal plane for small angles of incidence. The particular parameters used in the simulations are $\varepsilon_{xy} = 12.2$, $\varepsilon_z = -3.6$, $\lambda_0 = 3\,\mu m$, and $f = 6\,\mu m$. The deviation of the measured focal spots from the predicted positions may come from coarse step size used in the simulations. However, the focal spot is destroyed for angles larger than $\theta_i \backsimeq 8°$. Note that the shift of a focal spot with

small angle of incidence is a property of a conventional lens. We emphasize again that the Fresnel zone plate hypergratings are highly capable of transmitting signals to deep subwavelength detectors placed on many locations at the focal plane.

So far we have considered hypergratings with plane wave incidence. However, as well as conventional Fresnel lens, the hypergratings can magnify objects (sources) when the paraxial limit is taken into account. Fig. 3.6 shows theoretically the imaging schematic. With $\varphi_m - \varphi_0 = -m\pi$ and formalism developed in Appendix B, we arrive at

$$s_i\left(\sqrt{1+\frac{x_m^2}{s_i^2}}-1\right)+\sqrt{\varepsilon'_{xy}}s_o\left(\sqrt{1+\frac{\varepsilon'_z}{\varepsilon'_{xy}}\frac{x_m^2}{s_o^2}}-1\right)=-\frac{m\pi c}{\omega} \tag{3.8}$$

where s_i and s_o are image and object distances, respectively. Eq. (3.8) represents coordinates of boundary of m-th Fresnel zone, related to s_i, s_o, and optical parameters. When $s_i \to \infty$ (plane wave incidence), Eq. (3.8) reduces to Eq. (3.5). In the paraxial limit in which $\sqrt{-\varepsilon'_{xy}/\varepsilon_z}s_o \gg x_m$ and $s_i \gg x_m$, we obtain a hypergrating thin-lens equation:

$$\frac{1}{s_i}+\frac{\varepsilon'_z}{\sqrt{\varepsilon'_{xy}}s_o}=-\frac{m\lambda_0}{x_m^2} \tag{3.9}$$

with

$$m_{max}=\frac{\varepsilon'_{xy}}{\varepsilon'_z}\frac{s_o^2}{\lambda_0}\left[\frac{\varepsilon'_z}{\sqrt{\varepsilon'_{xy}}s_o}+\frac{1}{s_i}\right] \tag{3.10}$$

(maximum zone number is discussed in Appendix B). Such a structure behaves as a converging lens on a slab of negative-refraction metamaterial [Fig. 3.6] where the object and

image focal distances are $f_o = -\varepsilon_z'/\sqrt{\varepsilon_{xy}'}\,[x_m^2/(m\lambda_0)]$ and $f_i = -x_m^2/(m\lambda_0)$, respectively. Note that in this imaging structure, a ray tracing approach is employed in the paraxial limit of hypergratings. The locations of the object and focal spots, and the image and object positions are shown in Table 3.1. The transverse magnification of the hypergrating lens is given by

$$M_T = -\frac{\varepsilon_z'}{\sqrt{\varepsilon_{xy}'}}\frac{s_i}{s_o}. \tag{3.11}$$

In contrast to negative-refraction metamaterials, hypergratings with a slab of $\varepsilon_{xy}' < 0 < \varepsilon_z'$, materials may not behave as a thin lens since the paraxial limit cannot be satisfied ($x_m > s_o\sqrt{-\varepsilon_{xy}'/\varepsilon_z'}$). Physically, electromagnetic fields coming out from an object inside the metamaterial slab propagate outside the resonance cones; hence, in air the diffracted fields will diverge and prevent the formation of the image.

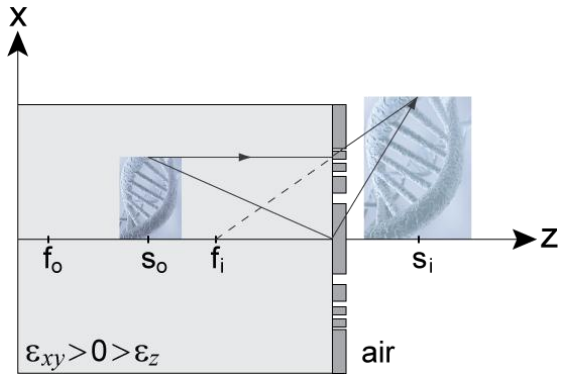

FIGURE 3.6: Imaging mechanism of thin-lens hypergratings; when subwavelength object is placed at $s_o < f_o$ (in negative refraction metamaterials or in reality, behind hypergratings with thickness s_o), real magnified image occurs at s_i (in air) with erect orientation; ray tracing technique is employed in this analysis.

TABLE 3.1: Object and image properties in Fresnel lens hypergratings.

Object	Image			
Location	Type	Location	Orientation	Relative Size
$s_o < f_o$	real	in air	erect	magnified
$s_o = f_o$	∞			
$s_o > f_o$	virtual	in metamaterial	inverted	minified

3.5 Conclusion

We have proposed a new class of planar nanophotonic systems, hypergratings, which combine the benefits of planar zone plates with the far-field subwavelength resolution of the hyperlens. Subwavelength focal spots in the far-field of the hypergratings were demonstrated numerically and the analytical description of the underlying physics was derived analytically. Examples of 1D and 2D amplitude gratings were presented. It is reasonable to assume that the results can be further optimized with phase gratings. We also showed that hypergratings can be utilized for magnification and far-field imaging with subwavelength resolution. The technique, illustrated here on examples of near-IR and mid-IR frequencies, is scalable from near-UV to mid-IR. Furthermore, the approach can be easily extended to enable the communication between subwavelength spots inside the bulk of metamaterials. Applications of the developed formalism lie in high-resolution sensing, nanolithography, high-density data storage, and on-chip communications.

Chapter 4 - Subwavelength Far-Field Imaging Technique

4.1 Introduction

High-resolution imaging is of interest for a broad class of applications spanning all parts of the electromagnetic spectra. Some applications of subwavelength imaging in information technology and life science include real-time biomolecule imaging, nanolithography, high-capacity optical data storage systems, and compact integrated optical telecom solutions [178-184]. Electromagnetic metamaterials and plasmonic systems promise to conquer the diffraction limit and offer numerous solutions to the problem of subwavelength imaging [14-19, 155]. However, while subwavelength light management in metamaterial systems may be free from the diffraction limit, the finite wavelength of light in air provides substantial challenges in experimental studies of nanophotonics.

Although near-field scanning optical microscopy (NSOM) [161-163] provides a way to analyze subwavelength field distributions, this technique suffers from a nontrivial convolution of the field pattern with the tip function. It is also implicitly slow and does not support real-time imaging since the evanescent signal is collected on a point-by-point basis. Moreover, NSOM is limited to visible and GHz parts of the spectrum and is not available at mid- and far-IR and THz frequencies. Another technique, called stimulated-emission-depletion microscopy (STED) [185-187] utilizes a light spot to excite fluorescence in subwavelength areas of samples. However, the technique forms images using the scanning scheme, and also needs fluorescent dyes and high illumination intensities to achieve a nonlinear response. Structured illumination microscopy (SIM) [188-192] was shown to improve the resolution of conventional optics by a factor of two by analyzing the light transmitted through a wavelength-scale diffraction grating, under a set of different

illumination conditions. More recently, an approach called far-field superlens (FSL) [193-196] was proposed to conquer the resolution limit. The technique utilizes a plasmonic thin film as superlens [19, 23] to enhance evanescent fields and then uses a first-diffraction-order metallic subwavelength grating to convert these evanescent fields into propagating waves which are detectable in far field. FSL can achieve $\sim\lambda_0/5$ resolution.

In Chapter 3, we developed the hypergratings structure which can focus incident plane waves into $\sim\lambda_0/50-\lambda_0/20$ resolution spot sizes. However, so far in our best knowledge, there has been no imaging technique that can achieve this high resolution by using far-field measurements. Here we present an approach that can be used to image unknown 1D objects with far-field measurements [197].

It has been known that the spectrum of the subwavelength object is dominated by high-wavenumber components that exponentially decay away from the object. Measurement of these evanescent components is impossible in the far-field regime. However, a subwavelength grating, located at the object plane, can potentially help the image-reconstructing procedure by converting the evanescent waves into propagating waves. Therefore, our technique, similar to FSL, relies on designing the plasmonic subwavelength grating to convert the information of subwavelength features into propagating waves. In contrast to FSL, our technique does not rely on resonant enhancement of subwavelength information with plasmonic structures, and we take advantage of many diffraction orders of the grating to obtain higher resolution. The approach promises broadband spectral response and direct imaging of high-resolution objects.

The rest of this Chapter is organized as follows. In Section 2, we will mention the concepts of the diffraction grating related to the grating equation and optical transfer function;

those will be necessary for our image-reconstruction technique. We will develop the imaging formalism in Section 3. In Section 4, we will illustrate the robustness of the developed technique by reconstructing the images of several single-slit sources, double slit-slit sources, and the size and shape of a subwavelength focal spot inside a hypergrating system.

4.2 Diffraction Grating

A diffraction grating, formed by a periodic set of slits, is an optical component that transforms the incident electromagnetic plane wave into a set of diffracted plane waves, called diffraction modes. The direction of propagation of each mode depends on angle of the incident plane wave, operating wavelength, permittivities of media, period of diffraction grating, and mode number. Grating applications include monochromators, spectrometers, and even imaging apparatus [186-191].

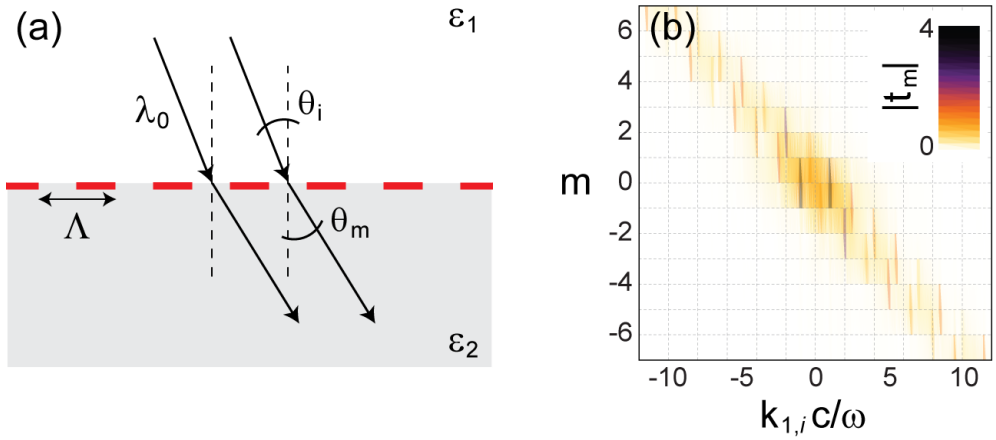

FIGURE 4.1: (a) Schematic of light diffraction; plane wave of operating wavelength λ_0 in isotropic medium ε_1 with incident angle θ_i is incident on a grating with period Λ; only one-diffraction-mode transmitted wave in isotropic medium ε_2 is shown; (b) absolute value of optical transfer function $|t_m|$ for several diffraction modes m and incident wavevector $k_{1,i}$.

Consider the incidence of an electromagnetic wave, either propagating or evanescent, on a diffraction grating with parameters: permittivity ε_g, periodic Λ, thickness h, and ridge filling factor f [Fig. 4.1(a)]. The grating is surrounded by two isotropic media with permittivities ε_1 (on input side) and ε_2 (on output side), respectively. The diffracted fields occupy many diffraction orders m, and a diffracted transverse-component wavevector for each order is given by the *grating equation* [116, 198]:

$$k_{2,m} = k_{1,i} + mk_\Lambda \tag{4.1}$$

where $k_\Lambda = 2\pi/\Lambda$ is the grating wavevector, $k_{1,i}$ is the transverse-component wavevector of the incident field, and $k_{2,m}$ is the transverse-component wavevector diffracted by an m-th order. It is clearly seen that the transverse wavevector component for each diffraction mode is translated by the amount of mk_Λ.

When the wavevector of the incident field is in the evanescent spectra ($k_{1,i} > |\sqrt{\varepsilon_1}2\pi/\lambda_0|$), with proper design of a subwavelength grating the diffracted wavevector may be shifted into the propagating regime ($|k_{2,m}| \leq \sqrt{\varepsilon_2}2\pi/\lambda_0$) which is detectable in the far field. Our imaging technique that uses a subwavelength grating to convert evanescent into propagating fields will be mentioned in details in Section 4.3.

In contrast, when the wavevector of the incident field is in the propagating regime; that is, a plane wave operated at wavelength λ_0 is incident with an angle θ_i, the diffracted fields can occupy both propagating and evanescent regimes. In this case, the grating equation is reduced to

$$\Lambda\left(\sqrt{\varepsilon_2}\sin\theta_m - \sqrt{\varepsilon_1}\sin\theta_i\right) = m\lambda_0\,, \tag{4.2}$$

giving θ_m, the diffracted angle for each diffraction order m. For normal incidence and $\varepsilon_1 = \varepsilon_2 = 1$, $\sin\theta_m = m\lambda_0/\Lambda$.

As mentioned earlier, our image-retrieval technique employs a subwavelength diffraction grating to convert the evanescent spectrum into propagating waves. Hence, it is important to know the contribution of each wavevector – both propagating and evanescent – to the diffracted fields. The quantity describing this contribution, called optical transfer function [OTF; $t_m(k_{1,i})$], is defined as the ratio of transmitted amplitude of the m-th mode $\left[a(k_{2,m})\right]$ over incident amplitude $\left[a(k_{1,i})\right]$, for various incident wavevectors [$k_{1,i}$]:

$$t_m(k_{1,i}) = \frac{a(k_{2,m})}{a(k_{1,i})}. \tag{4.3}$$

Rigorous coupled-wave analysis (RCWA) [199-202] is one of the most efficient techniques employed to compute reflecting and transmitting field amplitudes for each diffraction order. The technique expands the periodic relative permittivity in the grating region into the form of a Fourier series, writes electromagnetic fields in input and output regions of the diffraction grating as a linear combination of many diffraction modes, and then finds solutions that satisfy Maxwell's equations in all regions by solving the exact electromagnetic-boundary-value problem.

Fig. 4.1(b) shows the absolute value of OTF, $\left|t_m(k_{1,i})\right|$ as a function of $m \in [-7, 7]$ and $k_{1,i}c/\omega \in [-12,12]$ for a diffraction grating surrounded by air with parameters $\varepsilon_g = -100$, $f = 0.5$, $\Lambda = 2\lambda_0/3$, and $h = \lambda_0/10$, and the operating wavelength of $\lambda_0 = 1\ \mu m$.

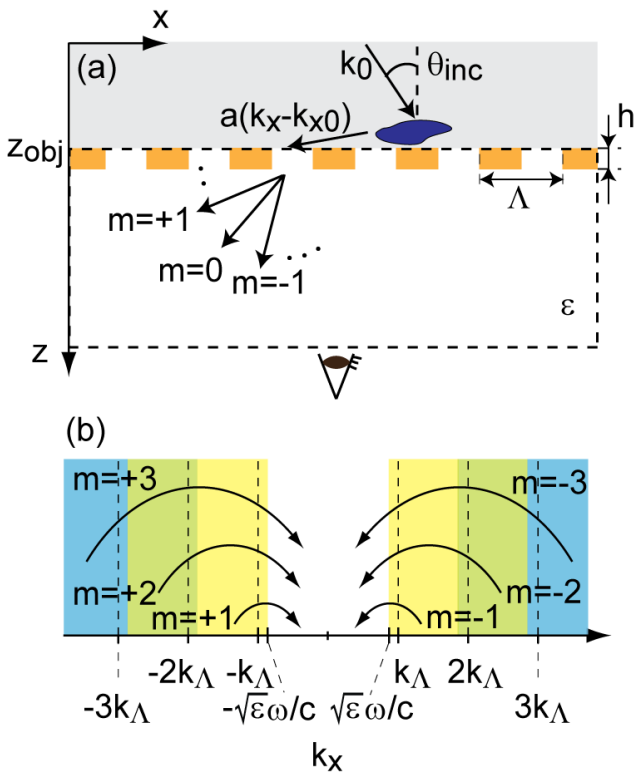

FIGURE 4.2: (a) Schematic of imaging structure; an object is placed closed to the subwavelength plasmonic grating with period Λ (at $z \cong z_{obj}$) and is irradiated by the plane wave with incident angle θ_{inc}; the far-field intensity is measured inside an isotropic material with permittivity ε; (b) transfer of evanescent information into propagating regime by the m-th diffraction order of the grating; normal incidence is assumed.

4.3 Imaging-Reconstruction Formalism

In this Section, we will develop the formalism of image reconstruction as follows. A subwavelength diffraction grating is placed at the object plane where the object is surrounded by a dielectric medium or hyperbolic metamaterial [Fig. 4.2(a)]. Light with transverse-component wavevector k_{x0} and angle of incidence θ_{inc} illuminates the object. Consequently, scattering fields with a broad range of wavevectors k_x, covering both propagating and

evanescent regimes, are diffracted by the grating. Each wavevector of the diffracted wave q_m can be related to the wavevector of the scattering field k_x by [Eq. (4.1)]

$$q_m = (k_x - k_{x0}) + mk_\Lambda \,. \tag{4.4}$$

Therefore, the subwavelength grating shifts some portions of the original propagating spectra into the evanescent regime, and shifts some portions of the evanescent spectra into the propagating regime [Fig. 4.2(b)], and then the originally-evanescent components can be detected with far-field measurements.

This procedure, however, leads to overlapping of the original evanescent signals with original propagating waves; so that extra measurements are required to deconvolute the different parts of the spectra from the far-field measurements. The approach to distinguish the propagating and evanescent spectra is detailed below. For simplicity, here we consider only TM-polarized incident waves. However, the formalism developed is directly applicable for TE-polarized light.

In Fourier space, an object comprises Fourier amplitudes with all ranges of wavevectors, $k_x \in (-\infty, +\infty)$. However, only a part of the spectra is substantially important, and then we might omit the other insignificant parts. Therefore, the electromagnetic field of the object can be represented as [138]

$$H_y^{obj}(x, z_{obj}) = \int_{-k_{x,max}}^{k_{x,max}} dk_x a(k_x) e^{ik_x x} e^{ik_z(k_x) z_{obj}} \tag{4.5}$$

where z_{obj} is the position on z-axis where the object is originally placed, $k_{x,max}$ is cut-off wavevector spectrum, k_z is related to k_x through the dispersion relation [Eqs. (2.7)-(2.8)], and $a(k_x)$ is the unknown complex amplitudes of the Fourier-decomposition of the light scattered

by the object. Hence, numerically the problem of imaging can be reduced to the problem of finding $a(k_x)$. When a subwavelength grating is placed at the object plane, each k_x component will be diffracted according to Eq. (4.4). Consequently, it is straightforward to show that the far-field TM-polarized light measured in a dielectric medium can be described numerically as

$$H_y^{far}(x, z, \theta_{inc}) = \sum_m \sum_n w_n a\left(k_{x,n} - k_{x0}\right) t_m\left(k_{x,n} - k_{x0}\right) e^{iq_{mn}x} e^{ik_z(q_{mn})z} \tag{4.6}$$

where $k_z(q_{mn}) = \sqrt{\varepsilon\, \omega^2/c^2 - q_{mn}^2}$, ε is permittivity of the isotropic medium in which the field is measured, and $t_m\left(k_{x,n} - k_{x0}\right)$ is OTF [Eq. (4.3)]. It is clearly seen that $a(\alpha_{mn}) = a\left(k_{x,n} - k_{x0}\right) t_m\left(k_{x,n} - k_{x0}\right)$. The index m corresponds to the summation over different diffraction orders, while the index n represents numerical integration over k_x with weighting factors w_n [203] [Fig. 4.2(b)].

When high-wavevector regimes are shifted into the propagating spectrum by the diffraction modes, the far-field propagating regime includes the overlapping of original propagating (clearly, by the $m = 0$ diffraction order) and original evanescent ($m \neq 0$ modes) components. We now come to the question how to deconvolute the different parts of the spectra from the far-field measurements. Both SIM and FSL rely on rotation of polarization of incident light to attain additional measurement and perform the deconvolution above. This procedure, however, is not desirable for systems where the properties of the sample strongly depend on polarization. Here we propose to fix the polarization of incident light, and instead rotate the direction of incident light (given by the angle of incidence θ_{inc}) as shown in Fig. 4.2(a).

This idea can be illustrated by the following simple example: let us consider a subwavelength single slit, surrounded by air and illuminated by a plane wave with incident angle θ_{inc}. Spectra of diffracted fields at two different distances behind the slit are shown in Fig. 4.3. It is obvious that in the evanescent regimes ($|k_x c/\omega| > 1$), the spectra of different incident angles are distinguishable in the near field, but indistinguishable in the far field. In contrast, the spectra of different incident angles in the propagating regime ($|k_x c/\omega| \leq 1$) are separated explicitly even in the far field. Hence, we may utilize this approach to split the overlapping spectra.

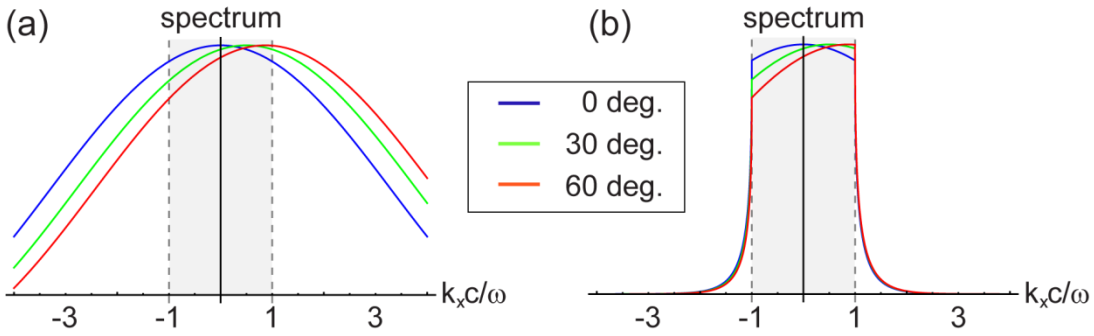

FIGURE 4.3: Field spectra of diffracted waves from a single slit with (a) near and (b) far distances; colored curves represent spectra of different angles of incidence (see inset); gray areas ($|k_x c/\omega| \leq 1$) correspond to propagating regions.

In this work, we numerically measure the field intensity at different transmitting angles θ_{tran} on a semicircle. Let this data be represented by P intensity (I_p) data points, $\{\theta_{inc,p}, x_p, z_p, I_p\}$. As an example, here we emulate the real experiment by sampling the numerical solutions of Maxwell's equations, obtained from commercial finite-element (FEM) [204] simulations. A nonlinear least-squares fitting technique based on Gauss-Newton algorithm [205] is used to

find the transmission coefficients. The method finds the unknown complex coefficients by minimizing the intensity deviation, represented by the sum (F) of squared residuals,

$$F = \sum_{p=1}^{P} \left[I_p - I\left(x_p, z_p, \theta_{inc,p}\right) \right]^2 \tag{4.7}$$

where $I\left(x_p, z_p, \theta_{inc,p}\right) = \left| H_y^{far}\left(x_p, z_p, \theta_{inc,p}\right) \right|^2$. Assuming $k_{x,n}$ is smaller than the cutoff wavevector $k_{x,max}$, the unknown complex transmission coefficients may be represented as a polynomial

$$a(k) = a_0 + a_1 \left(\frac{k}{k_{x,max}} \right)^1 + \cdots + a_j \left(\frac{k}{k_{x,max}} \right)^j + \cdots . \tag{4.8}$$

The minimum occurs when $\forall\, \partial F / \partial a_j = 0$. Finally, when the spectrum of the source is determined, the object is recovered using Eq. (4.5).

We emphasize that the most important aspects of our imaging-retrieval technique is to (i) use a subwavelength diffraction grating to allow measurements of subwavelength information in the far field, and (ii) vary angles of incidence to deconvolute the overlapping signals. In this work, we use the least-squares fitting technique to compute the unknown coefficient function; however, the technique could be vastly improved by employing more efficient mathematical algorithms to obtain the object's unknown Fourier function.

4.4 Far-Field Imaging with Typical Objects

The developed formalism is first illustrated on the examples of imaging several single-slit sources with widths $a = \lambda_0/2$, $\lambda_0/4$, $\lambda_0/8$, and $\lambda_0/20$ and double slit-slit sources with two $\lambda_0/4$ slits separated by $\lambda_0/5$, all placed in air. We assume that all linear dimensions are

normalized to the wavelength in the air λ_0, and use the following parameters for plasmonic grating: $\varepsilon_g = -100$, $h = \lambda_0/10$, $f = 0.5$, and $\Lambda = 2\lambda_0/3$. RCWA shows that this typical grating provides substantial coupling between propagating modes and the evanescent spectrum covered by the first seven diffraction orders which potentially yields a resolution of $\lambda_0/20$ [Fig. 4.1(b)]. To simulate experimental conditions, we calculate the intensity behind the grating using the FEM commercial software [204], and use the calculated intensity as the "experimental" input field. The good agreement of our retrieval technique for the single and double slits and their original configurations is shown in Fig. 4.4 and Fig. 4.6(a), respectively.

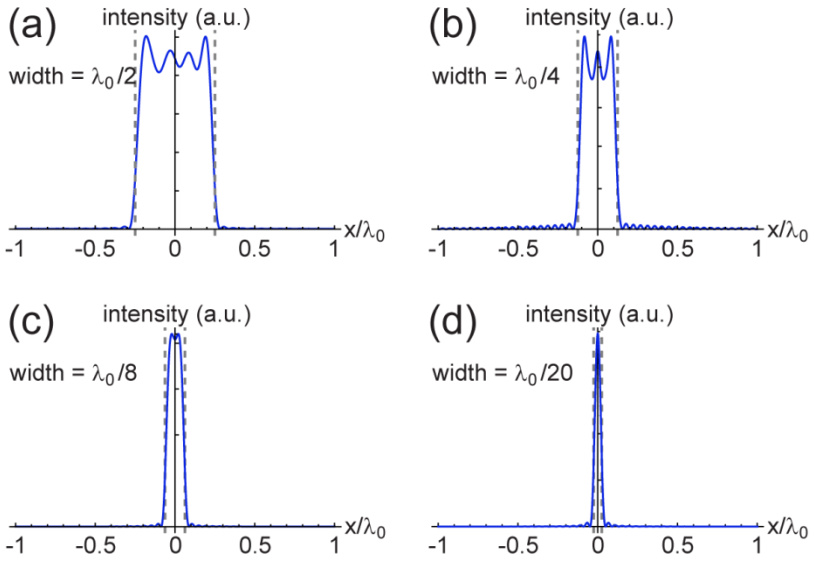

FIGURE 4.4: Reconstruction (blue solid curves) of single slits with width (a) $\lambda_0/2$, (b) $\lambda_0/4$, (c) $\lambda_0/8$, and (d) $\lambda_0/20$; gray dashed lines represent original sizes of the slits; air-to-air measurement is assumed.

We further apply the developed formalism to recover the field distribution at the focal plane of the planar subwavelength focusing device based on the strongly anisotropic metamaterials,

hypergrating [see Chapter 3]. The TM-polarized field of wavelength $\lambda_0 = 20\,\mu m$ is incident on the hypergrating structure with the particular metamaterial parameter: $\varepsilon_{xy} = -23.25 + 3.65i$ and $\varepsilon_z = 24.84 + 0.69i$ [16, 149], and the subwavelength focal spot is found at a distance behind the diffraction plate. With this positive-refraction metamaterial, small k_x components of the field are suppressed, so that the image recovery can be achieved with only single θ_{inc} measurement. The parameters of the Cu grating are $\varepsilon_g = -12662.6 + 3726.0i$ [149], $h = \lambda_0/80$, $f = 0.5$, and $\Lambda = \lambda_0/\left(\sqrt{\varepsilon_z} + \sqrt{\varepsilon_0}\right)$. Fig. 4.6(b) shows good agreement of subwavelength focal spot retrieval and FEM simulation.

Finally, we analyze the tolerance of the imaging algorithm to noise, present in any experiment, by adding a random 2% noise to the "experimental" field distributions from the single slits, and averaging the field recovered after several noise realizations. Our simulations demonstrate that the recovered image is not sensitive to the small experimental noise [Fig. 4.5].

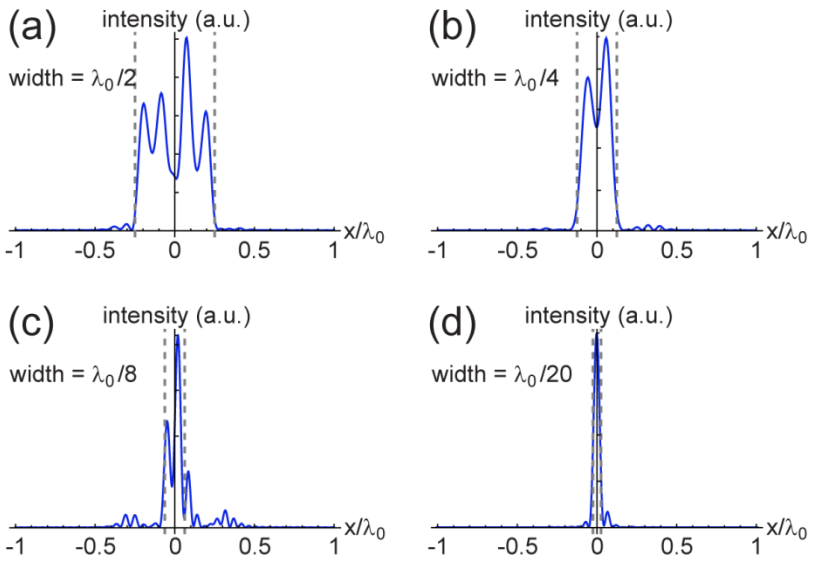

FIGURE 4.5: Reconstruction (blue solid curves) of single slits [as in Fig. 4.4] with a random 2% noise added in the experimental field distributions.

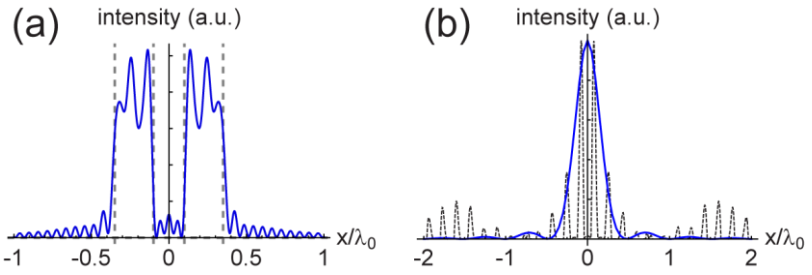

FIGURE 4.6: (a) Reconstruction of two $\lambda_0/4$ slits separated by $\lambda_0/5$ (air-to-air measurement); (b) reconstruction of the subwavelength focal spot of the hypergrating based on measurements in air; solid blue and dotted black curves correspond to retrieved and original images, respectively; intensities from both methods are normalized; positive refraction metamaterial-to-air measurement is assumed.

We now discuss the advantages and limitations of the proposed technique. The main mechanism of the imaging retrieval depends only on designing the subwavelength diffraction grating to support the evanescent-to-propagating wave transformation in a particular material. Once the permittivities of the materials surrounding the object are known, an appropriate grating can be designed. The design of this grating does not depend on the shape of the object. In addition, our technique is not only limited to TM-polarized incident fields, because our structure does not need the slab of metallic layer to enhance the evanescent fields [19, 193].

The main limitation of the complete imaging retrieval is related to the robustness of a mathematical approach, employed to fit the unknown amplitude function [Eq. (4.8)] with experimental data. Moreover, the speed of real-time bimolecular imaging depends on the process of varying incident angles and fitting computation.

4.5 Conclusion

We proposed a technique capable of retrieving the size and shape of the unknown subwavelength objects with far-field measurements and computer post-procession. The

approach relies on a predesigned subwavelength diffraction grating scattering evanescent information into the far field and on a numerical algorithm that is capable of deconvoluting this information based on the far-field intensity measurements. We showed the robustness of the technique by retrieving subwavelength single and double slits, with and without noise, and determining the size of the subwavelength focal spot in infrared spectrum regime. As compared to the previously introduced techniques (SIM and FSL), the proposed approach is implicitly non-resonant, and thus provides a relatively large operating bandwidth. It also enables deep subwavelength resolution ($\leq \lambda_0/20$), and opens the door for high-resolution real-time imaging.

Chapter 5 - Wave-Matching Technique: Computing Light in Planar Structures

5.1 Introduction

Accurate numerical analysis of electromagnetic fields is required to adequately understand the behavior of plasmonic and metamaterial systems. Although a number of finite-difference and finite-elements [206] techniques can successfully solve the problem of scattering in relatively small geometries ($\lesssim 10\lambda_0$), analysis of wave propagation in an extended system is beyond the capabilities of methods that rely on finite-size meshing of space/time. One of the ways to reduce memory requirement to calculate the field in an extended structure with a moderate number of scattering interfaces is to implement some sort of wave-matching technique where the modal spectrum is constructed to satisfy the solutions of Maxwell's equations in the space, and only boundary conditions *at scattering interfaces* are enforced, resulting in calculations of *amplitudes* of the modes. Effectively, modal expansion can replace the need to calculate all field components at every *point of space* with the need to calculate modal amplitudes in every *region of space*.

One of the first descriptions of the wave-matching approach and its applications for highly conductive plasmonic guides can be found in Refs. [207, 208]. Ref. [207] also describes scattering by planar guides with highly symmetric cross-sections. Green's function formalism has been utilized to analyze out-of-plane scattering of plasmonic guides in Ref. [209]. An approach to calculate the modal cross-talk and scattering in 1D guides was developed in Ref. [210]. Scattering by periodically corrugated systems has been analyzed with rigorous coupled wave analysis in Refs. [199-202]. Basis expansion of electromagnetic field in piecewise rectangular structures was proposed in Ref. [211]. Recently, the generalization of

field expansion to calculate scattering in plasmonic planar guides has been presented in Ref. [212]. However, while the mode-matching calculations were proven to be highly efficient, this technique had failed in the proximity of the plasmon resonance condition, when the field of a surface wave is highly confined to the proximity of a metal interface. Here we present the extended wave-matching technique that is capable of solving for wave scattering in complex systems formed by coupled planar waveguides [137].

The rest of this Chapter is organized as follows. In Section 2, we will present the mode structure of an arbitrary planar guide used in this work. Section 3 will be devoted to the development of the mode-matching technique in a quasi-planar system comprising a uniform in y-direction array of planar guides. The extension of the technique to multistack structures will be proposed in Section 4. The presented numerical approach will be illustrated on examples of light propagation in several plasmonic and metamaterial systems in Section 5.

Notations: In this work, we use the following notations for the electric and magnetic fields in the system: the total electric (E) and magnetic (H) fields are shown in italic letters; the fields of modal components contributing to the total field are represented with symbols $\mathbb{E}$ and $\mathbb{H}$; the components of an individual mode in a particular layer of the multilayer stack are represented with calligraphic symbols $\mathcal{E}$ and $\mathcal{H}$.

5.2 Modal Spectrum of Planar Guides

We start from analysis of a modal spectrum of a planar waveguide, schematically shown in Fig. 5.1(a). The structure comprises a set of N planar layers with layer interfaces parallel to the yz plane, with the j-th layer occupying the space between $x_{j-1} < x \leq x_j$, and having the uniaxial dielectric tensor described by

$$\hat{\varepsilon}_j \doteq \begin{bmatrix} \varepsilon_{x;j} & 0 & 0 \\ 0 & \varepsilon_{yz;j} & 0 \\ 0 & 0 & \varepsilon_{yz;j} \end{bmatrix}. \tag{5.1}$$

We assume that $x_0 = -\infty$ and $x_N = \infty$. Here we consider the structure that is infinitely extended in the yz plane.

The electromagnetic fields in this layered system can be represented as a set of TE and TM polarized waves (modes). Each mode of the multilayer constitutes a solution of Maxwell's equations that is finite for $-\infty < x < \infty$ [116]. In a homogeneous layered structure, the mode can be parameterized by a combination of (i) its polarization (TE/TM), (ii) the in-plane components of the wavevector (k_y, k_z), and (iii) a set of layer-specific complex coefficients $\{a_j^{\pm}\}$ playing the role of amplitudes of the mode components:

$$\vec{\mathbb{E}}(k_y, k_z) = \begin{cases} a_1^+ \vec{\mathcal{E}}_1\big(k_{x;1}(k_y, k_z), k_y, k_z\big) + a_1^- \vec{\mathcal{E}}_1\big(-k_{x;1}(k_y, k_z), k_y, k_z\big), & x < x_1 \\ \dots \\ a_j^+ \vec{\mathcal{E}}_j\big(k_{x;j}(k_y, k_z), k_y, k_z\big) + a_j^- \vec{\mathcal{E}}_j\big(-k_{x;j}(k_y, k_z), k_y, k_z\big), & x_{j-1} < x < x_j \\ \dots \\ a_N^+ \vec{\mathcal{E}}_N\big(k_{x;N}(k_y, k_z), k_y, k_z\big) + a_N^- \vec{\mathcal{E}}_N\big(-k_{x;N}(k_y, k_z), k_y, k_z\big), & x_{N-1} < x \end{cases}, \tag{5.2}$$

$$\vec{\mathbb{H}}(k_y, k_z) = \begin{cases} a_1^+ \vec{\mathcal{H}}_1\big(k_{x;1}(k_y, k_z), k_y, k_z\big) + a_1^- \vec{\mathcal{H}}_1\big(-k_{x;1}(k_y, k_z), k_y, k_z\big), & x < x_1 \\ \dots \\ a_j^+ \vec{\mathcal{H}}_j\big(k_{x;j}(k_y, k_z), k_y, k_z\big) + a_j^- \vec{\mathcal{H}}_j\big(-k_{x;j}(k_y, k_z), k_y, k_z\big), & x_{j-1} < x < x_j \\ \dots \\ a_N^+ \vec{\mathcal{H}}_N\big(k_{x;N}(k_y, k_z), k_y, k_z\big) + a_N^- \vec{\mathcal{H}}_N\big(-k_{x;N}(k_y, k_z), k_y, k_z\big), & x_{N-1} < x \end{cases}, \tag{5.3}$$

where the fields and dispersion relations in each layer are described by

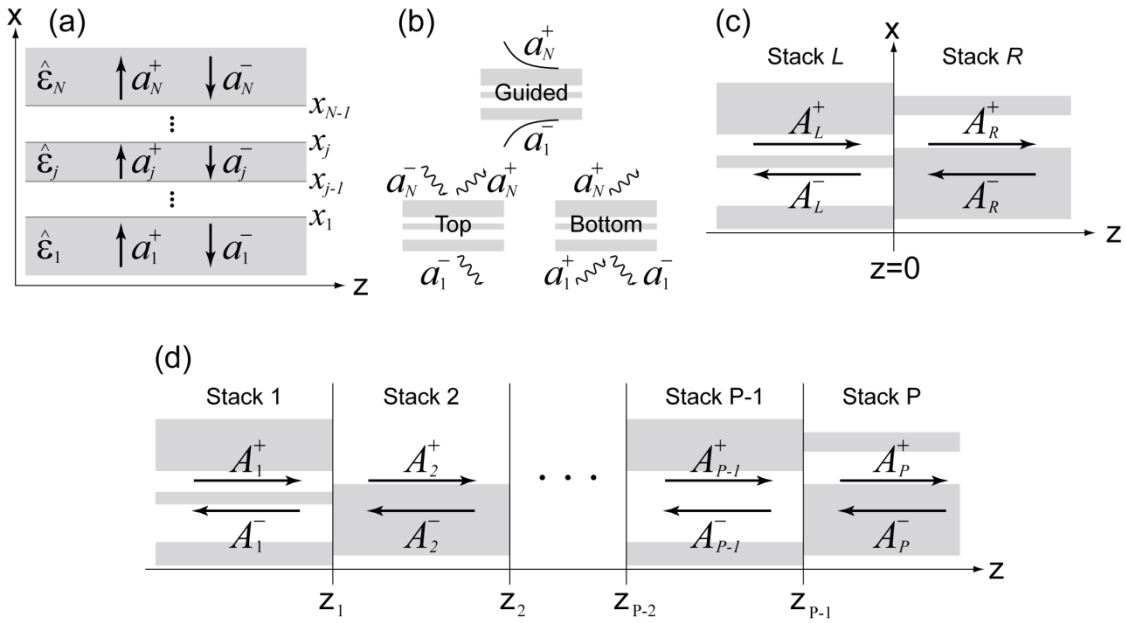

FIGURE 5.1: Schematic geometry of the multilayered structures and electromagnetic mode types; geometry of the single multilayer stack is shown in (a); coefficients $a_j^{\pm}$ play the role of amplitudes of the mode components in each layer; panel (b) explains the composition of top, bottom, and guided modes; field profiles in the outmost layers of the multilayer are shown; the interface between two multilayer stacks is shown in (c); modal amplitudes constituting total fields in each stack are given as $A^{\pm}$; panel (d) shows geometry of P-stack structure with $(P-1)$ interfaces; reprinted with permission from Ref. [137].

$$\text{TE – polarized waves: } \begin{cases} \vec{\mathcal{E}}_j = \frac{e^{-i\omega t + i\vec{k}\cdot\vec{r}}}{\sqrt{k_y^2+k_z^2}} & \{0, \quad k_z, \quad -k_y\} \\ \vec{\mathcal{H}}_j = \frac{e^{-i\omega t + i\vec{k}\cdot\vec{r}}}{\sqrt{k_y^2+k_z^2}} \frac{c}{\omega} & \{-(k_y^2+k_z^2),\ k_{x;j}k_y,\ k_{x;j}k_z\}, \\ \frac{k_{x;j}^2+k_y^2+k_z^2}{\varepsilon_{yz;j}} = \frac{\omega^2}{c^2} & \end{cases} \tag{5.4}$$

$$\text{TM – polarized waves: } \begin{cases} \vec{\mathcal{E}}_j = \frac{e^{-i\omega t + i\vec{k}\cdot\vec{r}}}{k_y^2+k_z^2} & \left\{k_y^2+k_z^2,\ -\frac{\varepsilon_{x;j}}{\varepsilon_{yz;j}}\,k_{x;j}k_y,\ -\frac{\varepsilon_{x;j}}{\varepsilon_{yz;j}}\,k_{x;j}k_z\right\} \\ \vec{\mathcal{H}}_j = \frac{e^{-i\omega t + i\vec{k}\cdot\vec{r}}}{k_y^2+k_z^2} \frac{\omega}{c} & \{0, \quad \varepsilon_{x;j}k_z, \quad -\varepsilon_{x;j}k_y\} \\ \frac{k_{x;j}^2}{\varepsilon_{yz;j}} + \frac{k_y^2+k_z^2}{\varepsilon_{x;j}} = \frac{\omega^2}{c^2} & \end{cases} . \tag{5.5}$$

Note that for a given mode only two of the amplitudes $a_j^{\pm}$ are independent to each other. Indeed, the remaining amplitudes can be calculated using the well-known transfer matrix method [Appendix A]:

$$\begin{pmatrix} a_{j+1}^- \\ a_{j+1}^+ \end{pmatrix} = \alpha_j \begin{bmatrix} (1+K_j)\varphi_j^- & (1-K_j)\varphi_j^+ \\ (1-K_j)/\varphi_j^+ & (1+K_j)/\varphi_j^- \end{bmatrix} \begin{pmatrix} a_j^- \\ a_j^+ \end{pmatrix} \tag{5.6}$$

with polarization-dependent parameters φ_j, α_j, and K_j given by $\varphi_j^{\pm} = exp\left[i\left(k_{x;j+1} \pm k_{x;j}\right)x_j\right]$, $\alpha_j^{TE} = 1/2$, $\alpha_j^{TM} = \varepsilon_{x;j}/\left(2\varepsilon_{x;j+1}\right)$, $K_j^{TE} = k_{x;j}/k_{x;j+1}$, and $K_j^{TM} = k_{x;j}\varepsilon_{yz;j+1}/\left(k_{x;j+1}\varepsilon_{yz;j}\right)$.

For multilayer systems, layer-specific transfer matrices can be multiplied together, yielding the transfer-matrix relating the fields in any two layers of the multilayer stack, and thus solving the problem of reflection and transmission of a plane wave by the multilayer composite. The singular solution that corresponds to nonzero scattered waves on both sides of the multilayer structure ($a_1^-, a_N^+ \neq 0$) with zero incident fields ($a_1^+ = a_N^- = 0$) corresponds to the eigen (guided) mode of the stack [116, 207, 210].

For each polarization, the full spectrum of modes supported by the stack includes three groups of waves [Fig. 5.1(b)]. The first group contains a discrete spectrum of guided modes, exponentially decaying into first and last layers ($a_1^+ = a_N^- = 0, a_1^- = 1$). Here we characterize these waves by the in-plane components of their wavevectors $\{k_y, k_z\}$. The remaining groups of modes contain the continuum of waves, known as open-waveguide modes [207, 212] (bulk modes). The first of these groups represents the modes originated by a plane wave that is incident on the layered structure from the top layer ($a_1^+ = 0, a_N^- = 1$), while the second group represents the wave incident on the structure from the bottom layer

$(a_1^+ = 1, a_N^- = 0)$. Here, the modes of the first group ("top modes") are parameterized by the real-valued $k_{x;N}$ in the top $\left(N^{th}\right)$ layer, while the "bottom modes" are parameterized by the real-valued $k_{x;1}$ in the bottom (1^{st}) layer.

In the limit of symmetric distribution of permittivity $\hat{\varepsilon}(x) = \hat{\varepsilon}(-x)$, the spectrum of top and bottom modes proposed here is equivalent to the earlier proposed [207] combinations of "standing wave" modes with symmetric and antisymmetric x-profiles. However, in contrast to the later, the combination of top and bottom modes is more easily generalizable to the case of nonsymmetric (such as plasmonic) planar guides. Note that in a majority of previous studies of plasmonic structures [212], bottom modes were explicitly omitted. As will be explained below, this omission becomes crucial in the regime of strong surface plasmon polariton (SPP) [92, 93] scattering, e.g., in proximity to SPP resonance or in plasmonic step geometry [Fig. 5.4]. Overall, the field inside the guiding structure can be written as

$$\begin{aligned}\vec{E} = &\sum_q \left[A^{(q)^+}\vec{\mathbb{E}}\left(k_y, k_z^{(q)}\right) + A^{(q)^-}\vec{\mathbb{E}}\left(k_y, -k_z^{(q)}\right)\right] \\ &+ \int_0^\infty \left[A^{top^+}\left(k_{x;N}\right)\vec{\mathbb{E}}\left(k_y, k_z\left(k_{x;N}\right)\right) + A^{top^-}\left(k_{x;N}\right)\vec{\mathbb{E}}\left(k_y, -k_z\left(k_{x;N}\right)\right)\right] dk_{x;N} \\ &+ \int_0^\infty \left[A^{btm^+}\left(k_{x;1}\right)\vec{\mathbb{E}}\left(k_y, k_z\left(k_{x;1}\right)\right) + A^{btm^-}\left(k_{x;1}\right)\vec{\mathbb{E}}\left(k_y, -k_z\left(k_{x;1}\right)\right)\right] dk_{x;1}\ ,\end{aligned}$$

(5.7)

$$\begin{aligned}\vec{H} = &\sum_q \left[A^{(q)^+}\vec{\mathbb{H}}\left(k_y, k_z^{(q)}\right) + A^{(q)^-}\vec{\mathbb{H}}\left(k_y, -k_z^{(q)}\right)\right] \\ &+ \int_0^\infty \left[A^{top^+}\left(k_{x;N}\right)\vec{\mathbb{H}}\left(k_y, k_z\left(k_{x;N}\right)\right) + A^{top^-}\left(k_{x;N}\right)\vec{\mathbb{H}}\left(k_y, -k_z\left(k_{x;N}\right)\right)\right] dk_{x;N} \\ &+ \int_0^\infty \left[A^{btm^+}\left(k_{x;1}\right)\vec{\mathbb{H}}\left(k_y, k_z\left(k_{x;1}\right)\right) + A^{btm^-}\left(k_{x;1}\right)\vec{\mathbb{H}}\left(k_y, -k_z\left(k_{x;1}\right)\right)\right] dk_{x;1}\ .\end{aligned}$$

(5.8)

The first terms in Eqs. (5.7) and (5.8) represent the summation of all guided modes, while the remaining two terms integrate all possible open-waveguide modes. Here we assume that all the modes in the layered material have the same value of k_y. This assumption does not limit the applicability of the developed technique, since due to translational symmetry any solution of Maxwell's equations in the set of coupled waveguides can be represented as a linear combination of solutions corresponding to a set of k_y values. Likewise, we assume that excitation and response of the system are monochromatic $[E, H \propto exp(-i\omega t)]$. The linearity of Maxwell's equations makes it possible to generalize the developed formalism for the arbitrary pulse excitation by representing the incident radiation by the linear combination of monochromatic waves.

Note that in the process of calculating waveguide modes it may be necessary to determine the proper sign of the k_x (or k_z) component of the wavevector in a particular layer. If the component of the wavevector has complex value, this sign is determined from the requirement for the mode to be finite in its domain. If the wavevector component is real, its sign should be determined to impose the propagation of energy in the positive x (or z) direction [42, 213].

The set of waveguide modes defined above allows the introduction of the scalar product

$$\langle \vec{\mathbb{E}}_1 | \vec{\mathbb{H}}_2^{\dagger} \rangle = \int_{-\infty}^{\infty} (\vec{\mathbb{E}}_1 \times \vec{\mathbb{H}}_2^{\dagger}) \cdot \hat{z} dx \tag{5.9}$$

where the dagger (†) corresponds to the adjoined field, i.e., field of the mode propagating in the reversed z direction [207, 210]. It can be shown [207, 210, 212] that in a given multilayer (i) all TM-polarized waves are orthogonal to all TE-polarized waves, (ii) the guided modes are

orthogonal to each other, and (iii) the top and bottom modes may have some coupling, depending on $\hat{\varepsilon}_1$ and $\hat{\varepsilon}_N$: if $\hat{\varepsilon}_1 = \hat{\varepsilon}_N$, the top and bottom modes corresponding to the same value of k_x are coupled to each other and are orthogonal to all other modes; if one of the two materials is lossy (as is usually the case with plasmonic structures), the top and bottom modes are, as a rule, orthogonal to each other.

Note that, similar to what has been suggested in Ref. [212], the scalar product can be calculated analytically, significantly speeding up the calculation [Appendix C].

5.3 Mode Coupling Across Two Multilayer Stacks

We now turn to the main point of this work – discussion of coupling of the modes at the boundary between the two multilayer structures. For simplicity, we present results for the case when the interface is located at $z = 0$ [Fig. 5.1(c)]. Generalization of the technique for other locations of the interface is straightforward.

We are solving the classical scattering problem: finding the fields scattered by the interface provided that the incident fields are known. The incident fields are represented by the modes propagating in the $+z$ direction on the left-hand side of the interface ($z < 0$) and by the modes travelling in the $-z$ direction on the right-hand side of the interface ($z > 0$); the scattered fields are represented by the modes travelling in the $-z$ direction on the left-hand side of the interface and by the modes travelling in the $+z$ direction on the right-hand side of the interface. The modal representation [Eqs. (5.7)-(5.8)] reduces the scattering problem to an arithmetic task of finding the coefficients A_L^- and A_R^+ as a function of A_L^+ and A_R^-, which can be solved by imposing the following set of boundary conditions:

$$E_{L_x} = E_{R_x}\,; \qquad H_{L_y} = H_{R_y}\,, \tag{5.10}$$

$$E_{L_y} = E_{R_y}\,; \qquad H_{L_x} = H_{R_x}\,. \tag{5.11}$$

As can be explicitly verified, the remaining boundary conditions follow from Eqs. (5.10)-(5.11). In the case of normal incidence $(k_y = 0)$, TM- and TE-modes do not couple to each other. Correspondingly, in this case Eqs. (5.10) describe the reflection, transmission, and scattering of TM-polarized waves, while Eqs. (5.11) describe the optical properties of TE-polarized modes.

In order to solve the scattering problem, Eqs. (5.10)-(5.11) need to be converted into a set of coupled linear equations which contain amplitudes of the scattered modes. To achieve this goal, we substitute the modal expansion [Eqs. (5.7)-(5.8)] in Eqs. (5.10)-(5.11), and subsequently multiply the resulting expressions by the adjoined fields of left- and right-hand side modes, as will be described below.

In numerical computations, it is necessary to replace the continuous integration over k_x with finite sums. Thus, Eqs. (5.7)-(5.8) become

$$\vec{E} = \sum_m \left[A^{(m)^+}\vec{\mathbb{E}}^{(m)^+} + A^{(m)^-}\vec{\mathbb{E}}^{(m)^-}\right] w^{(m)}\,, \tag{5.12}$$

$$\vec{H} = \sum_m \left[A^{(m)^+}\vec{\mathbb{H}}^{(m)^+} + A^{(m)^-}\vec{\mathbb{H}}^{(m)^-}\right] w^{(m)}\,, \tag{5.13}$$

where $\vec{\mathbb{E}}^{(m)^\pm} \equiv \vec{\mathbb{E}}\left(k_y, \pm k_z^{(m)}\right)$, and similar for $\vec{\mathbb{H}}$; the summation in Eqs. (5.12)-(5.13) go over all modes (top, bottom, and guided) of TE and TM polarizations, and the weight factors *w* are equal to 1 for the guided modes, and are determined by the numerical integration method used for top and bottom modes [203]. Note that the number of modes on the left-hand side of the

interface (N_L) does not necessarily equal the number of modes on the right-hand side of the interface (N_R). Eqs. (5.10)-(5.11) now become

$$\sum_{m=1}^{N_L}\left[A_L^{(m)^+}\mathbb{E}_{L_x}^{(m)^+}+A_L^{(m)^-}\mathbb{E}_{L_x}^{(m)^-}\right]w_L^{(m)}=\sum_{m=1}^{N_R}\left[A_R^{(m)^+}\mathbb{E}_{R_x}^{(m)^+}+A_R^{(m)^-}\mathbb{E}_{R_x}^{(m)^-}\right]w_R^{(m)},$$

$$\sum_{m=1}^{N_L}\left[A_L^{(m)^+}\mathbb{H}_{L_y}^{(m)^+}+A_L^{(m)^-}\mathbb{H}_{L_y}^{(m)^-}\right]w_L^{(m)}=\sum_{m=1}^{N_R}\left[A_R^{(m)^+}\mathbb{H}_{R_y}^{(m)^+}+A_R^{(m)^-}\mathbb{H}_{R_y}^{(m)^-}\right]w_R^{(m)},\tag{5.14}$$

$$\sum_{m=1}^{N_L}\left[A_L^{(m)^+}\mathbb{E}_{L_y}^{(m)^+}+A_L^{(m)^-}\mathbb{E}_{L_y}^{(m)^-}\right]w_L^{(m)}=\sum_{m=1}^{N_R}\left[A_R^{(m)^+}\mathbb{E}_{R_y}^{(m)^+}+A_R^{(m)^-}\mathbb{E}_{R_y}^{(m)^-}\right]w_R^{(m)},$$

$$\sum_{m=1}^{N_L}\left[A_L^{(m)^+}\mathbb{H}_{L_x}^{(m)^+}+A_L^{(m)^-}\mathbb{H}_{L_x}^{(m)^-}\right]w_L^{(m)}=\sum_{m=1}^{N_R}\left[A_R^{(m)^+}\mathbb{H}_{R_x}^{(m)^+}+A_R^{(m)^-}\mathbb{H}_{R_x}^{(m)^-}\right]w_R^{(m)}.\tag{5.15}$$

To solve for N_R+N_L unknown amplitudes, we multiply Eqs. (5.10) by the fields of TM-polarized modes and integrate the resulting products over x; similarly, we multiply Eqs. (5.11) by the fields of TE-polarized modes and perform the integration. Assuming that the index m first spans the TE-polarized and then TM-polarized waves, the procedure results in the following two sets of matrix equations:

$$\widehat{\mathfrak{E}_{\Re L}^{+}}^{nm}A_L^{(m)^+}+\widehat{\mathfrak{E}_{\Re L}^{-}}^{nm}A_L^{(m)^-}=\widehat{\mathfrak{E}_{\Re R}^{+}}^{nm}A_R^{(m)^+}+\widehat{\mathfrak{E}_{\Re R}^{-}}^{nm}A_R^{(m)^-},$$

$$\widehat{\mathfrak{H}_{\Re L}^{+}}^{nm}A_L^{(m)^+}+\widehat{\mathfrak{H}_{\Re L}^{-}}^{nm}A_L^{(m)^-}=\widehat{\mathfrak{H}_{\Re R}^{+}}^{nm}A_R^{(m)^+}+\widehat{\mathfrak{H}_{\Re R}^{-}}^{nm}A_R^{(m)^-},\tag{5.16}$$

and

$$\widehat{\mathfrak{E}_{\mathfrak{L}L}^{+}}^{nm} A_L^{(m)^+} + \widehat{\mathfrak{E}_{\mathfrak{L}L}^{-}}^{nm} A_L^{(m)^-} = \widehat{\mathfrak{E}_{\mathfrak{L}R}^{+}}^{nm} A_R^{(m)^+} + \widehat{\mathfrak{E}_{\mathfrak{L}R}^{-}}^{nm} A_R^{(m)^-} ,$$

$$\widehat{\mathfrak{H}_{\mathfrak{L}L}^{+}}^{nm} A_L^{(m)^+} + \widehat{\mathfrak{H}_{\mathfrak{L}L}^{-}}^{nm} A_L^{(m)^-} = \widehat{\mathfrak{H}_{\mathfrak{L}R}^{+}}^{nm} A_R^{(m)^+} + \widehat{\mathfrak{H}_{\mathfrak{L}R}^{-}}^{nm} A_R^{(m)^-}, \tag{5.17}$$

where the summation over repeated index m is assumed and matrix elements are given by

$$\mathfrak{E}_{\mathfrak{R}\{L|R\}}^{\pm nm} = w_{\{L|R\}}^{(m)} \begin{cases} \int_{-\infty}^{\infty} \mathbb{E}_{\{L|R\}_y}^{(m)^{\pm}} \mathbb{H}_{R_x}^{(n)^-} dx , & n \le N_R^{TE} \\ \int_{-\infty}^{\infty} \mathbb{E}_{\{L|R\}_x}^{(m)^{\pm}} \mathbb{H}_{R_y}^{(n)^-} dx , & n > N_R^{TE} \end{cases},$$

$$\mathfrak{H}_{\mathfrak{R}\{L|R\}}^{\pm nm} = w_{\{L|R\}}^{(m)} \begin{cases} \int_{-\infty}^{\infty} \mathbb{H}_{\{L|R\}_x}^{(m)^{\pm}} \mathbb{E}_{R_y}^{(n)^-} dx , & n \le N_R^{TE} \\ \int_{-\infty}^{\infty} \mathbb{H}_{\{L|R\}_y}^{(m)^{\pm}} \mathbb{E}_{R_x}^{(n)^-} dx , & n > N_R^{TE} \end{cases},$$

$$\mathfrak{E}_{\mathfrak{L}\{L|R\}}^{\pm nm} = w_{\{L|R\}}^{(m)} \begin{cases} \int_{-\infty}^{\infty} \mathbb{E}_{\{L|R\}_y}^{(m)^{\pm}} \mathbb{H}_{L_x}^{(n)^-} dx , & n \le N_L^{TE} \\ \int_{-\infty}^{\infty} \mathbb{E}_{\{L|R\}_x}^{(m)^{\pm}} \mathbb{H}_{L_y}^{(n)^-} dx , & n > N_L^{TE} \end{cases},$$

$$\mathfrak{H}_{\mathfrak{L}\{L|R\}}^{\pm nm} = w_{\{L|R\}}^{(m)} \begin{cases} \int_{-\infty}^{\infty} \mathbb{H}_{\{L|R\}_x}^{(m)^{\pm}} \mathbb{E}_{L_y}^{(n)^-} dx , & n \le N_L^{TE} \\ \int_{-\infty}^{\infty} \mathbb{H}_{\{L|R\}_y}^{(m)^{\pm}} \mathbb{E}_{L_x}^{(n)^-} dx , & n > N_L^{TE} \end{cases}. \tag{5.18}$$

An example of the matrix $\widehat{\mathfrak{E}_{\mathfrak{R}L}^{\pm}}$ formation is illustrated in Fig. 5.2; the formations of other matrices are similar. The modes of $z < 0$ region are not necessarily orthogonal to the modes in the $z > 0$ region. Thus, the matrices $\widehat{\mathfrak{E}_{\mathfrak{R}L}^{\pm}}$, $\widehat{\mathfrak{H}_{\mathfrak{R}L}^{\pm}}$, $\widehat{\mathfrak{E}_{\mathfrak{L}R}^{\pm}}$, and $\widehat{\mathfrak{H}_{\mathfrak{L}R}^{\pm}}$ may have substantial nondiagonal components describing cross-talk between modes across the interface. Note that in the planar structure, the scalar product yields analytical solution [see Appendix C]. The improper integration can be chopped into segments according to layers in both stacks.

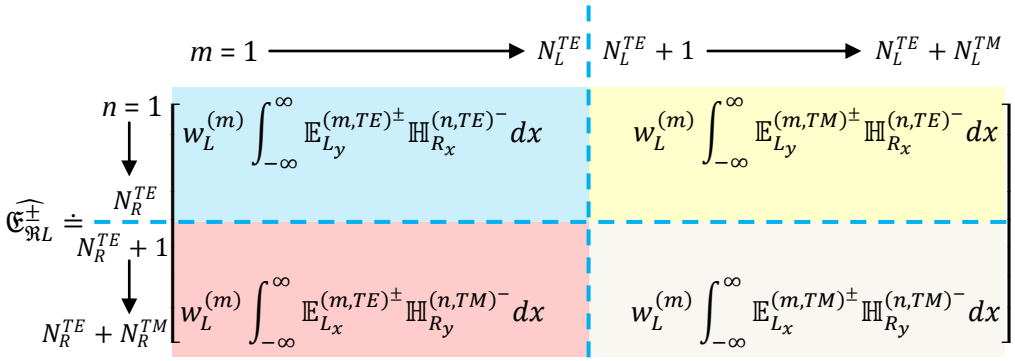

FIGURE 5.2: Matrix $\widehat{\mathfrak{E}}_{\mathfrak{R}L}^{\pm}$ formation; columns (m) are from the discretization of the continuous integration over k_x where N^{TE} and N^{TM} are the number of TE and TM k_x-discrete modes; the adjoined TM- and TE-polarized fields are multiplied to make rows (n).

In fact, the above matrices are square and invertible only when $N_L = N_R$, in which case one of Eqs. (5.16)-(5.17) can provide the information required to solve the scattering problem. However, even in this case, inversion procedure may lead to significant numerical problems and is undesirable. When $N_L \neq N_R$ these matrices are *rectangular* and thus, even theoretically, cannot be inverted. To overcome this difficulty, we reduce Eqs. (5.16)-(5.17) to the following set of equations that represent the generalization of transfer-matrix formalism for coupled waveguide structures:

$$\begin{cases} \vec{A}_R^- = \widehat{\mathfrak{R}_{11}}\vec{A}_L^- + \widehat{\mathfrak{R}_{12}}\vec{A}_L^+ \\ \vec{A}_R^+ = \widehat{\mathfrak{R}_{21}}\vec{A}_L^- + \widehat{\mathfrak{R}_{22}}\vec{A}_L^+ \end{cases}, \tag{5.19}$$

$$\begin{cases} \vec{A}_L^- = \widehat{\mathfrak{L}_{11}}\vec{A}_R^- + \widehat{\mathfrak{L}_{12}}\vec{A}_R^+ \\ \vec{A}_L^+ = \widehat{\mathfrak{L}_{21}}\vec{A}_R^- + \widehat{\mathfrak{L}_{22}}\vec{A}_R^+ \end{cases}. \tag{5.20}$$

where $\vec{A}_{\{L|R\}}^{\pm} \equiv \left\{ A_{\{L|R\}}^{(1)^{\pm}}, \ldots, A_{\{L|R\}}^{\left(N_{\{L|R\}}\right)^{\pm}} \right\}$ and

$$\begin{cases} \widehat{\mathfrak{R}_{11}} = \left[\widehat{\mathfrak{E}_{\mathfrak{R}R}^{+}}^{-1}\widehat{\mathfrak{E}_{\mathfrak{R}R}^{-}} - \widehat{\mathfrak{H}_{\mathfrak{R}R}^{+}}^{-1}\widehat{\mathfrak{H}_{\mathfrak{R}R}^{-}}\right]^{-1}\left[\widehat{\mathfrak{E}_{\mathfrak{R}R}^{+}}^{-1}\widehat{\mathfrak{E}_{\mathfrak{R}L}^{-}} - \widehat{\mathfrak{H}_{\mathfrak{R}R}^{+}}^{-1}\widehat{\mathfrak{H}_{\mathfrak{R}L}^{-}}\right] \\ \widehat{\mathfrak{R}_{12}} = \left[\widehat{\mathfrak{E}_{\mathfrak{R}R}^{+}}^{-1}\widehat{\mathfrak{E}_{\mathfrak{R}R}^{-}} - \widehat{\mathfrak{H}_{\mathfrak{R}R}^{+}}^{-1}\widehat{\mathfrak{H}_{\mathfrak{R}R}^{-}}\right]^{-1}\left[\widehat{\mathfrak{E}_{\mathfrak{R}R}^{+}}^{-1}\widehat{\mathfrak{E}_{\mathfrak{R}L}^{+}} - \widehat{\mathfrak{H}_{\mathfrak{R}R}^{+}}^{-1}\widehat{\mathfrak{H}_{\mathfrak{R}L}^{+}}\right] \\ \widehat{\mathfrak{R}_{21}} = \left[\widehat{\mathfrak{E}_{\mathfrak{R}R}^{-}}^{-1}\widehat{\mathfrak{E}_{\mathfrak{R}R}^{+}} - \widehat{\mathfrak{H}_{\mathfrak{R}R}^{-}}^{-1}\widehat{\mathfrak{H}_{\mathfrak{R}R}^{+}}\right]^{-1}\left[\widehat{\mathfrak{E}_{\mathfrak{R}R}^{-}}^{-1}\widehat{\mathfrak{E}_{\mathfrak{R}L}^{-}} - \widehat{\mathfrak{H}_{\mathfrak{R}R}^{-}}^{-1}\widehat{\mathfrak{H}_{\mathfrak{R}L}^{-}}\right] \\ \widehat{\mathfrak{R}_{22}} = \left[\widehat{\mathfrak{E}_{\mathfrak{R}R}^{-}}^{-1}\widehat{\mathfrak{E}_{\mathfrak{R}R}^{+}} - \widehat{\mathfrak{H}_{\mathfrak{R}R}^{-}}^{-1}\widehat{\mathfrak{H}_{\mathfrak{R}R}^{+}}\right]^{-1}\left[\widehat{\mathfrak{E}_{\mathfrak{R}R}^{-}}^{-1}\widehat{\mathfrak{E}_{\mathfrak{R}L}^{+}} - \widehat{\mathfrak{H}_{\mathfrak{R}R}^{-}}^{-1}\widehat{\mathfrak{H}_{\mathfrak{R}L}^{+}}\right] \end{cases}, \tag{5.21}$$

$$\begin{cases} \widehat{\mathfrak{L}_{11}} = \left[\widehat{\mathfrak{E}_{\mathfrak{L}L}^{+}}^{-1}\widehat{\mathfrak{E}_{\mathfrak{L}L}^{-}} - \widehat{\mathfrak{H}_{\mathfrak{L}L}^{+}}^{-1}\widehat{\mathfrak{H}_{\mathfrak{L}L}^{-}}\right]^{-1}\left[\widehat{\mathfrak{E}_{\mathfrak{L}L}^{+}}^{-1}\widehat{\mathfrak{E}_{\mathfrak{L}R}^{-}} - \widehat{\mathfrak{H}_{\mathfrak{L}L}^{+}}^{-1}\widehat{\mathfrak{H}_{\mathfrak{L}R}^{-}}\right] \\ \widehat{\mathfrak{L}_{12}} = \left[\widehat{\mathfrak{E}_{\mathfrak{L}L}^{+}}^{-1}\widehat{\mathfrak{E}_{\mathfrak{L}L}^{-}} - \widehat{\mathfrak{H}_{\mathfrak{L}L}^{+}}^{-1}\widehat{\mathfrak{H}_{\mathfrak{L}L}^{-}}\right]^{-1}\left[\widehat{\mathfrak{E}_{\mathfrak{L}L}^{+}}^{-1}\widehat{\mathfrak{E}_{\mathfrak{L}R}^{+}} - \widehat{\mathfrak{H}_{\mathfrak{L}L}^{+}}^{-1}\widehat{\mathfrak{H}_{\mathfrak{L}R}^{+}}\right] \\ \widehat{\mathfrak{L}_{21}} = \left[\widehat{\mathfrak{E}_{\mathfrak{L}L}^{-}}^{-1}\widehat{\mathfrak{E}_{\mathfrak{L}L}^{+}} - \widehat{\mathfrak{H}_{\mathfrak{L}L}^{-}}^{-1}\widehat{\mathfrak{H}_{\mathfrak{L}L}^{+}}\right]^{-1}\left[\widehat{\mathfrak{E}_{\mathfrak{L}L}^{-}}^{-1}\widehat{\mathfrak{E}_{\mathfrak{L}R}^{-}} - \widehat{\mathfrak{H}_{\mathfrak{L}L}^{-}}^{-1}\widehat{\mathfrak{H}_{\mathfrak{L}R}^{-}}\right] \\ \widehat{\mathfrak{L}_{22}} = \left[\widehat{\mathfrak{E}_{\mathfrak{L}L}^{-}}^{-1}\widehat{\mathfrak{E}_{\mathfrak{L}L}^{+}} - \widehat{\mathfrak{H}_{\mathfrak{L}L}^{-}}^{-1}\widehat{\mathfrak{H}_{\mathfrak{L}L}^{+}}\right]^{-1}\left[\widehat{\mathfrak{E}_{\mathfrak{L}L}^{-}}^{-1}\widehat{\mathfrak{E}_{\mathfrak{L}R}^{+}} - \widehat{\mathfrak{H}_{\mathfrak{L}L}^{-}}^{-1}\widehat{\mathfrak{H}_{\mathfrak{L}R}^{+}}\right] \end{cases}. \tag{5.22}$$

Finally, combining the second equation of Eqs. (5.19) and the first equation of Eqs. (5.20), we arrive to the generalization of the scattering-matrix technique that solves the problem of interlayer coupling:

$$\begin{cases} \vec{A}_L^- = \left[\hat{I} - \widehat{\mathfrak{L}_{12}}\widehat{\mathfrak{R}_{21}}\right]^{-1}\widehat{\mathfrak{L}_{11}} & \vec{A}_R^- + \left[\hat{I} - \widehat{\mathfrak{L}_{12}}\widehat{\mathfrak{R}_{21}}\right]^{-1}\widehat{\mathfrak{L}_{12}}\widehat{\mathfrak{R}_{22}} \quad \vec{A}_L^+ \\ \vec{A}_R^+ = \left[\hat{I} - \widehat{\mathfrak{R}_{21}}\widehat{\mathfrak{L}_{12}}\right]^{-1}\widehat{\mathfrak{R}_{21}}\widehat{\mathfrak{L}_{11}} & \vec{A}_R^- + \left[\hat{I} - \widehat{\mathfrak{R}_{21}}\widehat{\mathfrak{L}_{12}}\right]^{-1}\widehat{\mathfrak{R}_{22}} \quad \vec{A}_L^+ \end{cases} \tag{5.23}$$

with $\hat{I}$ being identity matrices. Eqs. (5.23) represent the main result of this Section.

5.4 Wave Calculation in Multistack Structure

In this Section, the wave-matching technique is extended to any general P-stack structure [Fig. 5.1(d)]. Let unknown coefficients in p-th stack be defined as $\vec{A}_p^{\pm} \equiv \left\{A_p^{(1)^{\pm}}, \dots, A_p^{(N_p)^{\pm}}\right\}$; therefore, we are solving the classical scattering problem in which the coefficients $\vec{A}_1^-$ and $\vec{A}_P^+$ are described as a function of $\vec{A}_1^+$ and $\vec{A}_P^-$. The set of two-stack transfer-matrix equations [Eqs. (5.19)-(5.20)] can be extended for P-stack structures:

$$\begin{bmatrix} \vec{A}_P^- \\ \vec{A}_P^+ \end{bmatrix} = \widehat{\Re}_{Total} \begin{bmatrix} \vec{A}_1^- \\ \vec{A}_1^+ \end{bmatrix}, \tag{5.24}$$

$$\begin{bmatrix} \vec{A}_1^- \\ \vec{A}_1^+ \end{bmatrix} = \widehat{\Omega}_{Total} \begin{bmatrix} \vec{A}_N^- \\ \vec{A}_N^+ \end{bmatrix}, \tag{5.25}$$

where

$$\widehat{\Re}_{Total} = \widehat{\Re}_{(P-1\to P)} \widehat{\Re}_{(P-2\to P-1)} \dots \widehat{\Re}_{(2\to 3)} \widehat{\Re}_{(1\to 2)}, \tag{5.26}$$

$$\widehat{\Omega}_{Total} = \widehat{\Omega}_{(2\to 1)} \widehat{\Omega}_{(3\to 2)} \dots \widehat{\Omega}_{(P-1\to P-2)} \widehat{\Omega}_{(P\to P-1)}. \tag{5.27}$$

$\widehat{\Re}_{(p-1\to p)}$ is the transfer matrix of wave propagation from $(p-1)$-th to p-th stack [Eq. (5.19)] and $\widehat{\Omega}_{(p\to p-1)}$ from p-th to $(p-1)$-th stack [Eq. (5.20)]. The elements of the matrices $\widehat{\Re}_{(p-1\to p)}$ and $\widehat{\Omega}_{(p\to p-1)}$ are defined in agreement with Eqs. (5.21) and (5.22), respectively, for $z = z_p$ interface. Eventually, Eqs. (5.24)-(5.25) provide scattering matrices solving the problem of multistack wave coupling [Eqs. (5.23)].

Before illustrating the accuracy of the developed approach, we would like to underline its main advantages and disadvantages. The approach is ideal for calculation of light propagation in extended structures with a relatively small number of multilayer segments; the increase in the number of segments results in additional memory use for each given segment and, correspondingly, minimizes the advantages of a wave-matching approach over finite-difference and finite-element schemes.

The developed technique provides an efficient solution to the problem of coupling between multilayer stacks with high index contrast (high optical mode density difference) by implementing a multilayer-dependent number of modes. However, our calculations show that

careful design of the spectrum of the open-waveguide modes is necessary when the coupling to and from the highly confined modes is calculated.

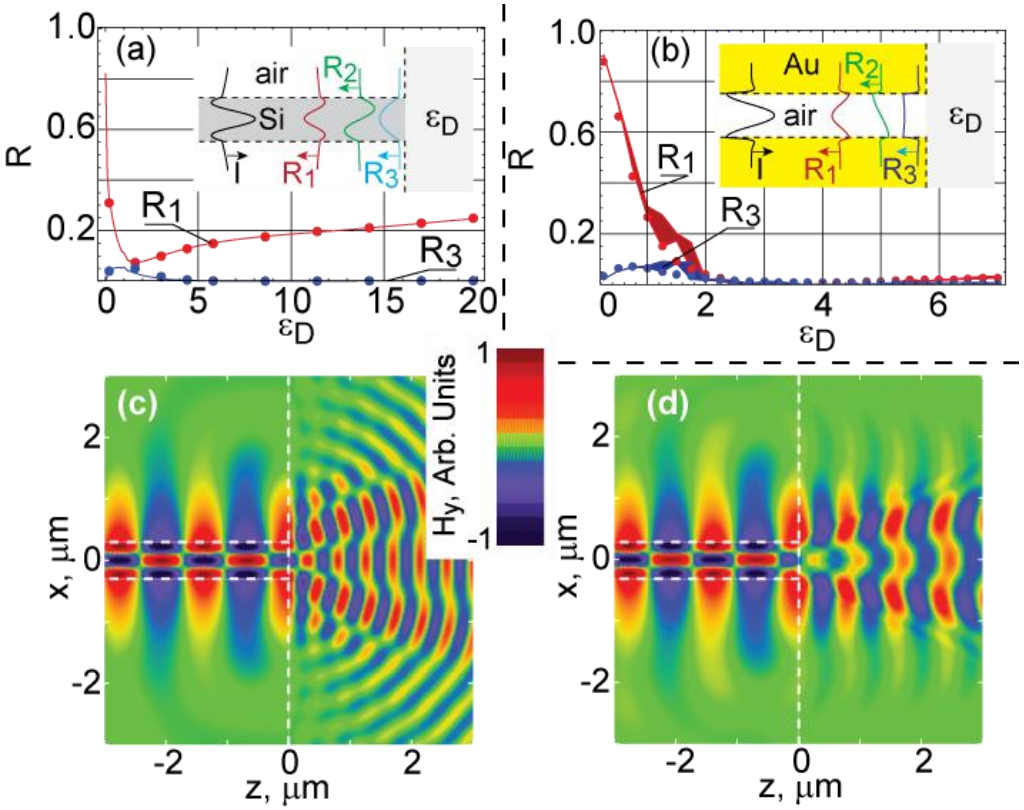

FIGURE 5.3: (a) Light reflection in the planar air-Si-air waveguide coupled to a homogeneous dielectric; $\lambda_0 = 1.5\,\mu m$, waveguide thickness $d = 0.6\,\mu m$; the geometry and profiles of the waveguide modes supported by the system are shown in the inset; excitation by TM_2 mode is assumed; the graph shows the comparison between the technique presented here (lines) and FEM simulations (dots); $R_2 = 0$ since the symmetry of TM_1 mode is different from that of TM_0 and TM_2 modes; (b) reflection in plasmonic gap (Au-air-Au) waveguide; $\lambda_0 = d = 0.6\,\mu m$; thickness of lines illustrates the convergence of the computations; panels (c) and (d) illustrate the field distributions in the system (a) with $\varepsilon_D = 12.12$ (c) and $\varepsilon_{D,x} = 3.6 + 0.05i$, $\varepsilon_{D,yz} = -12.2 + 1.36i$ (d); reprinted with permission from Ref. [137].

For guided modes, the approach allows straightforward calculation of intermode cross-talk by calculating the mode-specific pointing-flux and multiplying it by the amplitude of the given mode squared:

$$S_z^{(m)^{\pm}} \propto \left|A^{(m)^{\pm}}\right|^2 \mathbb{R}\mathrm{e} \int_{-\infty}^{\infty} \mathbb{E}^{(\mathrm{m})} \mathbb{H}^{(\mathrm{m})^*} dx \,. \tag{5.28}$$

Similarly, the approach allows for easy calculation of emission directionality, naturally separating the fields produced by guided modes from the fields of open-waveguide modes and separating the fields of the incident waves from the fields of the scattered waves.

5.5 Interguide Coupling in Plasmonic and Metamaterial Systems

We now illustrate the accuracy of the presented approach on several examples of plasmonic and metamaterial systems.

5.5.1 Light Emission and Scattering by Single-Mode Waveguide

We first consider light coupling to and from a waveguide. As an example, we use a $600\text{-}nm$ -thick Si waveguide surrounded by air, and calculate the coupling between this system and a homogeneous dielectric at $\lambda_0 = 1.5\ \mu m$; $\varepsilon_{Si} = 12.12$ [149] [Fig. 5.3(c)].

To analyze the accuracy of our technique we assume that the system is excited by the TM_2 (symmetric) mode with an amplitude of 1, and study the percentage of the reflected light into TM_0, TM_1, and TM_2 modes as a function of dielectric permittivity of the homogeneous dielectric [see inset in Fig. 5.3(a)]. For comparison, we calculate the same parameters with commercial finite-element-method (FEM) software [204]. The perfect agreement between the results of our technique and FEM simulations is shown in Fig. 5.3(a). As expected, even for

this relatively simple system, the scattering-matrix approach uses orders-of-magnitude less memory than the FEM model (~1.5 Gb for mode matching vs. ~8 Gb for FEM).

The field matching obtained with our technique for $\varepsilon_D = 12.12$ is illustrated in Fig. 5.3(c). Panel (d) of the same figure illustrates the matching obtained in coupling between an air-Si-air guide and an anisotropic hyperbolic metamaterial with $\varepsilon_{D,x} = 3.6 + 0.05i$, $\varepsilon_{D,yz} = -12.2 + 1.36i$ [41].

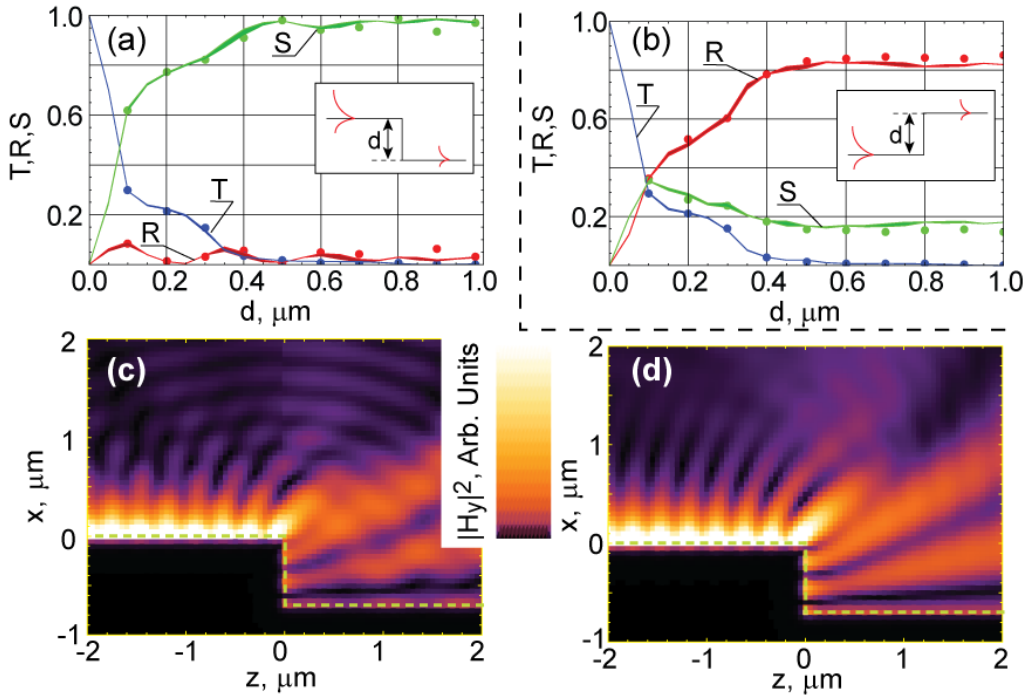

FIGURE 5.4: Scattering of the SPP propagating across the Au-air step; panels (a) and (b) show transmission, reflection, and scattering ($S = 1 - R - T$) of an SPP that is incident on the step; geometry of the structures is shown in insets; curves correspond to the formalism developed in this work (curve thickness represents data variation due to changes in spectra of bulk modes); dots represent results from FEM simulations; panels (c) and (d) illustrate the field distribution obtained from scattering matrix (c) and FEM (d) simulations for $d = 0.7\ \mu m$; reprinted with permission from Ref. [137].

5.5.2 Light Scattering in Plasmonic Systems

To further analyze the accuracy and limitations of the developed field-matching technique, we calculate the scattering from the plasmonic analog of the Si guide presented above: a $600\text{-}nm$-thick plasmonic gap waveguide operating at $\lambda_0 = 0.6\,\mu m$. We assume that cladding of this guide is composed from two gold plates with $\varepsilon_{Au} = -8.94 + 1.32i$ [149]. The agreement between the mode matching and FEM calculations of modal reflectivity in plasmonic gap guides is shown in Fig. 5.3(b).

We have further simulated the propagation of plasmonic modes across surface structure defects. In particular, we have used our approach to simulate the SPP propagation in "plasmonic step" geometry [Fig. 5.4]. As expected, when the incoming SPP is travelling on the upper side of the plasmonic step, most of the incident energy is converted into free-space modes. In contrast, when the incident SPP is travelling on the lower side of the step, the majority of energy is converted into the reflected SPP wave.

Our numerical simulations demonstrate that at near-IR frequencies (when $|\varepsilon_m| \gg \varepsilon_D$), the scattered field can be successfully decomposed into "top" open waveguide modes, as suggested in Ref. [212]. However, in the proximity of SPP resonance ($\varepsilon_m \cong -\varepsilon_D$), the inclusion of the "bottom" modes is necessary to adequately describe the optical properties of the system.

Note that the results of wave-matching simulations are almost identical to those obtained with FEM. Once again, we underline that the wave-matching technique allows for calculation of light propagation in much larger systems than the FEM system does.

To assess the convergence of our method, we have performed a set of simulations for each SPP structure described above, varying the configuration of spectra of top and bottom modes (for simplicity, equidistant k_x spectra between 500 and 3000 modes were used for Riemann numerical integration [214]). As expected, our simulations showed that it is necessary to design the spectrum of bulk modes to adequately resolve the SPP propagating at the $z = 0$ interface. Interestingly, the "averaged" parameters (such as amplitudes of reflected guided modes) are much more sensitive to spectrum variations than the matching of the boundary conditions at $z = 0$ interface, which is often considered to be an indication of accuracy of a numerical method. The typical inter-set variation of reflection, transmission, and scattering are illustrated in Figs. 5.3 and 5.4. The latter figure also shows the agreement between the field distribution obtained with our generalized scattering-matrix formalism and with FEM.

5.5.3 Truly Planar Optics

We now apply the developed wave-matching approach to analyze intermode coupling and out-of-mode scattering in planar optics [136, 212, 215]. Planar optics, in general (and SPP optics in particular), are fundamentally different from their free-space counterparts. Thus, when a plane wave is incident on a planar interface, the scattered field can be decomposed into one reflected plane wave and one transmitted plane wave. In contrast to this behavior, when one guided mode is incident on a planar interface between two waveguides, it generates a continuum of open-waveguide modes in addition to the sets of reflected and transmitted guided waves.

As seen from Figs. 5.5 and 5.6 and from Ref. [212], the typical interface between waveguide systems leads to the scattering of about 20% of incident radiation. Every attempt

to change the effective index of the mode in planar structures is necessarily accompanied by modal cross-talk or by out-of-plane scattering of radiation.

It is possible, however, to utilize anisotropic metamaterials to completely eliminate the cross-talk and to map the familiar laws of 3D optics to optics of planar guides [136, 216]. The main idea of planar optics lies in the ability to guide light along the planar optical circuit without out-of-plane scattering or modal cross-talk. Here we assume that the layers on both sides of the interface are aligned with each other ($x_{L,j} = x_{R,j}$).

In order to realize the efficient control over pulse propagation in the plane, the two layered structures must (i) have the same number of guided modes, and (ii) provide the ability to independently control the index of the mode (crucial for steering the light) and modal profile (crucial for optimizing the overlap integrals involved in $\widehat{\mathfrak{E}}$ and $\widehat{\mathfrak{H}}$ matrices).

As shown in Ref. [136] on the example of surface waves, these conditions can be satisfied when

$$\varepsilon_{L,yz;j} = \varepsilon_{R,yz;j}\,, \tag{5.29}$$

$$n^2\varepsilon_{L,x;j} = \varepsilon_{R,x;j}\,, \tag{5.30}$$

with n being the constant number that does not depend on layer number j.

As can be explicitly verified, when Eqs. (5.29) and (5.30) are satisfied, all $\widehat{\mathfrak{E}}$ and $\widehat{\mathfrak{H}}$ matrices become diagonal. Thus, the intermode coupling is absent across the interface. The interface remains completely transparent to TE-polarized waves, while reflection and refraction of TM-polarized modes are controlled by the ratio of out-of-plane permittivities. The direction and amplitudes of the reflected and refracted modes are related to the direction and amplitude of incident modes via the following Snell's law,

$$\sin(\theta_i) = \sin(\theta_r) = n\sin(\theta_t) \tag{5.31}$$

and Fresnel coefficients,

$$\frac{A_L^{(m)^-}}{A_L^{(m)^+}} = \frac{k_{L_z}^{(m)} - k_{R_z}^{(m)}}{k_{L_z}^{(m)} + k_{R_z}^{(m)}}, \tag{5.32}$$

$$\frac{A_R^{(m)^+}}{A_L^{(m)^+}} = \frac{2\,k_{L_z}^{(m)}}{k_{L_z}^{(m)} + k_{R_z}^{(m)}}. \tag{5.33}$$

The above equations represent generalization of the formalism of Ref. [136] to multilayered guides.

The concept of truly 2D optics is illustrated in Fig. 5.5 on example of an air-Si-air system coupled to a metamaterials waveguide. As expected, reflection of a single mode in a conventional planar system is accompanied not only by significant radiation scattering and modal cross-talk but also by cross-polarization coupling [Fig. 5.5(c)]. In contrast, for metamaterial guides the single-incident mode excites one reflected wave and one transmitted wave [Fig. 5.5(d)].

An interesting extension of truly planar optics is possible in plasmonic systems. From the fabricational standpoint, it is highly desirable that the plasmonic circuit is fabricated on top of common metallic substrate. Fabrication of an extremely low-scattering plasmonic circuit is possible when using anisotropic dielectrics deposited on noble metals in the limit of visible and near-IR frequencies, where the permittivity of metal is much larger than the permittivity of the dielectric ($|\varepsilon_m| \gg \varepsilon_{D,x}, \varepsilon_{D,yz}$).

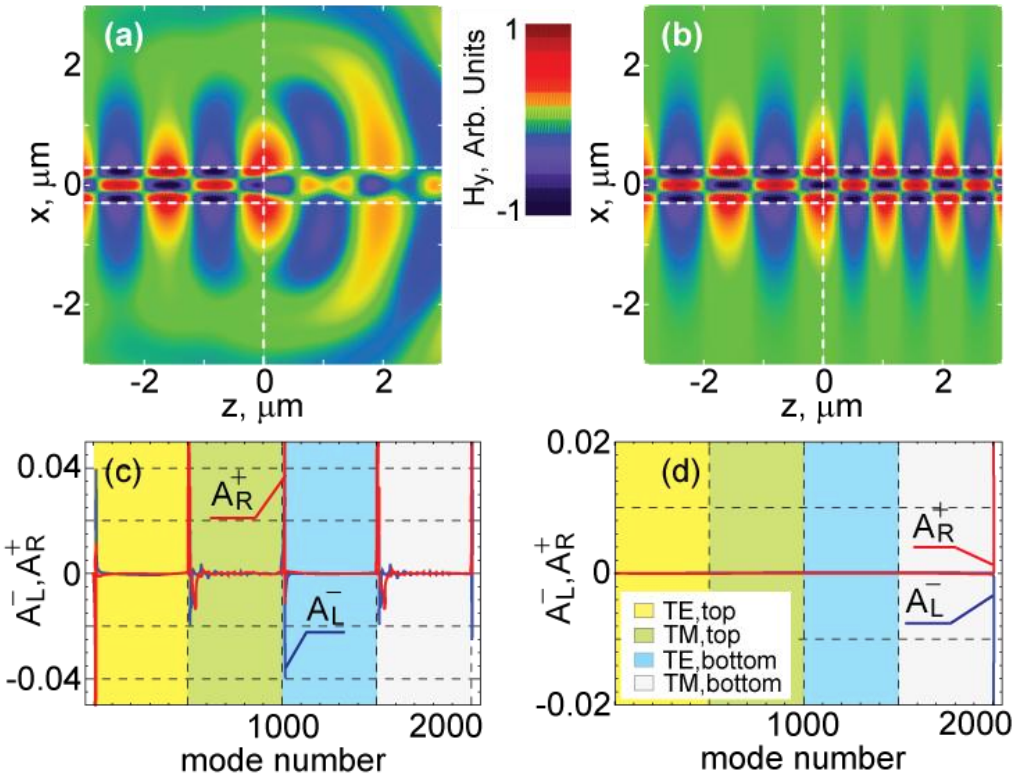

FIGURE 5.5: (a, c) An interface between an air-Si-air waveguide and isotropic air-($\varepsilon = 6.06$)-air guide leads to substantial modal cross-talk, polarization mixing, and out-of-plane scattering; while the interface between air-Si-air waveguide and its anisotropic truly planar optics analog allows for ideal mode matching with light steering capabilities (b, d); guided modes in (c, d) correspond to mode number > 2000; the system is excited by a TM_2 guided mode propagating at the angle 30° to the $z = 0$ interface; the amplitudes of modes in panels (c, d) are normalized to the amplitude of the incident mode; reprinted with permission from Ref. [137].

Consider the situation where the in-plane (yz) component of the dielectric's permittivity is kept constant across a plasmonic system, and only the out-of-plane (x) permittivity component of the superstrate is varied. In such a system, the propagation constant of a plasmonic mode, is approximately given by [216]

$$k_y^2 + k_z^2 \backsimeq \varepsilon_{D,x}\left(1 + \frac{\varepsilon_{D,yz}}{|\varepsilon_m|}\right)\frac{\omega^2}{c^2}, \tag{5.34}$$

and can be effectively controlled by changing the parameter $\varepsilon_{D,x}$. In the same limit, the exponential decay of the mode into the dielectric $\left[E,H \propto exp(-\kappa_D x),\ \kappa_D \backsimeq \omega/c\sqrt{\varepsilon_{D,yz}^2/|\varepsilon_m|}\right]$ does not depend on its propagation constant. The only source of out-of-plane scattering in such a structure is related to a weak dependence of the field profile in metal $\left[E,H \propto exp(\kappa_m x),\ \kappa_m \backsimeq \omega/c\sqrt{|\varepsilon_m|\left(1-\varepsilon_{D,x}/|\varepsilon_m|\right)}\right]$ on $\varepsilon_{D,x}$.

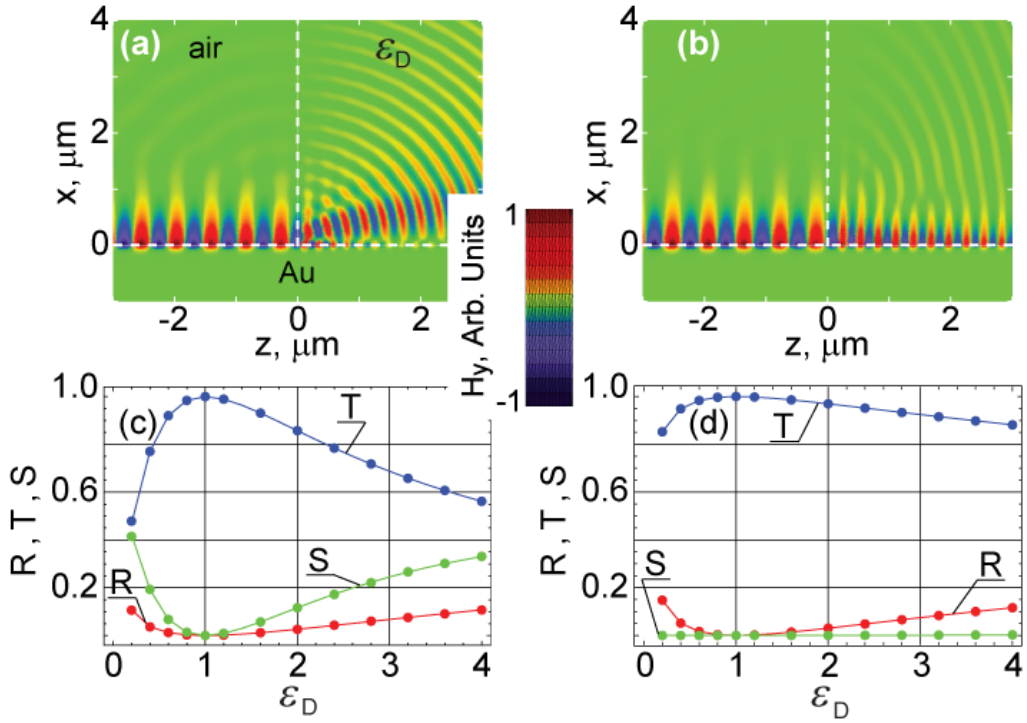

FIGURE 5.6: Anisotropic coatings (b, d) can significantly reduce (and almost eliminate) the scattering losses in plasmonic circuits; the figure shows reflection, transmission, and scattering in conventional plasmonic circuit (c) and in a plasmonic system where the space $x > 0$, $z > 0$ filled with material $\varepsilon_{yz} = 1$, $\varepsilon_x = \varepsilon_D$ (d); field distribution for $\varepsilon_D = 4$ (a) clearly shows that only a fraction of the energy of incident SPP is transferred into SPP on the right-hand side of the interface; on the other hand, the interface between the anisotropic system with $\varepsilon_{yz} = 1$, $\varepsilon_x = 4$ (b) allows for substantial modulation of SPP index, and results in almost perfect SPP-SPP coupling across a $z = 0$ interface; reprinted with permission from Ref. [137].

As seen from Fig. 5.6, anisotropy in the dielectric constant of a superstrate is achievable, for example, using the electrooptic effect [216], providing orders-of-magnitude suppression of out-of-plane scattering in plasmonic systems with respect to their isotropic counterparts.

5.6 Conclusion

We developed a reliable wave-matching technique for calculation of light propagation in planar guides and in arrays of planar guides. The technique combines full spectrum of three groups of modes: top, bottom, and guided, and finds solutions that satisfy boundary conditions at the interfaces of the multilayered stacks. We illustrated the developed formalism on examples of photonic, metamaterial, and plasmonic guides, and presented an approach to utilize anisotropic metamaterials for the minimization and elimination of modal cross-talk in planar optical circuits. Mode-matching computations showed substantial reduction of memory usage ($\sim 1.5\ Gb$ for our mode matching vs. $\sim 8\ Gb$ for FEM).

Chapter 6 - Plasmonic Beaming: Modeling Beam Formation

6.1 Introduction

It has been known that light emerging from a subwavelength aperture is diffracted in the form of cylindrical (circular) waves [116, 217]. However, it was recently shown that a single subwavelength aperture, surrounded by a set of periodic grooves on the output side, emits highly-directional beams of light under TM-polarized illumination [98, 103, 107]. This directional beaming was observed in experiments using optical [218, 219], mid-IR [112, 113], and microwave [220-223] radiation. Several theoretical explanations supporting the directionality of the emission have been published, including methods of Huygens's principle and surface cavity resonance [108-110], of multiple scattering effects of surface plasmon polaritons (SPPs) [111], and of field expansion from impedance boundary matching [114]. Since then, various aspects of beaming structures have been studied; for example, multiple direction beaming [224], a nonuniform and nonperiodic set of grooves [225], off-axis directional beaming [226, 227], grooves in curved depths [228], dielectric surface gratings [218], and beam focusing through a tapered subwavelength aperture [229]. Note that most of the previous studies are related to deforming configurations or optical properties of the grooves. Recently, two groups of researchers numerically observed focusing phenomena of beaming structure [230, 231], and dependences on number of grooves and period were studied. However, there was no analytical theory to explain the focusing behavior.

In numerical studies of the beaming phenomena, finite-element (FEM) and finite-difference time-domain (FDTD) methods are useful numerical approaches to compute light in beaming structures. However, the substantial limitation of the techniques is that the area of computation is restricted to only small geometries ($\leq 10\lambda_0$). In experimental studies, field

intensity distribution is always measured in the extreme far field, a region where FEM and FDTD cannot access. Consequently, in order to verify the experimental results by these numerical methods, we need a numerical approach to extend the numerical FEM or FDTD fields to the extreme far field.

In this work [113], we provide a numerical technique to extend electromagnetic fields computed by a commercial FEM software [204] into the far-field regime, and also propose a model to predict focal spots and beaming directions.

The rest of this Chapter is organized as follows. Generalization of the beaming-steering structure and our plasmonic mid-IR beaming device will be briefly described in Section 2. The experimental results from our UMass collaborators and applications will be mentioned. This Section will give the motivation to the rest of this work. In Section 3, we will propose a technique to extend the field distribution in the limited space from the FEM simulations. Full description of our model for beaming directions and array of focal spots will be shown in Section 4. We will verify our field expansion technique and our model with experimental results, FEM simulations, and field calculation in Section 5. All of them show very good agreement.

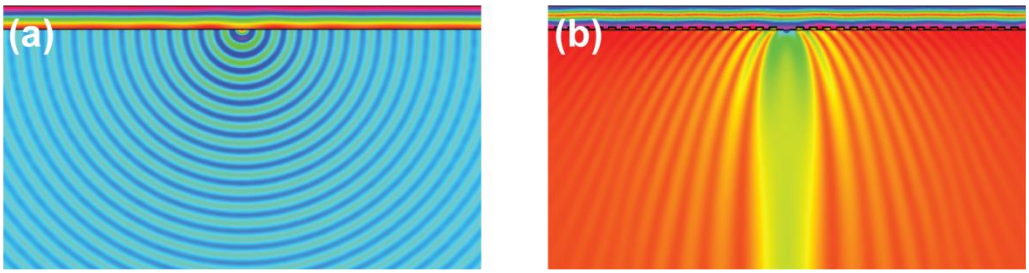

FIGURE 6.1: Diffraction of TM-polarized incident fields by (a) a subwavelength single slit and (b) a subwavelength single slit flanked by a set of periodic grooves; (a) waves diffracted in all directions and have circular (cylindrical) wavefront form; (b) transmitted fields concentrate in specific directions, giving highly-directional beams.

6.2 Mid-Infrared Beam Steering Structure

As mentioned earlier, a subwavelength single slit diffracts an incident plane wave in all directions [Fig. 6.1(a)]. In contrast, an aperture, flanked by a set of periodic grooves on the output side with TM-polarized illumination, can confine the diffracted wave into directions that depends on the incident wavelength, optical properties of metallic film, substrate, and superstrate, and period of the grooves [Fig. 6.1(b)]. This directional emission is created by the interference of scattering waves due to SPPs propagating through a corrugated structure [98, 102, 107-111]. In this Section, we review the mid-IR beaming experiments that our UMass collaborators performed [112]. The discrepancy between the experimental and preliminary numerical FEM results leads to the motivation through the rest of this Chapter.

The schematic of the beam-steering device is shown in Fig. 6.2(a). The $2N_g$ grooves are deposited on GaAs substrate of thickness L with unpolished surface, and then gold layer is coated on top of the grooves. The TM-polarized field with wavelength λ_0 is illuminated on top of the gold layer in the air. The transmitted waves are collected as a function of angle θ respective to normal axis in the very far-field air behind GaAs [see the experimental setup in Fig. 6.2(b)]. Note that the GaAs substrate provides the benefit of both carrier concentration and thermal tunabilities of beaming [112, 232-235]. Geometrical and optical parameters are given by the following: number of grooves $N_g = 100$, groove period $\Lambda = 2.8\,\mu m$, groove depth $h = 0.5\,\mu m$, groove and slit width $a = 1.4\,\mu m$, gold layer thickness $d = 200\,nm$, GaAs thickness $L = 650\,\mu m$, and permittivity of GaAs substrate $\varepsilon_{GaAs} \cong 10.87$ at room temperature (23℃) [233] (permittivity is a wavelength-dependent quantity; however, for simplicity we use it of $10\,\mu m$-wavelength). Two pulse tunable quantum cascade lasers

(QCLs) with wavelength λ_0 ranges of $8.3 - 9.4\,\mu m$ and $9.8 - 10.5\,\mu m$ are used as the incident radiation sources.

Directional beaming is clearly seen in experiments at room temperature [Fig. 6.3] where the gap in the experimental data represents the portion of the spectrum not accessible with QCLs. The normal beaming wavelength (a wavelength which the beaming direction is normal to the GaAs/Au interface) is found at approximately $9.2\,\mu m$. The transmitted beams split into two, and steering angles increase while the incident wavelength is tuned away from the normal beaming wavelength. The dashed lines come from our theoretical model (as will be proposed in Section 6.4). The asymmetric intensity of the split beams likely emerges from the slight misalignment of the single aperture respected to the grooves.

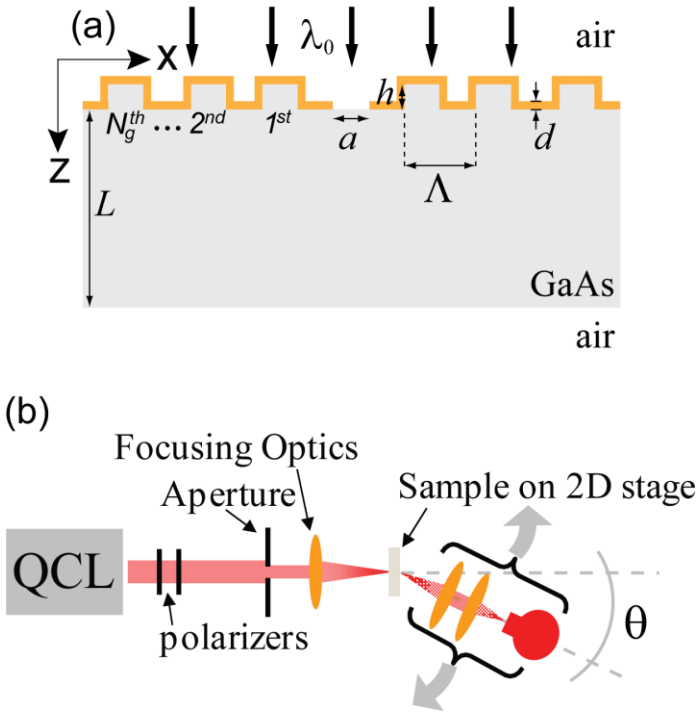

FIGURE 6.2: (a) Schematic of our mid-IR plasmonic beaming structure used in experiments; $N_g = 100,\ \Lambda = 2.8\,\mu m,\ h = 0.5\,\mu m,\ a = 1.4\,\mu m,\ d = 200\,nm,$ and $L = 650\,\mu m$; (b) the experimental setup for determination of the angle-resolved transmission of beamed light; field intensity is collected for different angles θ; reprinted with permission from Ref. [112].

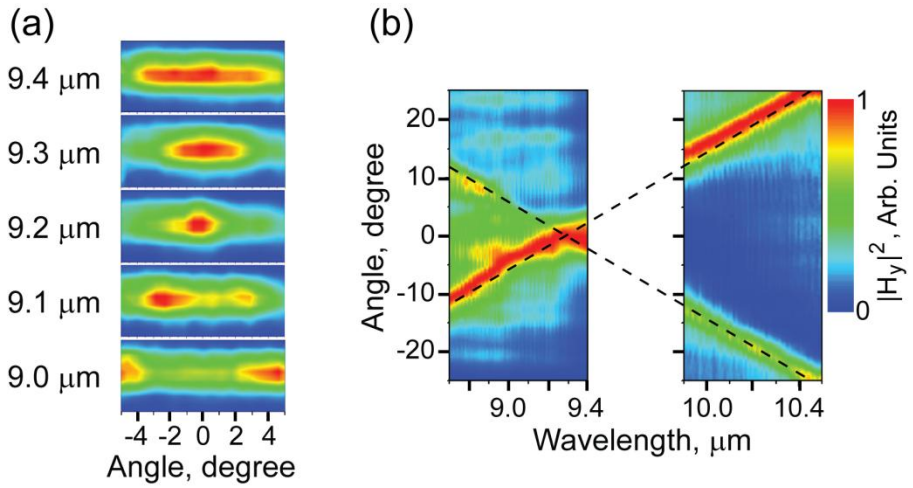

FIGURE 6.3: (a) Two-dimensional profiles of transmitted beams for five wavelengths between 9.4 and 9.0 μm; the narrowest beam width is seen for a laser wavelength of 9.2 μm (normal beaming wavelength); (b) the experimental (contour plot) and predicted (dashed lines) angular distribution of the transmitted beam as a function of wavelength; the gap in the experimental data represents the portion of the spectrum not accessible with our lasers; the dashed lines are computed from Eq. (6.14); the computed normal beaming wavelength is found at wavelength 9.25 μm; reprinted with permission from Ref. [112].

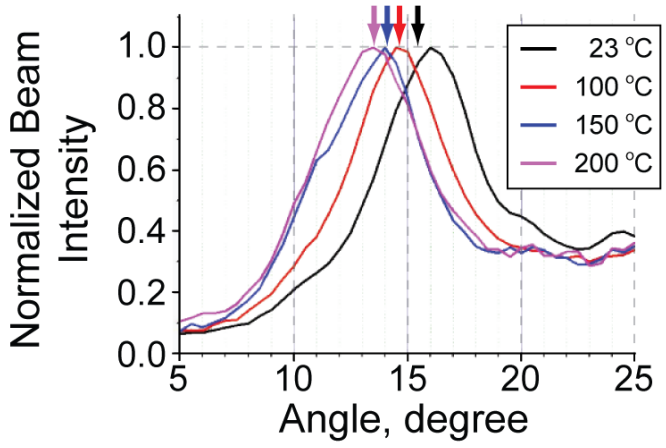

FIGURE 6.4: Normalized beam intensity vs. steering angle for a laser wavelength of 10 μm as a function of temperature; device temperature is increased from 23 to 200℃; the highest peak in each curve represents beaming direction; computed beaming direction for each temperature is shown in arrow; reprinted with permission from Ref. [112].

The beaming directions can be tuned by changing optical properties of the steering materials. In Ref. [112], our UMass collaborators control the permittivity of GaAs by increasing the temperature inside the substrate from room temperature to 200℃ [see Table 6.1]. For incident light at a laser wavelength of $10\ \mu m$, the total shift in the steering angle of the transmitted beams is found to be approximately 3° [Fig. 6.4].

TABLE 6.1: Dependence of permittivity of GaAs on temperature [232, 233].

Temperature (℃)	Permittivity of GaAs
23	10.87
100	10.95
150	11.00
200	11.05

We verified the experimental results by modeling our beam-steering device with commercial FEM software [204]. The transmitted beams are measured at the GaAs/air interface where Snell's law is also applied in order to compare to realistic refracting behavior. However, in contrast to the previously reported works [108], our simulation-designed pattern (with $L = 200\ \mu m$) does not represent the experimentally observed pattern (with $L = 650\ \mu m$) [see Fig. 6.5(a) compared to Fig. 6.3(b)]. Moreover, we observe the dependence of normal beaming wavelength on the thickness of GaAs substrate [Fig. 6.5(b)]. Surprisingly, in experiments with extremely far-field measurements, we do not see any dependence of beaming directions on the substrate thickness. Note that due to the limited memory unit of our computing resource, we cannot simulate samples where $L \geq 500\ \mu m$ with a fixed mesh size.

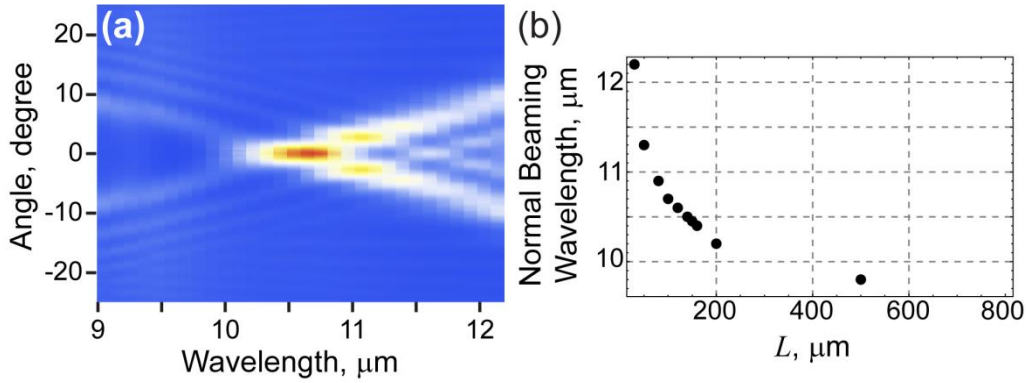

FIGURE 6.5: (a) Angular distribution of the transmitted beam as a function of wavelength from FEM simulations for $L = 200\,\mu m$; normal beaming angle is found at $10.2\,\mu m$; (b) dependence of normal beaming wavelength, observed from FEM simulations, on GaAs thickness; field intensity is measured at GaAs/air interface.

The discrepancy between experimental and numerical results comes from the evolution of wave packet (beam formation) that still happens in "extreme" far field of the sources, which is not accessible with the FEM approach. Therefore, we (i) need a new technique allowing the extension of the FEM numerical solutions into the extreme far field, and (ii) need a quantitative description of beam formation. The latter is very crucial when beaming is used in on-chip devices where the distance from the aperture to the receiver is on the order of a few tens (hundreds) of wavelength. In Section 6.3 and Section 6.4, we will develop formulation to support these two goals [113].

6.3 Field Extension Technique for Finite Element Results

The FEM technique gives solutions of Maxwell's equations satisfying boundary conditions in every point in the space. On the other hand, the magnetic field, $H_y(x,z)$, of the TM-polarized wave could be represented as

$$H_y(x,z) = \sum_{m=1}^{M} a_m e^{ik_{x,m}x} e^{ik_{z,m}z} \tag{6.1}$$

where $k_z = \sqrt{\varepsilon_{GaAs}\omega^2/c^2 - k_x^2}$ and in the distance very far from the source, k_x occupies only the propagating regime, $k_x \in \left[-\sqrt{\varepsilon_{GaAs}}\omega/c\,, +\sqrt{\varepsilon_{GaAs}}\omega/c\right]$. The summation over m represents nodes in numerical integration techniques [203]. a_m corresponds to the weighted complex coefficient for each wavevector component $k_{x,m}$, which is not given by the FEM approach; therefore, we need a reliable method to extract the spectrum a_m with the given FEM data. Eventually, we can compute the extreme far-field $H_y(x,z)$ using Eq. (6.1).

Here the problem of the spectrum definition can be considered as the linear least-squares fitting problem [205]. Assuming that the FEM software gives us the measured y-component magnetic fields h_n of N data points: $(x_1, z_1, h_1), (x_2, z_2, h_2), \dots, (x_N, z_N, h_N)$, the problem of the fitting technique is to minimize the field deviation:

$$F(\vec{a}) = \sum_{n=1}^{N} |h_n - H_n|^2 \tag{6.2}$$

where $H_n = H_y(x_n, z_n)$ is given by Eq. (6.1). The minimum occurs when $\partial F/\partial a_m = 0$; consequently, the amplitudes of modes $\vec{a}$ are obtained as

$$\hat{A}\vec{a} + \vec{b} = \vec{0} \tag{6.3}$$

where

$$\vec{a} \doteq \begin{bmatrix} a'_1 \\ \vdots \\ a'_M \\ a''_1 \\ \vdots \\ a''_M \end{bmatrix}, \tag{6.4}$$

$$\vec{b} \doteq \begin{bmatrix} (b_1)_1 \\ \vdots \\ (b_1)_M \\ (b_2)_1 \\ \vdots \\ (b_2)_M \end{bmatrix}, \tag{6.5}$$

$$\hat{A} \doteq \begin{bmatrix} (A_{11})_{11} & \cdots & (A_{11})_{1M} & (A_{12})_{11} & \cdots & (A_{12})_{1M} \\ \vdots & \ddots & \vdots & \vdots & \ddots & \vdots \\ (A_{11})_{M1} & \cdots & (A_{11})_{MM} & (A_{12})_{M1} & \cdots & (A_{12})_{MM} \\ (A_{21})_{11} & \cdots & (A_{21})_{1M} & (A_{22})_{11} & \cdots & (A_{22})_{1M} \\ \vdots & \ddots & \vdots & \vdots & \ddots & \vdots \\ (A_{21})_{M1} & \cdots & (A_{21})_{MM} & (A_{22})_{M1} & \cdots & (A_{22})_{MM} \end{bmatrix}, \tag{6.6}$$

$$\begin{cases} (b_1)_m = \sum_{n=1}^{N} h'_n(-2C_{mn}) + h''_n(-2S_{mn}) \\ (b_2)_m = \sum_{n=1}^{N} h'_n(2S_{mn}) + h''_n(-2C_{mn}) \end{cases}, \tag{6.7}$$

$$\begin{cases} (A_{11})_{ml} = \sum_{n=1}^{N} 2C_{mn}C_{ln} + 2S_{mn}S_{ln} \\ (A_{12})_{ml} = \sum_{n=1}^{N} -2C_{mn}S_{ln} + 2S_{mn}C_{ln} \\ (A_{21})_{ml} = \sum_{n=1}^{N} -2C_{ln}S_{mn} + 2C_{mn}S_{ln} \\ (A_{22})_{ml} = \sum_{n=1}^{N} 2S_{mn}S_{ln} + 2C_{mn}C_{ln} \end{cases}, \tag{6.8}$$

$$\begin{cases} C_{mn} = \mathbb{R}\mathrm{e}\left[\exp\left(i(k_{x,m}x_n + k_{z,m}z_n)\right)\right] \\ S_{mn} = \mathbb{I}\mathrm{m}\left[\exp\left(i(k_{x,m}x_n + k_{z,m}z_n)\right)\right] \end{cases}. \tag{6.9}$$

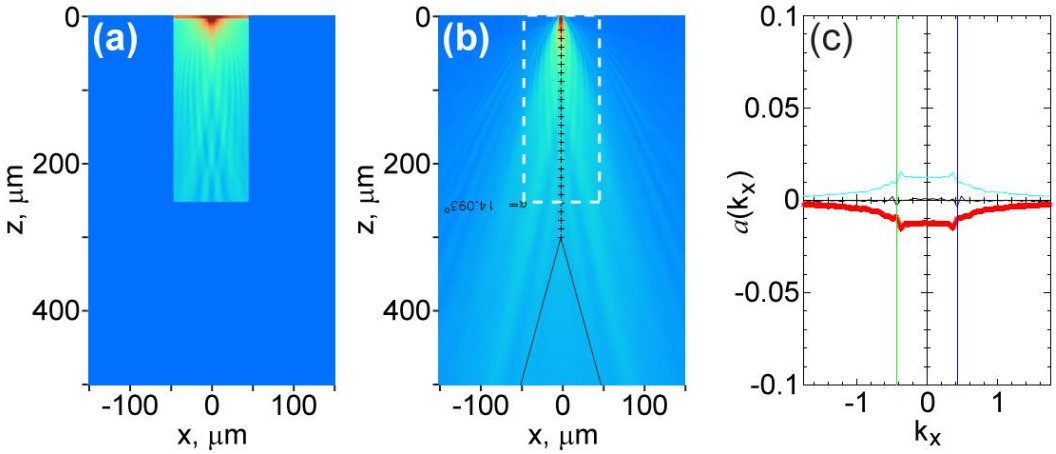

FIGURE 6.6: Field extension technique for FEM results; (a) field distribution from the FEM simulation is shown in small rectangle; (b) extension of the FEM fields; the dashed rectangle shows the original region; (c) retrieved spectrum components $a(k_x)$; red, black, and pink curves represent real part, imaginary part, and absolute value of the components, respectively; two lines correspond to highest peaks in spectrum, computed by Eq. (6.13).

Fig. 6.6 shows the extension of the field at $L = 250\mu m$ for $\lambda_0 = 11.5\,\mu m$. The fitting coefficients are shown in Fig. 6.6(c). The directions of the beams correspond to k_x of the dominant peaks; the lines, specifying the peaks, are given by Eq. (6.13). Note that in Eq. (6.1), the wavevectors of SPPs are neglected [92, 93] $\left(\left|k_{x,SPP} = \sqrt{\varepsilon_{Au}\varepsilon_{GaAs}/(\varepsilon_{Au} + \varepsilon_{GaAs})}\omega/c\right| > \sqrt{\varepsilon_{GaAs}}\omega/c\right)$; therefore, near the GaAs/Au interface we cannot see the SPP scattering in Fig. 6.6(b). Omitting SPPs will not affect field distribution in very far field because here plasmonic mid-IR SPPs are only significant in the range of $z \cong 1/\mathbb{I}\mathrm{m}\left(k_{z,SPP}\right) \approx 10\mu m$.

6.4 Focusing and Beam Formation

Even though it has been almost a decade after the first discovery of beaming phenomenon [107], up until now there has been no theory that can clearly and completely describe the underlying physical mechanism of the formation of the beams. In this Section, we develop the

formalism to compute the transmitted fields in the real space, and describe the focusing property of scattering waves from each groove (scatter) and its neighbor. In addition, our model is substantially different from conventional understanding in the case that *the beams emerge from the focal points, not the aperture*. Consequently, the numerical measurements of beaming directions from FEM simulations must be careful.

6.4.1 Field Computation

In the beam steering device, SPPs excited by a subwavelength aperture, propagate away from the slit along the metal-dielectric interface. The periodic surface corrugation results in partial out-coupling of SPPs into free-space. As a result, the light emitted by the device represents the interference of the cylindrical wave emitted by the central hole and the portion of original SPP scattered by periodic surface corrugations. Since the emission of the central hole lacks directionality, the direction of the beams is determined solely by interference of SPP-scattered waves.

Therefore, the field behind the corrugated surface, combining SPPs and scattered waves is described as

$$H_y(x,z) = \int_{-\infty}^{+\infty} dk_x \sum_{j=-N_g}^{N_g} S_j(k_x)\, t_j\, e^{ik_x(x-x_j)} e^{ik_z(k_x)z} \tag{6.10}$$

where the index j includes all scatterers in the beam-steering structure, $x_j = j\Lambda$ is the position of the j-th bump, and $S_j(k_x)$ describes scattering at $x = x_j$. For simplicity, we assume that the bumps are point scatterers, so $S_j(k_x) \approx 1$. t_j represents the amplitude and phase of single SPP at the j-th scatterer in which $t_j = t_1^{|j|}$ and $t_1 = t_0 \exp(i\, k_{x,SPP}\Lambda)$. Note that $t_0 \approx 0.9$,

computed by the FEM software, is the normalized amplitude of single SPP transmitting through a delta-function bump. Here we are interested only in problem of the far-field beaming; k_x is limited to the propagating spectrum, $|k_x| \le \sqrt{\varepsilon_{GaAs}}\omega/c$. Using geometric series, the far-field distribution is reduced as

$$H_y(x,z) = \int_{-\sqrt{\varepsilon_{GaAs}}\omega/c}^{+\sqrt{\varepsilon_{GaAs}}\omega/c} dk_x\, F(k_x) e^{ik_x x} e^{ik_z(k_x)z}\,, \tag{6.11}$$

$$F(k_x) = \frac{t_1 e^{-ik_x\Lambda}}{1 - t_1 e^{-ik_x\Lambda}}\left[1 - \left(t_1 e^{-ik_x\Lambda}\right)^{N_g}\right] + \frac{t_1 e^{ik_x\Lambda}}{1 - t_1 e^{ik_x\Lambda}}\left[1 - \left(t_1 e^{ik_x\Lambda}\right)^{N_g}\right]. \tag{6.12}$$

The function $F(k_x)$ can be used to calculate $a(k_x)$ in Eq. (6.1). Instead of the point scatterers, if the subwavelength single slit is surrounded by a set of periodic grooves with a finite width, then $a(k_x)$ is directly proportional to $S_j(k_x)F(k_x)$.

6.4.2 Beaming Directions

The beaming directions corresponding to the maximum interference of SPP-scattered waves are given by the resonance of the function $F(k_x)$ in Eq. (6.12); that is, select k_x where $dF(k_x)/dx = 0$. For an infinite number of bumps, the predicted directions are given by the SPP diffraction equation [92, 93]:

$$k_x = l\left(\frac{2\pi}{\Lambda}\right) - \frac{\delta}{\Lambda} - k'_{x,SPP} \tag{6.13}$$

or

$$\sin\alpha = l\left(\frac{\lambda_0}{\sqrt{\varepsilon_{GaAs}}\Lambda}\right) - \frac{\lambda_0}{\sqrt{\varepsilon_{GaAs}}\Lambda}\frac{\delta}{2\pi} - \frac{n'_{SPP}}{\sqrt{\varepsilon_{GaAs}}} \tag{6.14}$$

where n'_{SPP} is the real part of the refractive index of SPPs, α is the beaming angle which is measured with respect to the z-axis, and the parameter δ describes retardation of the phase of the SPP caused by an individual corrugation. $l \geq 1$ is an integer chosen to give pure real number α. For small wavelengths, Eqs. (6.13) and (6.14) supports many l modes; physically, it is possible to have multiple beaming directions. This phenomenon is studied seriously in Ref. [224].

The normal beaming wavelength corresponds to the normal beaming angle $\alpha = 0$, given $\lambda_0 = n'_{SPP}\Lambda$. In our plasmonic mid-IR beam-steering structure, the normal beaming wavelength is computed as $\sim 9.25\ \mu m$, which is very close to the experimental measurement [$\sim 9.2\ \mu m$ in Fig. 6.3].

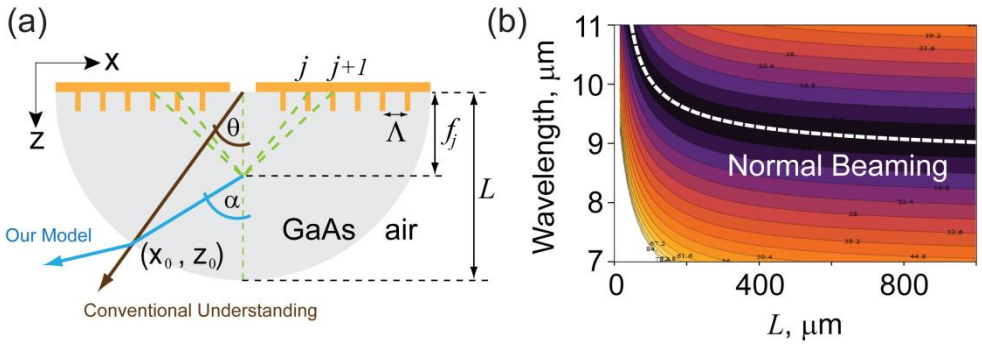

FIGURE 6.7: (a) Schematic of beam-steering structure used in our model; scattering light from delta-function scatterers j and $j+1$ will constructively interfere at a focal point f_j; our model's beams (blue line) emerge from the furthest focal spot f_{max} with directional angles α; however, in the conventional understanding the beams (brown line) emerge from the slit with directional angles θ; an observation point is marked as (x_0, y_0); (b) contour plot showing the apparent directions of the beam, θ, for different wavelengths and GaAs thicknesses; the simulations are computed in air upon exit from dielectric; normal beaming is marked as a white-dashed curve.

6.4.3 Focal Region and Beam Formation

We now come to the question of where the beams do emerge. It appears that the periodic corrugated surface generates array of relatively tight focal points [Fig. 6.7(a)]. Therefore, the beaming structure behaves as a Fresnel lens in the sense that phase difference of scattering light from the j-th scatterer and its neighbor $(j+1)$-th is 2π and then a focal point f_j is formed by constructive interference. Assuming that only bumps close to the slit are important for wave scattering $(f_j \gg x_j)$, the phase difference may be written as [Fig. 6.7(a)]

$$\left(k_{x,j+1}x_{j+1} + k_{z,j+1}f_j + k_{x,SPP}x_{j+1}\right) - \left(k_{x,j}x_j + k_{z,j}f_j + k_{x,SPP}x_j\right) = 2\pi\,, \tag{6.15}$$

$$k_{x,j} \cong \sqrt{\varepsilon_{GaAs}}\frac{\omega}{c}\frac{x_j}{f_j}\left[1 - \frac{x_j^2}{2f_j^2}\right], \tag{6.16}$$

$$k_{z,j} \cong \sqrt{\varepsilon_{GaAs}}\frac{\omega}{c}\left[1 - \frac{x_j^2}{2f_j^2}\right]. \tag{6.17}$$

Eventually, the focal spot of a scatterer and its neighbor is given by

$$f_j \cong \frac{\sqrt{\varepsilon_{GaAs}}\Lambda^2(2j+1)}{2(\lambda_0 - n'_{SPP}\Lambda)}. \tag{6.18}$$

It is straightforward to obtain the focal spot equation without the restriction of $f_j \gg x_j$. The deviation of both equations is very small and negligible when the operating wavelengths are close to the normal beaming wavelength. Note that each focal point is originated from four scatterers (two on each side of the single slit). The focal spots corresponding to different j-values occupy the region between f_1 and f_{max}; each is separated by a constant distance $\sqrt{\varepsilon_{GaAs}}\Lambda^2/(\lambda_0 - n'_{SPP}\Lambda)$. The furthest focal spot f_{max} represents the cut-off number of bumps

where the intensity of the SPP is substantially reduced $\left[t_0^{j_{cut}} \sim 1/e\right]$. Thus, the array of focal spots would effectively cut-off when

$$j_{cut} \sim -\frac{1}{\ln t_0}. \tag{6.19}$$

The formation of the focal range is observed in the experiments [Fig. 6.8], simulations [Fig. 6.9], and in Ref. [230] in the visible spectrum. It appears that the beams emit from the furthest focal spot f_{max}, with the beaming directions (with angles α) given by Eq. (6.14).

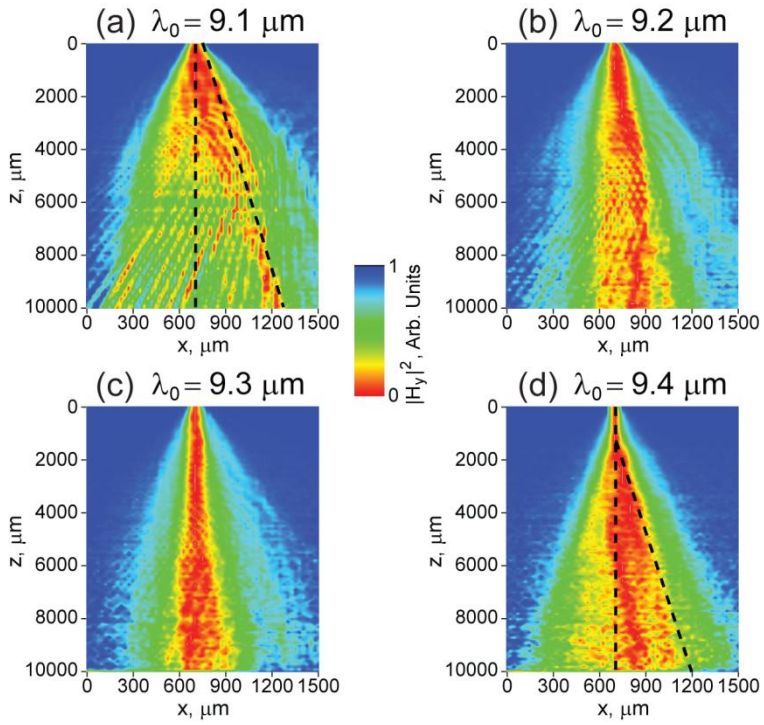

FIGURE 6.8: Intensity distribution in the experimental plasmonic beaming structure at wavelengths of (a) 9.1, (b) 9.2, (c) 9.3, and (d) 9.4 μm; normal beaming wavelength is between 9.2 and 9.3 μm; oblique dashed lines represent accuracy of our model [Eqs. (6.14) and (6.18)]; printed with permission from our UMass collaborators.

Therefore, our model contrasts to the conventional understanding that the beams emanate from the central slit itself with directions of angles θ [Fig. 6.7(a)]. Consequently, when using the finite-element method to deduce the field profile, one should be careful in numerically measuring the beaming angles. Both angles α and θ are related by

$$\theta = \arccos\frac{z_0}{L}, \tag{6.20}$$

$$z_0 = f_{max}\sin^2\alpha + \sqrt{L^2 - f_{max}^2\sin^2\alpha}\cos\alpha\,. \tag{6.21}$$

The excellent agreement between the experimental and predicted angular distribution of the transmitted beam as a function of wavelength is shown in Fig. 6.3(b). The dashed lines are computed by Eq. (6.20) and Snell's law. Moreover, the computed beaming angles of 10 μm-operating wavelength for room temperature, 100℃, 150℃, and 200℃ are 15.3, 14.58, 14.13, and 13.69 degrees, respectively [see arrows in Fig. 6.4].

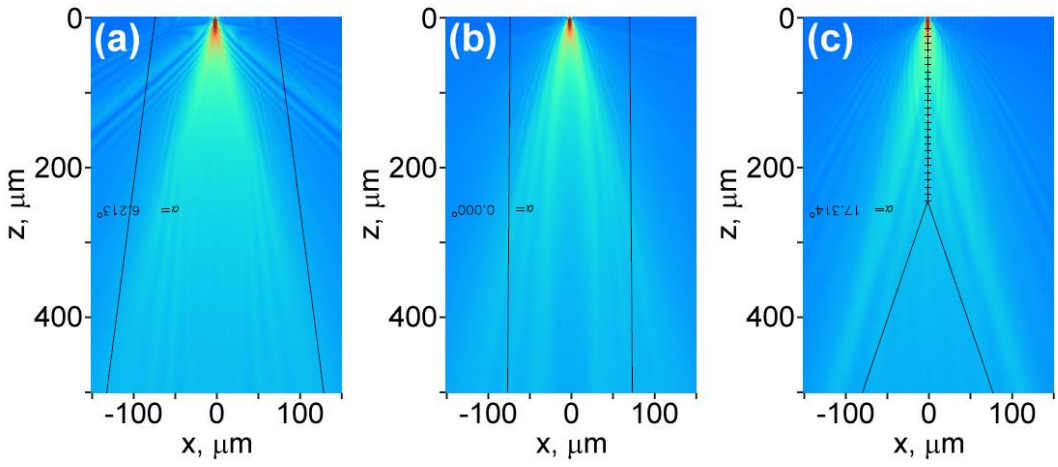

FIGURE 6.9: Field extension from the FEM simulations for wavelengths of (a) 8.25, (b) 9.25, and (c) 12 μm; the predicted beaming angles, shown as lines, are (a) 6.2, (b) 0, and (c) 17.3°; the cross symbols show the positions of focal spots.

As mentioned earlier, the wavepackets of scattering fields slowly evolve; therefore, in relatively close proximity to the plasmonic surface, beaming profile is related to the observation distance. Such slow field evolution is crucial when beaming is used in on-chip devices. We verify the field evolution by computing the beaming angles, calculated at the furthest-end interfaces of the GaAs slabs, for various wavelengths and slab thicknesses [Fig. 6.7(b)]. Obviously, for an arbitrary laser wavelength, the angle varies for small distances from the aperture (roughly $L = 0 - 200\ \mu m$), and approaches the beaming angle in the extreme far field ($L = 1000\ \mu m$).

6.5 Verification of Beam-Steering Model

In this Section, we will verify the robustness of our beam-steering model with different experimental and numerical simulation examples. All of them show excellent agreement with the proposed approach.

The experimental evidence of focal range in the far field, performed by the UML group, is shown in Fig. 6.8. The field intensity is measured behind the plasmonic mid-IR beaming structure for different distances up until $10000\ \mu m$. It is clearly seen that the normal beaming occurs for wavelengths between $9.2 - 9.3\ \mu m$. We verify the accuracy of the focusing range and beaming directions by Eqs. (6.18) and (6.14), respectively. In Fig. 6.8(d), the furthest focal spot is located around $1300\ \mu m$, and the computed result is located at $1224\ \mu m$. The oblique dashed line corresponds to computed $\alpha = 3.24°$ with respect to the z-axis. In Fig. 6.8(a), f_{max} is found at $-1369\ \mu m$, and $\alpha = 2.9°$; so that, the negative focal spot is virtual, and the beams appear to emanate from behind the corrugation surface.

We also use our field extension technique to decompose the spectrum components at a distance $z = 250\,\mu m$ and extend the measured fields into the far-field regime. The array of focal points and angle of beaming directions for each wavelength are computed and shown along with intensity distribution in Fig. 6.9; the model is in excellent agreement with FEM simulations.

It is regularly observed in a beam-steering device that the beams cross each other when the laser wavelength is increased [107-111]. We emphasize that the crossing behavior of the beams is the result of focal spots moving from virtual space (negative f_{max}) to the front of the corrugated structure (positive f_{max}). We use the field equation [Eq. (6.11)] to illustrate three field evolution patterns; negative, infinite, and positive f_{max} for wavelengths of 8.25, 9.25, and 10.25 μm, respectively [Fig. 6.10].

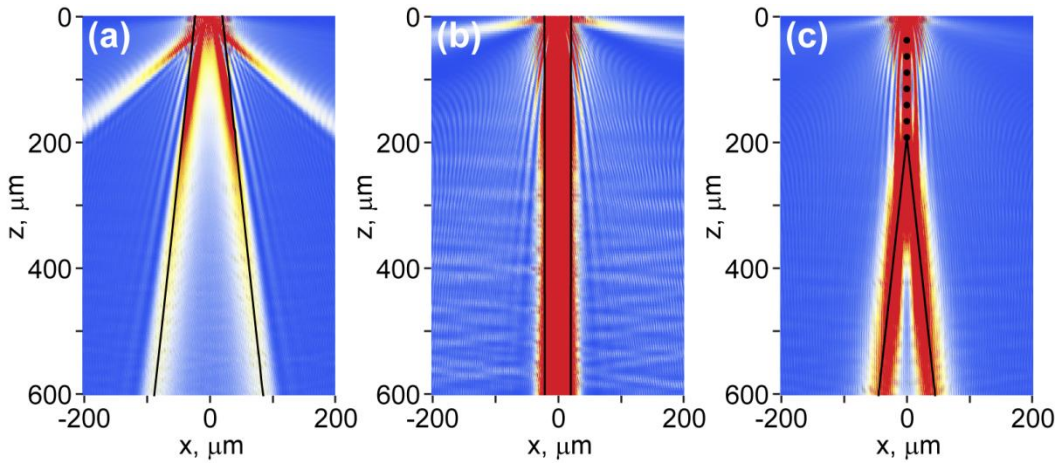

FIGURE 6.10: Calculated intensity distribution and angular identification (lines) of the transmission fields for the illumination wavelengths of (a) 8.25, (b) 9.25, and (c) 10.25 μm; (a)-(c) $f_{max} = -195$, 23143, and 192 μm, and $\alpha = 6.2$, 0.05, and 6.27°, respectively; array of focal spots is shown as dots in (c); three beaming patterns are following: (a) diverging for smaller wavelength, (b) parallel for normal incident wavelength, and (c) crossing for larger wavelength.

6.6 Conclusion

We reviewed the experiments of steering of mid-IR radiation using plasmonic structures consisting of a subwavelength single slit flanked by periodic subwavelength grooves on a semiconductor substrate. Later, we proposed the numerical technique to extend the FEM-calculated electromagnetic waves to the extremely far-field regime, which is not accessible by conventional FEM routines. The model fully describing the formation of the directional beams was proposed. The robustness of the model and underlying physics was illustrated on the mid-IR beaming experiments, FEM simulations, and scattering field calculations. The developed formalism is very crucial for optical and plasmonic applications, including on-chip, sensing and security devices. Even though we focus this work on mid-IR frequency, the approach is directly applicable to visible, near-IR, THz, and microwave frequencies.

Bibliography

[1] K. E. Drexler, "Molecular engineering: An approach to the development of general capabilities for molecular manipulation," Proceedings of the National Academy of Sciences of the United States of America, 78(9), 5275-5278 (1981).

[2] C. M. Lieber, "Nanoscale science and technology: Building a big future from small things," MRS Bulletin, 28(7), 486-491 (2003).

[3] H. W. Kroto, J. R. Heath, S. C. O'Brien *et al.*, "C60: Buckminsterfullerene," Nature, 318(6042), 162-163 (1985).

[4] S. Iijima, "Helical microtubules of graphitic carbon," Nature, 354(6348), 56-58 (1991).

[5] R. H. Baughman, A. A. Zakhidov, and W. A. de Heer, "Carbon nanotubes - the route toward applications," Science, 297(5582), 787-792 (2002).

[6] A. J. Hoffman, L. Alekseyev, S. S. Howard *et al.*, "Negative refraction in semiconductor metamaterials," Nature Materials, 6(12), 946-950 (2007).

[7] P. Evans, W. R. Hendren, R. Atkinson *et al.*, "Growth and properties of gold and nickel nanorods in thin film alumina," Nanotechnology, 17(23), 5746-5753 (2006).

[8] S. Zhang, Y. S. Park, J. S. Li *et al.*, "Negative refractive index in chiral metamaterials," Physical Review Letters, 102(2), 023901 (2009).

[9] V. M. Shalaev, W. S. Cai, U. K. Chettiar *et al.*, "Negative index of refraction in optical metamaterials," Optics Letters, 30(24), 3356-3358 (2005).

[10] Y. F. Mei, G. S. Huang, A. A. Solovev *et al.*, "Versatile approach for integrative and functionalized tubes by strain engineering of nanomembranes on polymers," Advanced Materials, 20(21), 4085-4090 (2008).

[11] V. Wagner, A. Dullaart, A. K. Bock *et al.*, "The emerging nanomedicine landscape," Nature Biotechnology, 24(10), 1211-1217 (2006).

[12] A. V. Kabashin, P. Evans, S. Pastkovsky *et al.*, "Plasmonic nanorod metamaterials for biosensing," Nature Materials, 8(11), 867-871 (2009).

[13] R. D. Piner, J. Zhu, F. Xu *et al.*, ""Dip-pen" nanolithography," Science, 283(5402), 661-663 (1999).

[14] Z. Jacob, L. V. Alekseyev, and E. Narimanov, "Optical hyperlens: Far-field imaging beyond the diffraction limit," Optics Express, 14(18), 8247-8256 (2006).

[15] A. A. Govyadinov, and V. A. Podolskiy, “Metamaterial photonic funnels for subdiffraction light compression and propagation,” Physical Review B, 73(15), 155108 (2006).

[16] S. Thongrattanasiri, and V. A. Podolskiy, “Hypergratings: Nanophotonics in planar anisotropic metamaterials,” Optics Letters, 34(7), 890-892 (2009).

[17] V. A. Podolskiy, and S. Thongrattanasiri, “Hypergratings: Far-field subwavelength focusing in planar metamaterials,” Proceedings of SPIE, 7392, 73921A (2009).

[18] N. M. Litchinitser, and V. M. Shalaev, “Metamaterials: Transforming theory into reality,” Journal of the Optical Society of America B-Optical Physics, 26(12), B161-B169 (2009).

[19] J. B. Pendry, “Negative refraction makes a perfect lens,” Physical Review Letters, 85(18), 3966-3969 (2000).

[20] J. B. Pendry, A. J. Holden, W. J. Stewart *et al.*, “Extremely low frequency plasmons in metallic mesostructures,” Physical Review Letters, 76(25), 4773-4776 (1996).

[21] J. B. Pendry, A. J. Holden, D. J. Robbins *et al.*, “Magnetism from conductors and enhanced nonlinear phenomena,” IEEE Transactions on Microwave Theory and Techniques, 47(11), 2075-2084 (1999).

[22] D. R. Smith, W. J. Padilla, D. C. Vier *et al.*, “Composite medium with simultaneously negative permeability and permittivity,” Physical Review Letters, 84(18), 4184-4187 (2000).

[23] R. A. Shelby, D. R. Smith, and S. Schultz, “Experimental verification of a negative index of refraction,” Science, 292(5514), 77-79 (2001).

[24] R. A. Shelby, D. R. Smith, S. C. Nemat-Nasser *et al.*, “Microwave transmission through a two-dimensional, isotropic, left-handed metamaterial,” Applied Physics Letters, 78(4), 489-491 (2001).

[25] A. A. Houck, J. B. Brock, and I. L. Chuang, “Experimental observations of a left-handed material that obeys Snell's law,” Physical Review Letters, 90(13), 137401 (2003).

[26] A. Mary, S. G. Rodrigo, F. J. Garcia-Vidal *et al.*, “Theory of negative-refractive-index response of double-fishnet structures,” Physical Review Letters, 101(10), 103902 (2008).

[27] E. Plum, J. Zhou, J. Dong *et al.*, “Metamaterial with negative index due to chirality,” Physical Review B, 79(3), 035407 (2009).

[28] Z. X. Tang, H. Zhang, Y. X. Ye *et al.*, “Negative refraction in a honeycomb-lattice photonic crystal,” Solid State Communications, 141, 183-187 (2007).

[29] Y. F. Chen, P. Fischer, and F. W. Wise, “Negative refraction at optical frequencies in nonmagnetic two-component molecular media,” Physical Review Letters, 95(6), 067402 (2005).

[30] Y. F. Chen, P. Fischer, and F. W. Wise, “Comment on "Negative refraction at optical frequencies in nonmagnetic two-component molecular media" - Reply,” Physical Review Letters, 98(5), 059702 (2007).

[31] G. Dolling, C. Enkrich, M. Wegener *et al.*, “Simultaneous negative phase and group velocity of light in a metamaterial,” Science, 312(5775), 892-894 (2006).

[32] G. Dolling, M. Wegener, C. M. Soukoulis *et al.*, “Negative-index metamaterial at 780 nm wavelength,” Optics Letters, 32(1), 53-55 (2007).

[33] S. Y. Liu, W. K. Chen, J. J. Du *et al.*, “Manipulating negative-refractive behavior with a magnetic field,” Physical Review Letters, 101(15), 157407 (2008).

[34] S. Zhang, W. J. Fan, N. C. Panoiu *et al.*, “Experimental demonstration of near-infrared negative-index metamaterials,” Physical Review Letters, 95(13), 137404 (2005).

[35] S. Zhang, W. J. Fan, K. J. Malloy *et al.*, “Demonstration of metal-dielectric negative-index metamaterials with improved performance at optical frequencies,” Journal of the Optical Society of America B-Optical Physics, 23(3), 434-438 (2006).

[36] D. R. Smith, J. B. Pendry, and M. C. K. Wiltshire, “Metamaterials and negative refractive index,” Science, 305(5685), 788-792 (2004).

[37] N. Liu, H. Liu, S. N. Zhu *et al.*, “Stereometamaterials,” Nature Photonics, 3(3), 157-162 (2009).

[38] I. V. Lindell, S. A. Tretyakov, K. I. Nikoskinen *et al.*, “BW media-media with negative parameters, capable of supporting backward waves,” Microwave and Optical Technology Letters, 31(2), 129-133 (2001).

[39] P. A. Belov, “Backward waves and negative refraction in uniaxial dielectrics with negative dielectric permittivity along the anisotropy axis,” Microwave and Optical Technology Letters, 37(4), 259-263 (2003).

[40] T. M. Grzegorczyk, M. Nikku, X. D. Chen *et al.*, “Refraction laws for anisotropic media and their application to left-handed metamaterials,” IEEE Transactions on Microwave Theory and Techniques, 53(4), 1443-1450 (2005).

[41] R. Wangberg, J. Elser, E. E. Narimanov *et al.*, “Nonmagnetic nanocomposites for optical and infrared negative-refractive-index media,” Journal of the Optical Society of America B-Optical Physics, 23(3), 498-505 (2006).

[42] V. A. Podolskiy, and E. E. Narimanov, “Strongly anisotropic waveguide as a nonmagnetic left-handed system,” Physical Review B, 71(20), 201101(R) (2005).

[43] V. A. Podolskiy, L. V. Alekseyev, and E. E. Narimanov, "Strongly anisotropic media: The THz perspectives of left-handed materials," Journal of Modern Optics, 52(16), 2343-2349 (2005).

[44] J. Yao, Z. W. Liu, Y. M. Liu *et al.*, "Optical negative refraction in bulk metamaterials of nanowires," Science, 321(5891), 930-930 (2008).

[45] M. A. Noginov, Y. A. Barnakov, G. Zhu *et al.*, "Bulk photonic metamaterial with hyperbolic dispersion," Applied Physics Letters, 94(15), 151105 (2009).

[46] P. V. Parimi, W. T. T. Lu, P. Vodo *et al.*, "Photonic crystals - imaging by flat lens using negative refraction," Nature, 426, 404-404 (2003).

[47] A. Grbic, and G. V. Eleftheriades, "Overcoming the diffraction limit with a planar left-handed transmission-line lens," Physical Review Letters, 92(11), 117403 (2004).

[48] R. J. Blaikie, and D. O. S. Melville, "Imaging through planar silver lenses in the optical near field," Journal of Optics A-Pure and Applied Optics, 7(2), S176-S183 (2005).

[49] H. Lee, Y. Xiong, N. Fang *et al.*, "Realization of optical superlens imaging below the diffraction limit," New Journal of Physics, 7, 255 (2005).

[50] N. Fang, H. Lee, C. Sun *et al.*, "Sub-diffraction-limited optical imaging with a silver superlens," Science, 308(5721), 534-537 (2005).

[51] Smolyaninov, II, Y. J. Hung, and C. C. Davis, "Magnifying superlens in the visible frequency range," Science, 315(5819), 1699-1701 (2007).

[52] X. Zhang, and Z. W. Liu, "Superlenses to overcome the diffraction limit," Nature Materials, 7(6), 435-441 (2008).

[53] A. Schilling, J. Schilling, C. Reinhardt *et al.*, "A superlens for the deep ultraviolet," Applied Physics Letters, 95(12), 121909 (2009).

[54] P. Chaturvedi, W. Wu, V. J. Logeeswaran *et al.*, "A smooth optical superlens," Applied Physics Letters, 96(4), 043102 (2010).

[55] T. Taubner, D. Korobkin, Y. Urzhumov *et al.*, "Near-field microscopy through a SiC superlens," Science, 313(5793), 1595-1595 (2006).

[56] A. Alu, and N. Engheta, "Physical insight into the "growing" evanescent fields of double-negative metamaterial lenses using their circuit equivalence," IEEE Transactions on Antennas and Propagation, 54(1), 268-272 (2006).

[57] J. O. Dimmock, "Losses in left-handed materials," Optics Express, 11(19), 2397-2402 (2003).

[58] R. Merlin, “Analytical solution of the almost-perfect-lens problem,” Applied Physics Letters, 84(8), 1290-1292 (2004).

[59] I. A. Larkin, and M. I. Stockman, “Imperfect perfect lens,” Nano Letters, 5(2), 339-343 (2005).

[60] V. A. Podolskiy, and E. E. Narimanov, “Near-sighted superlens,” Optics Letters, 30(1), 75-77 (2005).

[61] A. Salandrino, and N. Engheta, “Far-field subdiffraction optical microscopy using metamaterial crystals: Theory and simulations,” Physical Review B, 74(7), 075103 (2006).

[62] Z. Jacob, L. V. Alekseyev, and E. Narimanov, “Semiclassical theory of the hyperlens,” Journal of the Optical Society of America A-Optics Image Science and Vision, 24(10), A52-A59 (2007).

[63] A. V. Kildishev, and E. E. Narimanov, “Impedance-matched hyperlens,” Optics Letters, 32(23), 3432-3434 (2007).

[64] Z. W. Liu, H. Lee, Y. Xiong *et al.*, “Far-field optical hyperlens magnifying sub-diffraction-limited objects,” Science, 315(5819), 1686-1686 (2007).

[65] H. Lee, Z. Liu, Y. Xiong *et al.*, “Development of optical hyperlens for imaging below the diffraction limit,” Optics Express, 15(24), 15886-15891 (2007).

[66] A. V. Kildishev, and V. M. Shalaev, “Engineering space for light via transformation optics,” Optics Letters, 33(1), 43-45 (2008).

[67] E. J. Smith, Z. Liu, Y. F. Mei *et al.*, “System investigation of a rolled-up metamaterial optical hyperlens structure,” Applied Physics Letters, 95(8), 083104 (2009).

[68] A. V. Kildishev, U. K. Chettiar, Z. Jacob *et al.*, “Materializing a binary hyperlens design,” Applied Physics Letters, 94(7), 071102 (2009).

[69] V. M. Shalaev, “Transforming light,” Science, 322(5900), 384-386 (2008).

[70] J. B. Pendry, D. Schurig, and D. R. Smith, “Controlling electromagnetic fields,” Science, 312(5781), 1780-1782 (2006).

[71] U. Leonhardt, “Optical conformal mapping,” Science, 312(5781), 1777-1780 (2006).

[72] U. Leonhardt, “Notes on conformal invisibility devices,” New Journal of Physics, 8, 118 (2006).

[73] S. A. Cummer, B. I. Popa, D. Schurig *et al.*, “Full-wave simulations of electromagnetic cloaking structures,” Physical Review E, 74(3), 036621 (2006).

[74] D. Schurig, J. J. Mock, B. J. Justice *et al.*, "Metamaterial electromagnetic cloak at microwave frequencies," Science, 314(5801), 977-980 (2006).

[75] Smolyaninov, II, Y. J. Hung, and C. C. Davis, "Two-dimensional metamaterial structure exhibiting reduced visibility at 500 nm," Optics Letters, 33(12), 1342-1344 (2008).

[76] Z. Jacob, and E. E. Narimanov, "Semiclassical description of non magnetic cloaking," Optics Express, 16(7), 4597-4604 (2008).

[77] M. Rahm, D. Schurig, D. A. Roberts *et al.*, "Design of electromagnetic cloaks and concentrators using form-invariant coordinate transformations of Maxwell's equations," Photonics and Nanostructures-Fundamentals and Applications, 6(1), 87-95 (2008).

[78] J. S. Li, and J. B. Pendry, "Hiding under the carpet: A new strategy for cloaking," Physical Review Letters, 101(20), 203901 (2008).

[79] A. Alu, and N. Engheta, "Cloaking a sensor," Physical Review Letters, 102(23), 233901 (2009).

[80] B. Edwards, A. Alu, M. G. Silveirinha *et al.*, "Experimental verification of plasmonic cloaking at microwave frequencies with metamaterials," Physical Review Letters, 103(15), 153901 (2009).

[81] R. Liu, C. Ji, J. J. Mock *et al.*, "Broadband ground-plane cloak," Science, 323(5912), 366-369 (2009).

[82] P. A. Huidobro, M. L. Nesterov, L. Martin-Moreno *et al.*, "Transformation optics for plasmonics," Nano Letters, 10(6), 1985-1990 (2010).

[83] T. Ergin, N. Stenger, P. Brenner *et al.*, "Three-dimensional invisibility cloak at optical wavelengths," Science, 328(5976), 337-339 (2010).

[84] U. Leonhardt, and T. G. Philbin, "General relativity in electrical engineering," New Journal of Physics, 8, 247 (2006).

[85] A. Greenleaf, Y. Kurylev, M. Lassas *et al.*, "Electromagnetic wormholes and virtual magnetic monopoles from metamaterials," Physical Review Letters, 99(18), 183901 (2007).

[86] D. A. Genov, S. Zhang, and X. Zhang, "Mimicking celestial mechanics in metamaterials," Nature Physics, 5(9), 687-692 (2009).

[87] M. Li, R. X. Miao, and Y. Pang, "More studies on metamaterials mimicking de Sitter space," Optics Express, 18(9), 9026-9033 (2010).

[88] Q. Cheng, T. J. Cui, W. X. Jiang *et al.*, "An omnidirectional electromagnetic absorber made of metamaterials," New Journal of Physics, 12, 063006 (2010).

[89] I. I. Smolyaninov, “Metamaterial "Multiverse",” arXiv:1005.1002, 13 (2010).

[90] I. I. Smolyaninov, “Optical models of the big bang and non-trivial space-time metrices based on metamaterials,” arXiv:0908.2407, 3 (2010).

[91] I. I. Smolyaninov, and E. E. Narimanov, “Metric Signature Transitions in Optical Metamaterials,” Physical Review Letters, 105(6), 067402 (2010).

[92] A. D. Boardman, [Electromagnetic Surface Modes] Wiley, Chichester ; New York (1982).

[93] H. Raether, [Surface Plasmons on Smooth and Rough Surfaces and on Gratings] Springer-Verlag, Berlin ; New York (1988).

[94] W. L. Barnes, A. Dereux, and T. W. Ebbesen, “Surface plasmon subwavelength optics,” Nature, 424(6950), 824-830 (2003).

[95] A. V. Zayats, Smolyaninov, II, and A. A. Maradudin, “Nano-optics of surface plasmon polaritons,” Physics Reports-Review Section of Physics Letters, 408(3-4), 131-314 (2005).

[96] S. I. Bozhevolnyi, and V. M. Shalaev, “Nanophotonics with surface plasmons - Part I - The evolving field of nanophotonics seeks to combine the capabilities of nanotechnology and photonics,” Photonics Spectra, 40(1), 58-66 (2006).

[97] V. M. Shalaev, and S. I. Bozhevolnyi, “Nanophotonics with surface plasmons - Part II - The evolving technology of plasmonic nanophotonics seeks to combine the capabilities of nanotechnology and photonics,” Photonics Spectra, 40(2), 66-72 (2006).

[98] C. Genet, and T. W. Ebbesen, “Light in tiny holes,” Nature, 445, 39-46 (2007).

[99] F. J. Garcia-Vidal, L. Martin-Moreno, T. W. Ebbesen *et al.*, “Light passing through subwavelength apertures,” Reviews of Modern Physics, 82(1), 729-787 (2010).

[100] T. W. Ebbesen, H. J. Lezec, H. F. Ghaemi *et al.*, “Extraordinary optical transmission through sub-wavelength hole arrays,” Nature, 391(6668), 667-669 (1998).

[101] L. Martin-Moreno, F. J. Garcia-Vidal, H. J. Lezec *et al.*, “Theory of extraordinary optical transmission through subwavelength hole arrays,” Physical Review Letters, 86(6), 1114-1117 (2001).

[102] W. L. Barnes, W. A. Murray, J. Dintinger *et al.*, “Surface plasmon polaritons and their role in the enhanced transmission of light through periodic arrays of subwavelength holes in a metal film,” Physical Review Letters, 92(10), 107401 (2004).

[103] J. Dintinger, A. Degiron, and T. W. Ebbesen, “Enhanced light transmission through subwavelength holes,” MRS Bulletin, 30(5), 381-384 (2005).

[104] J. B. Pendry, L. Martin-Moreno, and F. J. Garcia-Vidal, "Mimicking surface plasmons with structured surfaces," Science, 305(5685), 847-848 (2004).

[105] F. J. Garcia-Vidal, L. Martin-Moreno, and J. B. Pendry, "Surfaces with holes in them: New plasmonic metamaterials," Journal of Optics A-Pure and Applied Optics, 7(2), S97-S101 (2005).

[106] T. SÃ¸ndergaard, S. I. Bozhevolnyi, S. M. Novikov *et al.*, "Extraordinary Optical Transmission Enhanced by Nanofocusing," Nano Letters, 10(8), 3123-3128 (2010).

[107] H. J. Lezec, A. Degiron, E. Devaux *et al.*, "Beaming light from a subwavelength aperture," Science, 297(5582), 820-822 (2002).

[108] L. Martin-Moreno, F. J. Garcia-Vidal, H. J. Lezec *et al.*, "Theory of highly directional emission from a single subwavelength aperture surrounded by surface corrugations," Physical Review Letters, 90(16), 167401 (2003).

[109] C. T. Wang, C. L. Du, and X. G. Luo, "Refining the model of light diffraction from a subwavelength slit surrounded by grooves on a metallic film," Physical Review B, 74(24), 245403 (2006).

[110] F. J. Garcia-Vidal, H. J. Lezec, T. W. Ebbesen *et al.*, "Multiple paths to enhance optical transmission through a single subwavelength slit," Physical Review Letters, 90(21), 213901 (2003).

[111] L. B. Yu, D. Z. Lin, Y. C. Chen *et al.*, "Physical origin of directional beaming emitted from a subwavelength slit," Physical Review B, 71(4), 041405(R) (2005).

[112] D. C. Adams, S. Thongrattanasiri, T. Ribaudo *et al.*, "Plasmonic mid-infrared beam steering," Applied Physics Letters, 96(20), 201112 (2010).

[113] S. Thongrattanasiri, D. Adams, D. Wasserman *et al.*, "Beam shaping by corrugated plasmonic systems," under consideration, (2010).

[114] W. Dai, and C. M. Soukoulis, "Control of beaming angles via a subwavelength metallic slit surrounded by grooves," Physical Review B, 82(4), 045427 (2010).

[115] V. G. Veselago, "The electrodynamics of substances with simultaneously negative values of permittivity and permeability," Soviet Physics Uspekhi, 10(4), 509-514 (1968).

[116] M. Born, and E. Wolf, [Principles of Optics: Electromagnetic Theory of Propagation, Interference and Diffraction of Light] Cambridge University Press, (1999).

[117] L. D. Landau, and E. M. Lifshitz, [Electrodynamics of Continuous Media] Pergamon Press, (1984).

[118] J. D. Jackson, [Classical Electrodynamics] John Wiley & Sons, Inc., (1999).

[119] A. J. Hoffman, V. A. Podolskiy, D. L. Sivco *et al.*, "Sub-diffraction negative and positive index modes in mid-infrared waveguides," Optics Express, 16(21), 16404-16409 (2008).

[120] A. J. Hoffman, A. Sridhar, P. X. Braun *et al.*, "Midinfrared semiconductor optical metamaterials," Journal of Applied Physics, 105(12), 122411 (2009).

[121] B. D. F. Casse, W. T. Lu, Y. J. Huang *et al.*, "Super-resolution imaging using a three-dimensional metamaterials nanolens," Applied Physics Letters, 96(2), 023114 (2010).

[122] R. Atkinson, W. R. Hendren, G. A. Wurtz *et al.*, "Anisotropic optical properties of arrays of gold nanorods embedded in alumina," Physical Review B, 73(23), 235402 (2006).

[123] G. A. Wurtz, W. Dickson, D. O'Connor *et al.*, "Guided plasmonic modes in nanorod assemblies: Strong electromagnetic coupling regime," Optics Express, 16(10), 7460-7470 (2008).

[124] L. V. Alekseyev, and E. Narimanov, "Slow light and 3D imaging with non-magnetic negative index systems," Optics Express, 14(23), 11184-11193 (2006).

[125] M. J. Weber, [Handbook of Optical Materials] CRC Press, (2003).

[126] D. R. Lide, [CRC Handbook of Chemistry and Physics] CRC Press, (2008).

[127] P. J. Collings, and M. Hird, [Introduction to Liquid Crystal] Taylor & Francis, (1997).

[128] Y. Igasaki, F. H. Li, N. Yoshida *et al.*, "High efficiency electrically-addressable phase-only spatial light modulator," Optical Review, 6(4), 339-344 (1999).

[129] H. Sarkissian, S. V. Serak, N. V. Tabiryan *et al.*, "Polarization-controlled switching between diffraction orders in transverse-periodically aligned nematic liquid crystals," Optics Letters, 31(15), 2248-2250 (2006).

[130] H. Sarkissian, B. Park, N. Tabirian *et al.*, "Periodically aligned liquid crystal: Potential application for projection displays," Molecular Crystals and Liquid Crystals, 451(1), 1-19 (2006).

[131] W. T. Lu, and S. Sridhar, "Superlens imaging theory for anisotropic nanostructured metamaterials with broadband all-angle negative refraction," Physical Review B, 77(23), 233101 (2008).

[132] Z. Jacob, I. I. Smolyaninov, and E. E. Narimanov, "Broadband Purcell effect: Radiative decay engineering with metamaterials," arXiv:0910.3981v2, (2009).

[133] H. N. S. Krishnamoorthy, Z. Jacob, E. E. Narimanov *et al.*, "Metamaterial based broadband engineering of quantum dot spontaneous emission," arXiv:0912.2454v1, (2009).

[134] M. A. Noginov, H. Li, Y. A. Barnakov *et al.*, “Controlling spontaneous emission with metamaterials,” Optics Letters, 35(11), 1863-1865 (2010).

[135] V. A. Podolskiy, R. Wangberg, J. Elser *et al.*, "Left-handed high energy density waveguides: Nano-light propagation and focusing." Proceedings of SPIE, 6002, 600205 (2005).

[136] J. Elser, and V. A. Podolskiy, “Scattering-free plasmonic optics with anisotropic metamaterials,” Physical Review Letters, 100(6), 066402 (2008).

[137] S. Thongrattanasiri, J. Elser, and V. A. Podolskiy, “Quasi-planar optics: Computing light propagation and scattering in planar waveguide arrays,” Journal of the Optical Society of America B-Optical Physics, 26(12), B102-B110 (2009).

[138] J. W. Goodman, [Introduction to Fourier Optics] The McGraw-Hill Companies, Inc., (1996).

[139] E. Abbe, “Beitrage zur theorie des mikroskops und der mikroskopischen,” Arch. mikrosk. Anat. Entwichlungsmech., 9(1), 413-418 (1873).

[140] J. C. Maxwell Garnett, “Colours in metal glasses and in metallic films,” Philosophical Transactions of the Royal Society of London. Series A, Containing Papers of a Methematical or Physical Character, 203, 385-420 (1904).

[141] V. D. A. G. Bruggeman, “Berechnung verschiedener physikalischer konstanten von heterogenen substanzen,” Annalen der Physik, 24, 636-664 (1935).

[142] T. C. Choy, [Effective Medium Theory: Principles and Applications] Oxford University Press, (1999).

[143] G. W. Milton, [The Theory of Composites] Cambridge University Press, Cambridge ; New York (2002).

[144] H. C. Weissker, J. Furthmuller, and F. Bechstedt, “Optical properties of Ge and Si nanocrystallites from ab initio calculations. I. Embedded nanocrystallites,” Physical Review B, 65(15), 155327 (2002).

[145] H. C. Weissker, J. Furthmuller, and F. Bechstedt, “Optical properties of Ge and Si nanocrystallites from ab initio calculations. II. Hydrogenated nanocrystallites,” Physical Review B, 65(15), 155328 (2002).

[146] H. C. Weissker, J. Furthmuller, and F. Bechstedt, “Validity of effective-medium theory for optical properties of embedded nanocrystallites from ab initio supercell calculations,” Physical Review B, 67(16), 165322 (2003).

[147] J. Elser, R. Wangberg, V. A. Podolskiy *et al.*, “Nanowire metamaterials with extreme optical anisotropy,” Applied Physics Letters, 89(26), 261102 (2006).

[148] A. N. Lagarkov, and A. K. Sarychev, "Electromagnetic properties of composites containing elongated conducting inclusions," Physical Review B, 53(10), 6318-6336 (1996).

[149] E. D. Palik, [Handbook of Optical Constants of Solids] Academic Press, (1997).

[150] J. Elser, V. A. Podolskiy, I. Salakhutdinov *et al.*, "Nonlocal effects in effective-medium response of nanolayered metamaterials," Applied Physics Letters, 90(19), 191109 (2007).

[151] P. A. Belov, and Y. Hao, "Subwavelength imaging at optical frequencies using a transmission device formed by a periodic layered metal-dielectric structure operating in the canalization regime," Physical Review B, 73(11), 113110 (2006).

[152] R. J. Pollard, A. Murphy, W. R. Hendren *et al.*, "Optical nonlocalities and additional waves in epsilon-near-zero metamaterials," Physical Review Letters, 102(12), 127405 (2009).

[153] W. S. Cai, U. K. Chettiar, A. V. Kildishev *et al.*, "Optical cloaking with metamaterials," Nature Photonics, 1(4), 224-227 (2007).

[154] V. M. Shalaev, "Optical negative-index metamaterials," Nature Photonics, 1(1), 41-48 (2007).

[155] M. I. Stockman, "Nanofocusing of optical energy in tapered plasmonic waveguides," Physical Review Letters, 93(13), 137404 (2004).

[156] R. Merlin, "Radiationless electromagnetic interference: Evanescent-field lenses and perfect focusing," Science, 317(5840), 927-929 (2007).

[157] A. Grbic, and R. Merlin, "Near-field focusing plates and their design," IEEE Transactions on Antennas and Propagation, 56(10), 3159-3165 (2008).

[158] A. Grbic, L. Jiang, and R. Merlin, "Near-field plates: Subdiffraction focusing with patterned surfaces," Science, 320(5875), 511-513 (2008).

[159] L. Markley, A. M. H. Wong, Y. Wang *et al.*, "Spatially shifted beam approach to subwavelength focusing," Physical Review Letters, 101(11), 113901 (2008).

[160] Y. Xiong, Z. W. Liu, and X. Zhang, "Projecting deep-subwavelength patterns from diffraction-limited masks using metal-dielectric multilayers," Applied Physics Letters, 93(11), 111116 (2008).

[161] A. Lewis, H. Taha, A. Strinkovski *et al.*, "Near-field optics: From subwavelength illumination to nanometric shadowing," Nature Biotechnology, 21(11), 1377-1386 (2003).

[162] A. Lewis, M. Isaacson, A. Harootunian *et al.*, "Development of a 500-A spatial-resolution light-microscope .1. Light is efficiently transmitted through GAMMA-16 diameter apertures," Ultramicroscopy, 13(3), 227-231 (1984).

[163] E. A. Ash, and G. Nicholls, "Super-resolution aperture scanning microscope," Nature, 237(5357), 510-512 (1972).

[164] A. A. Govyadinov, and V. A. Podolskiy, "Sub-diffraction light propagation in fibres with anisotropic dielectric cores," Journal of Modern Optics, 53(16-17), 2315-2324 (2006).

[165] C. Reinhardt, S. Passinger, B. N. Chichkov *et al.*, "Restructuring and modification of metallic nanorod arrays using femtosecond laser direct writing," Applied Physics Letters, 89(23), 231117 (2006).

[166] K. G. Balmain, A. A. E. Luttgen, and P. C. Kremer, "Resonance cone formation, reflection, refraction, and focusing in a planar anisotropic metamaterial," IEEE Antennas and Wireless Propagation Letters, 1, 146-149 (2002).

[167] R. K. Fisher, and R. W. Gould, "Resonance cones in the field pattern of a short antenna in an anisotropic plasma," Physical Review Letters, 22(21), 1093-1095 (1969).

[168] P. A. Belov, C. R. Simovski, and P. Ikonen, "Canalization of subwavelength images by electromagnetic crystals," Physical Review B, 71(19), 193105 (2005).

[169] P. A. Belov, Y. Hao, and S. Sudhakaran, "Subwavelength microwave imaging using an array of parallel conducting wires as a lens," Physical Review B, 73(3), 033108 (2006).

[170] E. Shamonina, V. A. Kalinin, K. H. Ringhofer *et al.*, "Imaging, compression and Poynting vector streamlines for negative permittivity materials," Electronics Letters, 37(20), 1243-1244 (2001).

[171] S. A. Ramakrishna, and J. B. Pendry, "Removal of absorption and increase in resolution in a near-field lens via optical gain," Physical Review B, 67(20), 201101(R) (2003).

[172] M. A. Noginov, V. A. Podolskiy, G. Zhu *et al.*, "Compensation of loss in propagating surface plasmon polariton by gain in adjacent dielectric medium," Optics Express, 16(2), 1385-1392 (2008).

[173] M. A. Noginov, "Compensation of surface plasmon loss by gain in dielectric medium," Journal of Nanophotonics, 2, 021855 (2008).

[174] M. I. Stockman, "Criterion for negative refraction with low optical losses from a fundamental principle of causality," Physical Review Letters, 98(17), 177404 (2007).

[175] G. Dolling, C. Enkrich, M. Wegener *et al.*, "Low-loss negative-index metamaterial at telecommunication wavelengths," Optics Letters, 31(12), 1800-1802 (2006).

[176] J. B. Khurgin, and G. Sun, "In search of the elusive lossless metal," Applied Physics Letters, 96(18), 181102 (2010).

[177] A. L. Pokrovsky, and A. L. Efros, "Nonlocal electrodynamics of two-dimensional wire mesh photonic crystals," Physical Review B, 65(4), 045110 (2002).

[178] C. Bremer, and R. Weissleder, "Molecular imaging - In vivo imaging of gene expression: MR and optical technologies," Academic Radiology, 8(1), 15-23 (2001).

[179] R. Weissleder, and U. Mahmood, "Molecular imaging," Radiology, 219(2), 316-333 (2001).

[180] Z. W. Liu, Q. H. Wei, and X. Zhang, "Surface plasmon interference nanolithography," Nano Letters, 5(5), 957-961 (2005).

[181] W. Srituravanich, N. Fang, C. Sun *et al.*, "Plasmonic nanolithography," Nano Letters, 4(6), 1085-1088 (2004).

[182] B. D. Terris, H. J. Mamin, D. Rugar *et al.*, "Near-field optical-data storage using a solid immersion lens," Applied Physics Letters, 65(4), 388-390 (1994).

[183] B. D. Terris, H. J. Mamin, and D. Rugar, "Near-field optical data storage," Applied Physics Letters, 68(2), 141-143 (1996).

[184] B. H. Cumpston, S. P. Ananthavel, S. Barlow *et al.*, "Two-photon polymerization initiators for three-dimensional optical data storage and microfabrication," Nature, 398(6722), 51-54 (1999).

[185] S. W. Hell, and J. Wichmann, "Breaking the diffraction resolution limit by stimulated-emission - stimulated-emission-depletion fluorescence microscopy," Optics Letters, 19(11), 780-782 (1994).

[186] S. W. Hell, "Toward fluorescence nanoscopy," Nature Biotechnology, 21(11), 1347-1355 (2003).

[187] B. Hein, K. I. Willig, and S. W. Hell, "Stimulated emission depletion (STED) nanoscopy of a fluorescent protein-labeled organelle inside a living cell," Proceedings of the National Academy of Sciences of the United States of America, 105(38), 14271-14276 (2008).

[188] R. Heintzmann, and C. Cremer, "Laterally Modulated Excitation Microscopy: Improvement of resolution by using a diffraction grating," Proceedings of SPIE, 3568, 185-196 (1998).

[189] M. G. L. Gustafsson, "Surpassing the lateral resolution limit by a factor of two using structured illumination microscopy," Journal of Microscopy, 198, 82-87 (2000).

[190] M. G. L. Gustafsson, "Nonlinear structured-illumination microscopy: Wide-field fluorescence imaging with theoretically unlimited resolution," Proceedings of the National Academy of Sciences of the United States of America, 102, 13081-13086 (2005).

[191] L. Schermelleh, P. M. Carlton, S. Haase *et al.*, "Subdiffraction multicolor imaging of the nuclear periphery with 3D structured illumination microscopy," Science, 320(5881), 1332-1336 (2008).

[192] F. Wei, and Z. Liu, "Plasmonic Structured Illumination Microscopy," Nano Letters, 10(7), 2531-2536 (2010).

[193] S. Durant, Z. W. Liu, J. A. Steele *et al.*, "Theory of the transmission properties of an optical far-field superlens for imaging beyond the diffraction limit," Journal of the Optical Society of America B-Optical Physics, 23(11), 2383-2392 (2006).

[194] Z. W. Liu, S. Durant, H. Lee *et al.*, "Experimental studies of far-field superlens for sub-diffractional optical imaging," Optics Express, 15(11), 6947-6954 (2007).

[195] H. Lee, Z. W. Liu, Y. Xiong *et al.*, "Design, fabrication and characterization of a far-field superlens," Solid State Communications, 146(5-6), 202-207 (2008).

[196] Y. Xiong, Z. Liu, C. Sun *et al.*, "Two-dimensional Imaging by far-field superlens at visible wavelengths," Nano Letters, 7(11), 3360-3365 (2007).

[197] S. Thongrattanasiri, N. A. Kuhta, M. D. Escarra *et al.*, "Analytical technique for subwavelength far field imaging," under consideration, (2010).

[198] C. Palmer, [Diffraction Grating Handbook] Newport Corporation, (2005).

[199] M. G. Moharam, and T. K. Gaylord, "Diffraction analysis of dielectric surface-relief gratings," Journal of the Optical Society of America, 72(10), 1385-1392 (1982).

[200] M. G. Moharam, and T. K. Gaylord, "Rigorous coupled-wave analysis of grating diffraction - E-mode polarization and losses," Journal of the Optical Society of America, 73(4), 451-455 (1983).

[201] M. G. Moharam, E. B. Grann, D. A. Pommet *et al.*, "Formulation for stable and efficient implementation of the rigorous coupled-wave analysis of binary gratings," Journal of the Optical Society of America A-Optics Image Science and Vision, 12(5), 1068-1076 (1995).

[202] M. G. Moharam, D. A. Pommet, E. B. Grann *et al.*, "Stable implementation of the rigorous coupled-wave analysis for surface-relief gratings - enhanced transmittance matrix approach," Journal of the Optical Society of America A-Optics Image Science and Vision, 12(5), 1077-1086 (1995).

[203] W. H. Press, B. P. Flannery, S. A. Teukolsky *et al.*, [Numerical Recipes in FORTRAN77: The Art of Scientific Computing] Cambridge University Press, (1992).

[204] For details see COMSOL Multiphysics 3.4 User's Guide and RF Module User's Guide; www.comsol.com.

[205] C. T. Kelley, [Iterative Methods for Optimization] SIAM, Philadelphia (1999).

[206] A. Bondeson, T. Rylander, and P. Ingelstrom, [Computational Electromagnetics] Springer Science+Business Media, Inc., (2005).

[207] V. V. Shevchenko, [Continuous transitions in open waveguides: Introduction to the theory] Golem Press, Boulder, Colo., (1971).

[208] P. J. B. Clarricoats, and K. R. Slinn, "Numerical method for the solution of waveguide-discontinuity problems," Electronics Letters, 2(6), 226-228 (1966).

[209] T. Sondergaard, and S. I. Bozhevolnyi, "Out-of-plane scattering properties of long-range surface plasmon polariton gratings," Physica Status Solidi B-Basic Solid State Physics, 242(15), 3064-3069 (2005).

[210] T. Rozzi, M. Mongiardo, and Institution of Electrical Engineers., [Open electromagnetic waveguides] Institution of Electrical Engineers, London (1997).

[211] M. Hammer, "Quadridirectional eigenmode expansion scheme for 2-D modeling of wave propagation in integrated optics," Optics Communications, 235(4-6), 285-303 (2004).

[212] R. F. Oulton, D. F. P. Pile, Y. Liu *et al.*, "Scattering of surface plasmon polaritons at abrupt surface interfaces: Implications for nanoscale cavities," Physical Review B, 76(3), 035408 (2007).

[213] A. A. Govyadinov, V. A. Podolskiy, and M. A. Noginov, "Active metamaterials: Sign of refractive index and gain-assisted dispersion management," Applied Physics Letters, 91(19), 191103 (2007).

[214] K. F. Riley, M. P. Hobson, and S. J. Bence, [Mathematical Methods for Physics and Engineering] Cambridge University Press, Cambridge (2006).

[215] Smolyaninov, II, D. L. Mazzoni, J. Mait *et al.*, "Experimental study of surface-plasmon scattering by individual surface defects," Physical Review B, 56(3), 1601-1611 (1997).

[216] V. A. Podolskiy, and J. Elser, [Electroplasmonics: Dynamical plasmonic circuits with minimized parasitic scattering (QTuJ2)], (2008).

[217] H. A. Bethe, "Theory of diffraction by small holes," Physical Review, 66(7-8), 163-182 (1944).

[218] D. Z. Lin, C. K. Chang, Y. C. Chen *et al.*, "Beaming light from a subwavelength metal slit surrounded by dielectric surface gratings," Optics Express, 14(8), 3503-3511 (2006).

[219] D. Z. Lin, T. D. Cheng, C. K. Chang *et al.*, "Directional light beaming control by a subwavelength asymmetric surface structure," Optics Express, 15(5), 2585-2591 (2007).

[220] M. Beruete, M. Sorolla, I. Campillo *et al.*, "Enhanced millimeter-wave transmission through subwavelength hole arrays," Optics Letters, 29(21), 2500-2502 (2004).

[221] M. Beruete, I. Campillo, J. S. Dolado *et al.*, "Enhanced microwave transmission and beaming using a subwavelength slot in corrugated plate," IEEE Antennas and Wireless Propagation Letters, 3, 328-331 (2004).

[222] H. Caglayan, I. Bulu, and E. Ozbay, "Beaming of electromagnetic waves emitted through a subwavelength annular aperture," Journal of the Optical Society of America B-Optical Physics, 23(3), 419-422 (2006).

[223] A. P. Hibbins, J. R. Sambles, and C. R. Lawrence, "Gratingless enhanced microwave transmission through a subwavelength aperture in a thick metal plate," Applied Physics Letters, 81(24), 4661-4663 (2002).

[224] Y. G. Liu, H. F. Shi, C. T. Wang *et al.*, "Multiple directional beaming effect of metallic subwavelength slit surrounded by periodically corrugated grooves," Optics Express, 16(7), 4487-4493 (2008).

[225] Z. F. Li, H. Caglayan, E. Colak *et al.*, "Enhanced transmission and directivity from metallic subwavelength apertures with nonuniform and nonperiodic grooves," Applied Physics Letters, 92(1), 011128 (2008).

[226] H. Caglayan, I. Bulu, and E. Ozbay, "Observation of off-axis directional beaming via subwavelength asymmetric metallic gratings," Journal of Physics D-Applied Physics, 42(4), 045105 (2009).

[227] S. Kim, H. Kim, Y. Lim *et al.*, "Off-axis directional beaming of optical field diffracted by a single subwavelength metal slit with asymmetric dielectric surface gratings," Applied Physics Letters, 90(5), 051113 (2007).

[228] H. F. Shi, C. L. Du, and X. G. Luo, "Focal length modulation based on a metallic slit surrounded with grooves in curved depths," Applied Physics Letters, 91(9), 093111 (2007).

[229] G. G. Zheng, L. X. Shi, H. L. Wang *et al.*, "Beam focusing through a tapered subwavelength aperture surrounded by dielectric surface gratings," Optics Communications, 282(20), 4146-4151 (2009).

[230] F. J. Garcia-Vidal, L. Martin-Moreno, H. J. Lezec *et al.*, "Focusing light with a single subwavelength aperture flanked by surface corrugations," Applied Physics Letters, 83(22), 4500-4502 (2003).

[231] S. Kim, Y. Lim, H. Kim *et al.*, "Optical beam focusing by a single subwavelength metal slit surrounded by chirped dielectric surface gratings," Applied Physics Letters, 92(1), 013103 (2008).

[232] J. S. Blakemore, "Semiconducting and other major properties of gallium arsenide," Journal of Applied Physics, 53(10), R123-R181 (1982).

[233] E. A. Shaner, J. G. Cederberg, and D. Wasserman, "Electrically tunable extraordinary optical transmission gratings," Applied Physics Letters, 91(18), 181110 (2007).

[234] T. Ribaudo, E. A. Shaner, S. S. Howard *et al.*, "Active control and spatial mapping of mid-infrared propagating surface plasmons," Optics Express, 17(9), 7019-7024 (2009).

[235] D. Wasserman, E. A. Shaner, and J. G. Cederberg, "Midinfrared doping-tunable extraordinary transmission from sub-wavelength gratings," Applied Physics Letters, 90(19), 191102 (2007).

[236] A. A. Govyadinov, [Subwavelength Light Confinement and Quantum Chaos in Micro- and Nano-structured Metamaterials] Oregon State University, Corvallis (2007).

APPENDICES

Appendix A - Optical Transfer Matrix Formalism

The optical transfer matrix method is a numerical technique used to analyze the propagation of electromagnetic fields through a stratified medium [116]. In this Appendix, we will represent the transfer matrix formalism for our planar structure with uniaxial dielectric constant tensor in the Cartesian coordinate system for both TM- and TE-polarized waves. The solutions will be further developed for scattering and waveguiding problems.

Let us consider the multilayered structure illustrated in Fig. A.1: the structure consists of N layers, each having dielectric constant tensor $\hat{\varepsilon}_j$ [Eq. (2.5)] and thickness $\Delta z_j = z_j - z_{j-1}$. We assume that $z_0 = -\infty$ and $z_N = \infty$. A plane wave with free space wavelength λ_0 is incident on the first layer with an incident angle θ_{inc}. For TM-polarized illumination, the field components comprise $\vec{E}^{TM} = \{E_x^{TM}, 0, E_z^{TM}\}$ and $\vec{H}^{TM} = \{0, H_y^{TM}, 0\}$; Maxwell's equations [Eqs. (2.1)-(2.4)] relate all components as

$$E_x^{TM} = -\frac{\varepsilon_z}{\varepsilon_{xy}} \frac{k_z}{k_x} E_z^{TM} , \tag{A.1}$$

$$H_y^{TM} = -\varepsilon_z \frac{\omega}{c\, k_x} E_z^{TM} , \tag{A.2}$$

where $\omega/c = 2\pi/\lambda 0$ is free-space wavevector, and k_z is related to k_x by the anisotropic dispersion relation [Eq. (2.8)]. E_z^{TM}, defined here as the main field component, is represented as the superposition of incoming $(+z)$ and outgoing $(-z)$ waves with corresponding amplitudes a^+ and a^-, respectively. For an arbitrary layer j, the field inside is given as

$$E_{z;j}^{TM} = a_j^+ e^{ik_{z;j}z} e^{ik_x x} + a_j^- e^{-ik_{z;j}z} e^{ik_x x} . \tag{A.3}$$

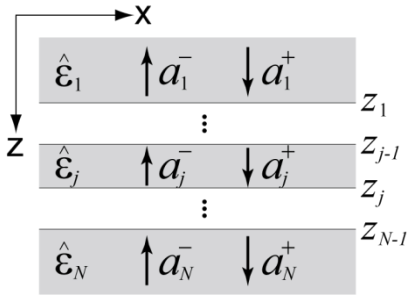

FIGURE A.1: Schematic geometry of the N-layer planar structure for transfer matrix formalism; arrows in each layer illustrate directions of incoming and outgoing waves, a_j^+ and a_j^- at $z = z_j$ interface.

Therefore, the coefficients of layer $j+1$ can be solved by employing boundary conditions at the $z = z_j$ interface. Note that the exponential term $\exp(ik_x x)$ can be neglected due to the continuity of the tangential component of the wavevector k_x along the structure. Using the continuity of E_x^{TM} and D_z^{TM} across the boundary, we obtain a set of equations linearly relating coefficients a_{j+1}^- and a_{j+1}^+ to a_j^- and a_j^+:

$$\begin{bmatrix} a_{j+1}^- \\ a_{j+1}^+ \end{bmatrix} = \alpha_j \begin{bmatrix} (1+K_j)\varphi_j^- & (1-K_j)\varphi_j^+ \\ (1-K_j)/\varphi_j^+ & (1+K_j)/\varphi_j^- \end{bmatrix} \begin{bmatrix} a_j^- \\ a_j^+ \end{bmatrix} \tag{A.4}$$

with $\varphi_j^{\pm}$, α_j, and K_j given by $\varphi_j^{\pm} = \exp\left[i\left(k_{z;j+1} \pm k_{z;j}\right)z_j\right]$, $\alpha_j^{TM} = \varepsilon_{z;j}/2\varepsilon_{z;j+1}$, and $K_j^{TM} = k_{z;j}\varepsilon_{xy;j+1}/\left(k_{z;j+1}\varepsilon_{xy;j}\right)$.

The analysis for TE-polarized wave is very similar. The field components given by $\vec{E}^{TE} = \left\{0, E_y^{TE}, 0\right\}$ and $\vec{H}^{TE} = \{H_x^{TE}, 0, H_z^{TE}\}$, are related to E_y^{TE} by

$$H_x^{TE} = -\frac{k_z c}{\omega} E_y^{TE}, \tag{A.5}$$

$$H_z^{TE} = \frac{k_x c}{\omega} E_y^{TE} \,, \tag{A.6}$$

where k_z is related to k_x by isotropic dispersion relation [Eq. (2.7)]. For a layer j, the main field component, E_y^{TE} is given by

$$E_{y;j}^{TE} = a_j^+ e^{ik_{z;j}z} e^{ik_x x} + a_j^- e^{-ik_{z;j}z} e^{ik_x x} \,. \tag{A.7}$$

Using the continuity of E_y^{TE} and H_z^{TE} across the interface, we obtain another set of equations [Eq. (A.4)] relating a_{j+1}^- and a_{j+1}^+ to a_j^- and a_j^+, and polarization-dependent parameters are given as $\alpha_j^{TE} = 1/2$ and $K_j^{TE} = k_{z;j}/k_{z;j+1}$. Note that in this k_y-independent multilayered planar structure, TM- and TE-polarized fields are completely decoupled; consequently, we can compute the layer-specific coefficients separately, and the full-wave solutions are the linear combination of the decoupled fields.

The set of equations, Eq. (A.4) can be written in general from as

$$\begin{bmatrix} a_{j+1}^- \\ a_{j+1}^+ \end{bmatrix} = \hat{T}_{j,j+1} \begin{bmatrix} a_j^- \\ a_j^+ \end{bmatrix} \tag{A.8}$$

where $\hat{T}_{j,j+1}$ is called *transfer matrix*. Such a matrix can represent field propagation through a layer. For a system with N layers, each layer j has its own transfer matrix $\hat{T}_{j,j+1}$; hence, the system transfer matrix is

$$\hat{T}_{1,N} = \hat{T}_{N-1,N} \dots \hat{T}_{j,j+1} \dots \hat{T}_{2,3} \hat{T}_{1,2} \,. \tag{A.9}$$

When a plane wave is incident on $z = z_1$ interface ($a_1^+ \neq 0$, $a_N^- = 0$), the reflecting (r) and transmitting (t) coefficients of the multilayered planar structure are expressed as

$$r = \frac{a_1^-}{a_1^+} = -\frac{\left(\hat{T}_{1,N}\right)_{12}}{\left(\hat{T}_{1,N}\right)_{11}}, \tag{A.10}$$

$$t = \frac{a_N^+}{a_1^+} = \frac{\det \hat{T}_{1,N}}{\left(\hat{T}_{1,N}\right)_{11}}. \tag{A.11}$$

It is straightforward to show that for single interface structures, Eqs. (A.10)-(A.11) give Fresnel coefficients [116]. Even though the transfer matrix approach is easy to implement and very useful in many applications, the disadvantage we cannot avoid is the numerical error which arises when computing the growing exponential terms of lossy layers. Another method called the relaxation technique [236] requires more computational time, but provides more accurate results when solving the scattering problem for planar structures.

In many situations, we are involved with scattering problems where coefficients a_1^+ and a_N^- are known. Therefore, we can relate the system transfer matrix $\hat{T}_{1,N}$ to the system scattering matrix $\hat{S}_{1,N}$ by

$$\begin{bmatrix} a_1^- \\ a_N^+ \end{bmatrix} = \hat{S}_{1,N} \begin{bmatrix} a_N^- \\ a_1^+ \end{bmatrix} \tag{A.12}$$

$$\hat{S}_{1,N} = \frac{1}{\left(\hat{T}_{1,N}\right)_{11}} \begin{bmatrix} 1 & -\left(\hat{T}_{1,N}\right)_{12} \\ \left(\hat{T}_{1,N}\right)_{21} & \det \hat{T}_{1,N} \end{bmatrix}. \tag{A.13}$$

The equations give the scattering coefficients a_1^- and a_N^+ having linear relations to the incident field coefficients a_1^+ and a_N^-. The scattering problem can be extended to the waveguiding structure where a_1^+, $a_N^- = 0$. The guided modes exist when k_x's yield nontrivial solutions of the guiding dispersion relation, $\det\left[\hat{S}_{1,N}^{-1}(k_x)\right] = 0$ [207, 210].

Appendix B - Coordinates of Fresnel Zones in Phase Aspect

In this Appendix, we will derive the coordinates of the boundaries of Fresnel zones with hyperbolic metamaterials [Eq. (3.5)] by explicitly calculating proper phase relationships. The phase difference of each Fresnel zone (φ_m) and the first zone (φ_0) is [Fig. B.1]

$$\varphi_m - \varphi_0 = \pm m\pi\,, \tag{B.1}$$

$$\varphi_m = \vec{k}_m \cdot (f\,\hat{e}_z + x_m \hat{e}_x)\,, \tag{B.2}$$

$$\varphi_0 = k_z(k_x = 0)f\,, \tag{B.3}$$

where the sign in Eq. (B.1) corresponds to the sign of ε_z'. In other words, the sign characterizes refraction of fields inside metamaterials. The next step is to relate x_m to ε_{xy}, ε_z, and f. Using relation of Poynting vectors and wavevectors [Eq. (2.10)], $S_{x,m} = -S(\theta_m)\sin\theta_m$, and $S_{z,m} = S(\theta_m)\cos\theta_m$ where

$$S(\theta_m) = \frac{c^2}{4\pi\omega} K(\alpha_m) \sqrt{\frac{\sin^2\alpha_m}{\varepsilon_z^2} + \frac{\cos^2\alpha_m}{\varepsilon_{xy}^2}}\,, \tag{B.4}$$

$$K(\alpha_m) = \frac{\omega}{c}\left[\frac{\sin^2\alpha_m}{\varepsilon_z} + \frac{\cos^2\alpha_m}{\varepsilon_{xy}}\right]^{-1/2}\,, \tag{B.5}$$

Eq. (B.1) yields

$$K(\alpha_m)\sqrt{\frac{\sin^2\alpha_m}{\varepsilon_z^2} + \frac{\cos^2\alpha_m}{\varepsilon_{xy}^2}}\left[\varepsilon_{xy}\cos\theta_m + \varepsilon_z\frac{\sin^2\theta_m}{\cos\theta_m}\right] - K(0) = \pm\frac{m\pi}{f} \tag{B.6}$$

Note that θ_m and α_m in Eq. (B.6) are connected by the Poynting vector-wavevector relation. Using $x_m = f\tan\theta_m$, we obtain Eq. (3.5). In the case of an isotropic material, Eq. (B.6) is reduced to the conventional Fresnel zone plate [116].

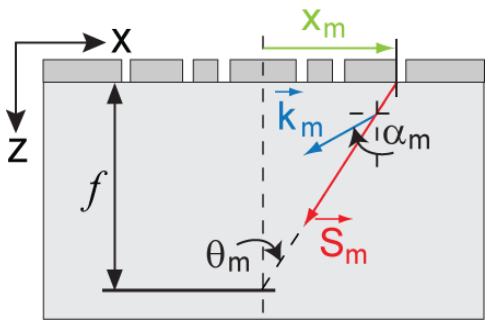

FIGURE B.1: Schematic of Fresnel lens hypergratings; the coordinate of m-th zone is related to Poynting vector ($\vec{S}_m$) and wavevector ($\vec{k}_m$); note that in anisotropic material, $\vec{S}_m$ and $\vec{k}_m$ have different directions, whereas their corresponding angles to optical axis (z-axis) are θ_m and α_m, respectively.

In hyperbolic structures, two significantly different types of refraction might be considered. In the case of $\varepsilon_z' < 0 < \varepsilon_{xy}'$, θ_m is limited by the resonance cone [Eq. (3.4)]. Therefore, a Fresnel lens based on this material will have at most m_{max} zones where $m_{max} = 2f\sqrt{\varepsilon_{xy}'}/\lambda_0$. In contrast, the material with $\varepsilon_{xy}' < 0 < \varepsilon_z'$ yields wave propagation outside the cone. Therefore, this Fresnel lens has infinite number of zones with the initial minimum shift from the focal axis, $x_0 = f\sqrt{-\varepsilon_{xy}'/\varepsilon_z'}$.

Appendix C - Analytical Calculation of Overlap Integrals

In a planar structure, the scalar products yield analytical solutions, substantially speeding up the calculation. This Appendix is devoted to the computation of overlap integrals with all possible integration limits.

Firstly, assuming that each of the modal fields has dependence [Eqs. (5.2)-(5.3)]:

$$\mathbb{E}, \mathbb{H} \propto \Phi^{+} e^{i\, k_x\, x} + \Phi^{-} e^{-i\, k_x\, x}\,, \tag{C.1}$$

where $\Phi^{\pm}$ is the field contribution functions independent on x. The overlapping of the field components can be considered by improper integration of the field components over x covering infinite space [Eqs. (5.9) and (5.18)]. The integration can be chopped into many segments according to discontinuity of layers at a two-stack interface; each segment of the scalar product (ξ) has general form:

$$\xi = w \int_{x_1}^{x_2} \left(\Phi^{+} e^{i\, k_x\, x} + \Phi^{-} e^{-i\, k_x\, x}\right)\left(\widetilde{\Phi}^{+} e^{i\, \tilde{k}_x\, x} + \widetilde{\Phi}^{-} e^{-i\, \tilde{k}_x\, x}\right) dx\,, \tag{C.2}$$

where w represents the weighting factor of the numerical integration over k_x. The limits of integration of the integral, $\{x_1, x_2\}$ are classified into three cases:

- Case 1: x_1 and x_2 finite
- Case 2: x_1 and $x_2 \to \infty$
- Case 3: x_1 finite, $x_2 \to \infty$
- Case 4: $x_1 \to -\infty$, x_2 finite

The solutions of these three cases are given as $\xi = \xi_1 + \xi_2$ where ξ_1 and ξ_2 are following.

Case 1: x_1 and x_2 finite

$$\frac{\xi_1}{w} = \begin{cases} \dfrac{\Phi^+\tilde{\Phi}^+\left[e^{i(k_x+\tilde{k}_x)x_2} - e^{i(k_x+\tilde{k}_x)x_1}\right] - \Phi^-\tilde{\Phi}^-\left[e^{-i(k_x+\tilde{k}_x)x_2} - e^{-i(k_x+\tilde{k}_x)x_1}\right]}{i\left(k_x+\tilde{k}_x\right)} & ;\ k_x \neq -\tilde{k}_x \\ \left(\Phi^+\tilde{\Phi}^+ + \Phi^-\tilde{\Phi}^-\right)(x_2 - x_1) & ;\ k_x = -\tilde{k}_x \end{cases},$$

(C.3)

$$\frac{\xi_2}{w} = \begin{cases} \dfrac{\Phi^+\tilde{\Phi}^-\left[e^{i(k_x-\tilde{k}_x)x_2} - e^{i(k_x-\tilde{k}_x)x_1}\right] - \Phi^-\tilde{\Phi}^+\left[e^{-i(k_x-\tilde{k}_x)x_2} - e^{-i(k_x-\tilde{k}_x)x_1}\right]}{i\left(k_x-\tilde{k}_x\right)} & ;\ k_x \neq \tilde{k}_x \\ \left(\Phi^+\tilde{\Phi}^- + \Phi^-\tilde{\Phi}^+\right)(x_2 - x_1) & ;\ k_x = \tilde{k}_x \end{cases}.$$

(C.4)

Case 2: x_1 and $x_2 \to \infty$

In this case, the stack comprises at most single layer, allowing only propagation of top and bottom modes, which are characterized by real-valued wavevector k_x. Using the integration property [214]

$$\int_{-\infty}^{\infty} dx\, e^{\pm ikx} = 2\pi\delta(k)\,, \tag{C.5}$$

we arrive

$$\frac{\xi}{w} = \left(\Phi^+\tilde{\Phi}^+ + \Phi^-\tilde{\Phi}^-\right)2\pi\delta\left(k_x+\tilde{k}_x\right) + \left(\Phi^+\tilde{\Phi}^- + \Phi^-\tilde{\Phi}^+\right)2\pi\delta\left(k_x-\tilde{k}_x\right). \tag{C.6}$$

Case 3: x_1 finite, $x_2 \to \infty$

This case is different from the previous one, because one of the limits goes finite; that is, the stack contains at least two layers. For the plasmonic planar structure, the guided modes are characterized by the in-plane components of their wavevectors k_z, which allows wavevectors k_x to be complex numbers. However, the electromagnetic fields must not contain exponentially growing components; hence, the condition $k_x'' \geq 0$ must always be enforced. If $k_x'' \neq 0$, then Φ^- must be vanished. With the properties [214]

$$\begin{aligned} \int_{x_1}^{\infty} dx\, e^{\pm ikx} &= \int_{x_1}^{0} dx\, e^{\pm ikx} + \int_{-\infty}^{\infty} dx\, \Theta(x) e^{\pm ikx} \\ &= \int_{x_1}^{0} dx\, e^{\pm ikx} + \left(\pi\delta(k) \pm \frac{i}{k}\right), \end{aligned} \tag{C.7}$$

where $\Theta(x)$ is Heaviside step function, we obtain

$$\frac{\xi_1}{w} = \begin{cases} \dfrac{-\Phi^+\tilde{\Phi}^+ e^{i(k_x+\tilde{k}_x)x_1} + \Phi^-\tilde{\Phi}^- e^{-i(k_x+\tilde{k}_x)x_1}}{i\left(k_x+\tilde{k}_x\right)} & ;\ k_x \neq -\tilde{k}_x \\ \left(\Phi^+\tilde{\Phi}^+ + \Phi^-\tilde{\Phi}^-\right)\left(\dfrac{\pi}{w} - x_1\right) & ;\ k_x = -\tilde{k}_x \end{cases}, \tag{C.8}$$

$$\frac{\xi_2}{w} = \begin{cases} \dfrac{-\Phi^+\tilde{\Phi}^- e^{i(k_x-\tilde{k}_x)x_1} + \Phi^-\tilde{\Phi}^+ e^{-i(k_x-\tilde{k}_x)x_1}}{i\left(k_x-\tilde{k}_x\right)} & ;\ k_x \neq \tilde{k}_x \\ \left(\Phi^+\tilde{\Phi}^- + \Phi^-\tilde{\Phi}^+\right)\left(\dfrac{\pi}{w} - x_1\right) & ;\ k_x = \tilde{k}_x \end{cases}. \tag{C.9}$$

Note that the terms $\left(\frac{\pi}{w} - x_1\right)$ in Eqs. (C.8) and (C.9) are approximated from Eq. (C.5) [see illustration of the improper integration in Fig. (C.1)].

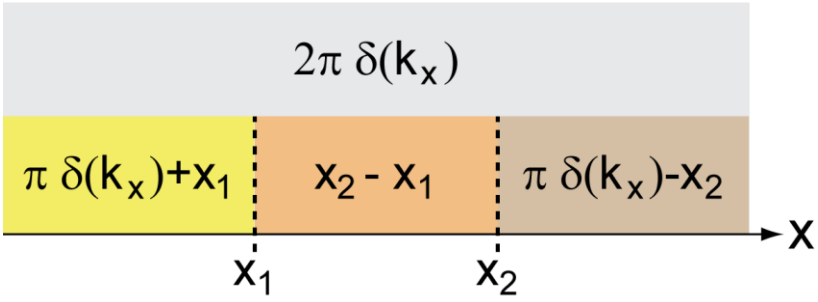

FIGURE C.1: The improper integration of $\exp(\pm ikx)$ over x [Eq. (C.5)] is divided into three regions, indicated by different colors; result of the piecewise integration is given in each region; total summation yields $2\pi\delta(k_x)$.

Case 4: $x_1 \to -\infty$, x_2 finite

This case is similar to Case 3. The analytical calculation yields

$$\frac{\xi_1}{w} = \begin{cases} \dfrac{\Phi^+\tilde{\Phi}^+ e^{i(k_x+\tilde{k}_x)x_2} - \Phi^-\tilde{\Phi}^- e^{-i(k_x+\tilde{k}_x)x_2}}{i\left(k_x+\tilde{k}_x\right)} & ;\ k_x \neq -\tilde{k}_x \\ \left(\Phi^+\tilde{\Phi}^+ + \Phi^-\tilde{\Phi}^-\right)\left(\dfrac{\pi}{w}+x_2\right) & ;\ k_x = -\tilde{k}_x \end{cases}, \tag{C.10}$$

$$\frac{\xi_2}{w} = \begin{cases} \dfrac{\Phi^+\tilde{\Phi}^- e^{i(k_x-\tilde{k}_x)x_2} - \Phi^-\tilde{\Phi}^+ e^{-i(k_x-\tilde{k}_x)x_2}}{i\left(k_x-\tilde{k}_x\right)} & ;\ k_x \neq \tilde{k}_x \\ \left(\Phi^+\tilde{\Phi}^- + \Phi^-\tilde{\Phi}^+\right)\left(\dfrac{\pi}{w}+x_2\right) & ;\ k_x = \tilde{k}_x \end{cases}. \tag{C.11}$$